Theoretical Models for Predicting Catalytic Efficiencies

A Thesis Submitted to
Indian Institute of Technology Guwahati
for the degree of

Doctor of Philosophy

By

Himangshu Pratim Bhattacharyya
Roll No. 176122114

Under Supervision of

Dr. Manabendra Sarma

DEPARTMENT OF CHEMISTRY
INDIAN INSTITUTE OF TECHNOLOGY GUWAHATI
GUWAHATI - 781 039, ASSAM, INDIA

August 2024

Dedicated to My Beloved Parents,

Whose Love and Sacrifices have been My Foundation,

&

To All My Teachers, Whose Wisdom and Guidance have Shaped me into Who I am Today.

Department of Chemistry
Indian Institute of Technology Guwahati
Guwahati - 781 039, India

STATEMENT

The work contained in the thesis entitled "**Theoretical Models for Predicting Catalytic Efficiencies**" has been carried out by me at the Indian Institute of Technology Guwahati, under the supervision of Dr. Manabendra Sarma, Department of Chemistry, Indian Institute of Technology Guwahati. This work has not been submitted elsewhere for the award of any degree.

Himangshu Pratim Bhattacharyya

Roll No. 176122114

Department of Chemistry

Indian Institute of Technology Guwahati

Guwahati - 781 039, Assam, India

Dr. Manabendra Sarma

Associate Professor
Department of Chemistry
Indian Institute of Technology Guwahati
Guwahati - 781 039, India
Phone: +913612582318, Fax: +913612582349
Email: msarma@iitg.ac.in

CERTIFICATE

This is to certify that the work contained in the thesis entitled "**Theoretical Models for Predicting Catalytic Efficiencies**" has been carried out by **Mr. Himangshu Pratim Bhattacharyya** (Roll No. 176122114) at the Indian Institute of Technology Guwahati, under my supervision. This work has not been submitted elsewhere for award of any degree.

Dr. Manabendra Sarma

Thesis Supervisor

Acknowledgements

I would like to express my sincere gratitude to all those who have contributed to the completion of this thesis. First and foremost, I express my sincere appreciation to my advisor, Dr. Manabendra Sarma, for allowing me to carry out the work under him. I am indebted to his mentorship, guidance, constructive feedback, and support throughout the tough times of my PhD journey. Thank you, sir, for all your support.

I extend my appreciation to the chairperson Professor Ashish Kumar Gupta, and members of my doctoral committee Professor Aditya Narayan Panda and Dr. Dipankar Srimani for their constructive and thoughtful suggestions, which significantly enhanced the quality of this work.

I am deeply grateful to the Department of Chemistry at the Indian Institute of Technology Guwahati (IIT Guwahati) and to the faculty members and staff. I appreciate the supercomputing facilities Param-Ishan and Param-Kamrupa at IIT Guwahati for enabling me to carry out my research calculations. A special thanks go to Mr. Jeherul Islam and the other members of the HPC support team for their assistance and cooperation throughout my PhD journey.

I also extend my heartfelt thanks to the Department of Science and Technology (DST), Government of India, for providing me with the *Innovation in Science Pursuit for Inspired Research* (INSPIRE) Fellowship (Fellowship No. DST/INSPIRE Fellowship/2017/IF170899).

I extend my deepest gratitude to my parents, brother, and sister-in-law whose constant encouragement, sacrifices, and unshakable belief in my capabilities have not only been the driving force behind my academic pursuits but also a source of immeasurable emotional support. Throughout the journey, my little niece Jiya has been a painkiller to my sorrows and a booster to my happiness.

I want to express my heartfelt gratitude to my labmates Juhi, Kisan, Bittu, Niharika, Upasana, Monalisha, Biman, Rabu, Shubam, Samsung, Manash, Anand, and Rimi for their support, which was instrumental in completing my work. A special thanks to my juniors Shubam and Manash for the fruitful discussion during my research journey.

I thank my beloved friend Murchana for her unwavering support in the tough times of my life. Your belief in my abilities and constant encouragement have been more than just support; they have been the bedrock of my resilience. I am also thankful to my friends and seniors Parikshit Saikia, Pranab J Sarma, Banuary, Neeldip, Niranjan, Debajit, and Hirak for always being there during my research journey.

Synopsis

The theoretical prediction of catalytic efficiency has become an urgent priority. The advent of density functional theory (DFT) has ushered in an era of precise quantitative computations in this field. Augmenting this sophisticated approach with tools that can accurately assess catalyst efficiency would be exceptionally advantageous. The thesis covers the methodological development to predict catalysts' turnover frequency (TOF) in connection to efficiency. To represent the efficiency of catalysts, the TOF is considered because the term is more acceptable and facile to the scientific community rather than the turnover number (TON). In this context, we developed our first strategy, the Efficiency Conceptualization Model (ECM), which leverages quantum mechanical techniques to optimize efficiency as measured by turnover frequency (TOF). The ECM strategy relies on the kinetics and thermodynamics of the rate-determining step (RDS). In addition, we developed the second method to delineate the maximum kinetic efficiency of catalysts, named the *MaxKinEff* model, which also describes the TOF of catalysts in the light of collision theory. The *MaxKinEff* model assumes the possible collisions within a cubical system of unit dimensions to

take into account the collisions at a more considerable distance. Both strategies were further extrapolated to convert turnover frequency (TOF) to turnover number (TON). All calculations and relationships were conducted under standard conditions of temperature, 1 atm pressure, and neutral pH for ease of comparison. To validate both strategies, we carried out the water-oxidation reaction using twenty-six experimentally synthesized transition metal catalysts that exclusively follow the water-nucleophilic attack (WNA) pathway.

Chapter-1: Introduction to Catalysis

Chapter 1 briefly overviews the evolution and history of catalysis. The chapter discusses the classification of catalysis and its significance in context to the turnover number (TON) and turnover frequency (TOF). In addition, a broad summary of the established models- (a) Energetic Span Model, (b) Degree of Rate Control, (c) Microkinetic Modelling, and (d) Molecular Volcano Plot were also presented. The chapter concludes by covering the goals and future possibilities of developed methods.

Chapter-2: Efficiency Conceptualization Model: A Novel Method for Computing the Turnover of Catalysts

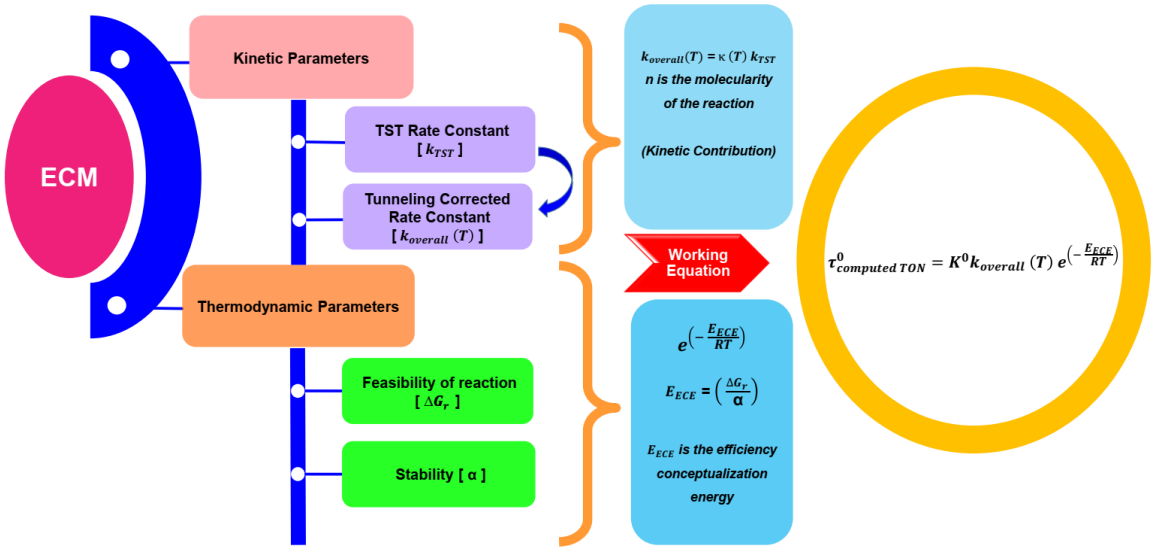

The quantum mechanical studies allow us to compute the detailed energy landscape of a catalytic cycle. The efficiency of catalysts can be inferred using turnover numbers (TONs) and turnover frequencies (TOFs). However, the computational prediction of turnover frequency (TOF) is challenging. In this work, we developed a novel strategy, the Efficiency Conceptualization Model (ECM), to predict the efficiency of catalysts as a function of turnover frequency (TOF). The ECM method relies on the kinetics and thermodynamics of the rate-determining step (RDS) and provides Eq. (1) to

calculate the TOF.

$$\Gamma^{0}_{computed\ TOF} = K^{0} k_{overall}(T) \times exp\left(- \frac{E_{ECE}}{RT} \right) \tag{1}$$

The developed method further correlated the computed TOF to the half-life of the catalysts and extended to define the catalyst's turnover number (TON).

Chapter-3: Implementation of ECM: An Application to the Transition Metal-Catalyzed Water-Oxidation Reaction

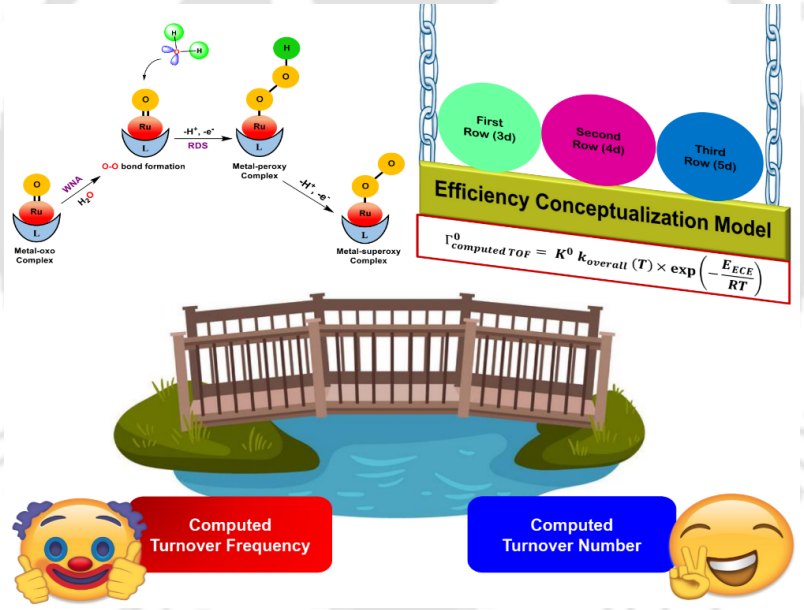

To verify the ECM approach, we first examined the water oxidation reaction. Ruthenium (Ru)-complexes, known for their clear structure and diagonal relationship with the manganese (Mn) centre, are frequently studied among the second-

row (4d) transition metal catalysts. First-row (3d) and third-row (5d) transition metals (TMs) have garnered significant research interest in the development of efficient bio-inspired water-oxidation catalysts (WOCs) due to their abundance and cost-effectiveness. However, because of the substitutional labile nature, the evolution of the first-row TMs is limited. In the current Chapter, we validated the ECM strategy to the first (3d) and third (5d) row transition metal elements along with the different Ru-catalyzed water oxidation catalysts (Ru-WOCs) that were morphologically different in terms of their rigidity, substitution, and chelation. From the series of transition metals, we have considered twenty-six (26) catalysts from Manganese (Mn) to Copper (Cu) from the first row, Ruthenium (Ru) from the second row, and Iridium (Ir) from the third row as the active catalytic centres for water oxidation. With the kinetics and thermodynamics of the reaction, the model's validity was assessed by computing the turnover frequency, $\Gamma^{0}_{computed\ TOF}$ and turnover number (TON), $\tau^{0}_{computed\ TON}$ of catalysts.

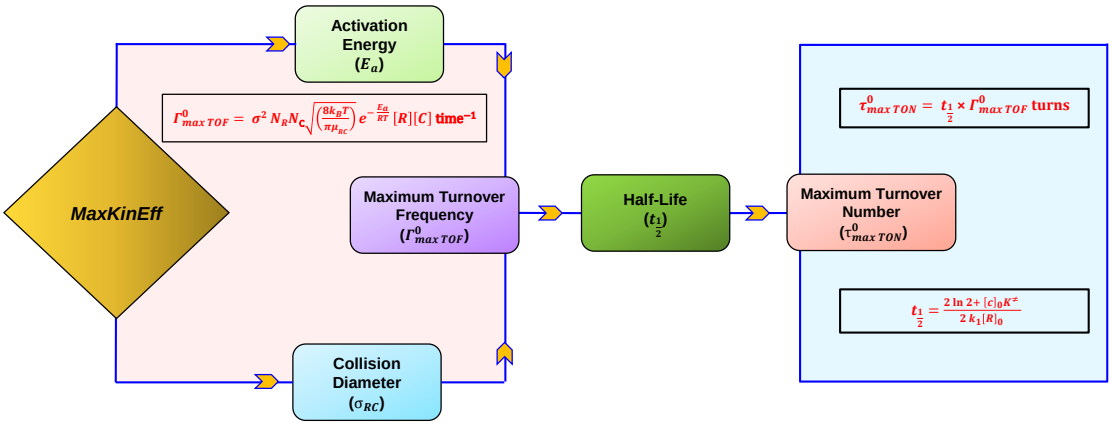

A catalytic cycle is a recurring process that involves many catalytic reaction steps. The chemical species are generated newly at a particular "rate" during each reaction step. In particular, when the reaction rate is the first order to the catalysts, the "rate" is coined as the turnover frequency (TOF) under the steady-state regime. In this Chapter, we developed a second model that provides a new perspective to compute the maximum kinetic efficiency of a catalyst, which we named the *MaxKinEff* Model. The *MaxKinEff* is the bedrock of the collision theory, where the catalyst and the substrate are assumed to be hard spheres. The simple and straightforward model predicts the maximum turnover frequency, $\Gamma^0_{max\ TOF}$ and is represented by Eq. (2)

$$\Gamma^0_{max\ TOF} = \sigma^2_{RC}\sqrt{\left(\frac{8k_BT}{\pi\mu_{RC}}\right)}\, e^{-\frac{E_a}{RT}} \quad time^{-1} \tag{2}$$

$$\tau^0_{max\ TON} = \Gamma^0_{max\ TOF} \times \mathbf{t}_{\frac{1}{2}} \quad turns \tag{3}$$

In addition, we have calculated the half-life of the catalyst and correspondingly estimated the maximum turnover number of the catalyst $\tau^0_{max\ TON}$. Further, the standard conditions of temperature, pressure, and concentration were theoretically considered to evaluate their effect on the turnover frequency of the catalyst. Thus, the model provides a way to comprehend the activity of the catalyst.

Chapter-5: Application of the *MaxKinEff* Model to Water-Oxidation Catalysts: A Newer Perspective to Efficiency

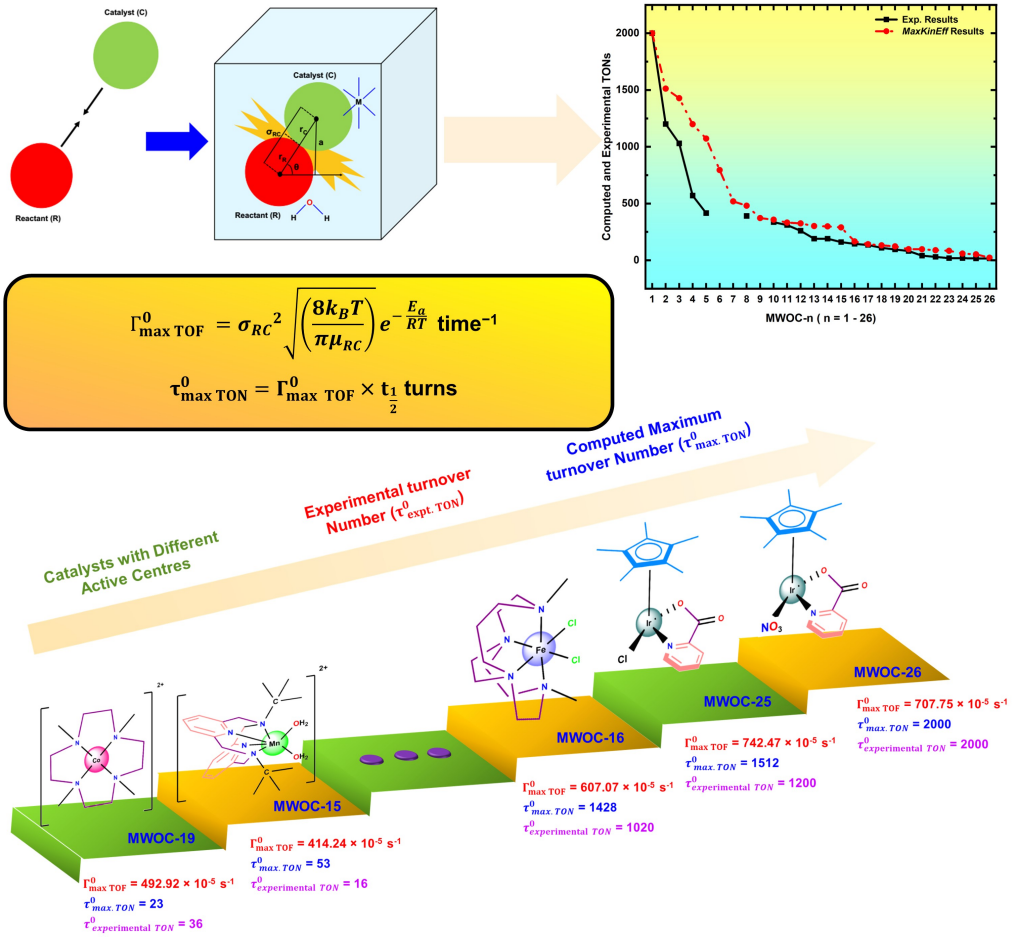

The water oxidation reaction in Photosystem II (PSII) has captivated researchers, offering a blueprint for creating active and durable synthetic water oxidation catalysts that emulate the oxygen-evolving complex (OEC) of PSII. In Chapter 5, we apply the *MaxKinEff* to the water oxidation catalysts with 3d (from Mn to Cu), ruthenium (Ru) from 4d, and iridium (Ir) from 5d transition metals as active metal centres to calculate the maximum turning over of catalysts. Since for water oxidation reaction, the mass of the catalyst (m_R) >> the mass of the catalyst (m_C), therefore, Eq. (2) converts to

$$\Gamma^0_{max\ TOF} = \sigma^2_{RC}\sqrt{\left(\frac{8k_BT}{\pi m_R}\right)}\, e^{-\frac{E_a}{RT}} \quad time^{-1} \tag{4}$$

The result from our computations suggests that among the ruthenium catalysts, MWOC-3 has the highest turnover frequency, with a $\Gamma^0_{max\ TOF}$ of 1176.87 $\times$ 10^{-5} s^{-1} in the M06-L level of theory, whereas MWOC-10 shows a $\Gamma^0_{max\ TOF}$ of 603.16 $\times$ 10^{-5} s^{-1}. Extending the theory, the calculated shows $\tau^0_{max\ TON}$ of 1199 for MWOC-8, which has the highest computed and experimental turnover number among the chosen ruthenium catalysts. Further, our studies delineate that the Ir catalysts, MWOC-25 and MWOC-26, have the maximum computed TON, $\tau^0_{max\ TON}$ of 2000 and 1512, mimicking the experimental TON, $\tau^0_{experimental\ TON}$ of 2000 and 1200, respectively.

Chapter-6: A Comparative Analysis of Developed Models: Efficiency Conceptualization Model *vs.* *MaxKinEff* Model

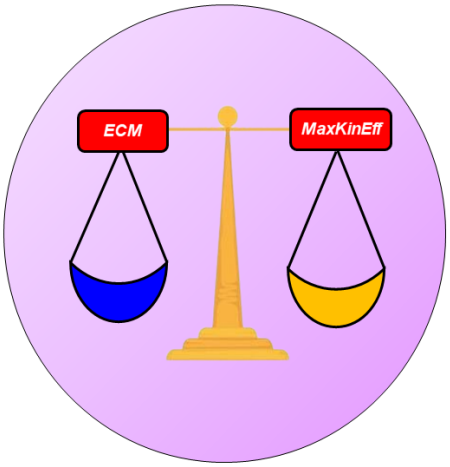

The Chapter presents a comparative analysis of two developed models: the Efficiency Conceptualization Model (ECM) and the Maximum Kinetic Efficiency (*MaxKinEff*) Model. The methodological differences between the ECM and *MaxKinEff* models significantly influence their respective predictions, offering unique insights into catalyst performance. The ECM primarily focuses on the rate-determining step (RDS) of the reaction mechanism, providing a detailed understanding of the critical kinetic step. In contrast, the *MaxKinEff* model evaluates the overall reaction rate, offering a broader perspective. Additionally, the ECM takes a comprehensive approach by considering kinetic and thermodynamic factors associated with the RDS, whereas the *MaxKinEff* operates solely as a kinetic model. Despite their differences, both models

are unique, each with its specific assumptions, and predict efficiencies in terms of turnover number and turnover frequencies.

Chapter-7: Summary and Conclusions

The final Chapter of the thesis summarizes the work done and sketches potential future research areas. This Chapter covers the salient insights and impacts of the recent research and proposes prospective future research directions. It highlights the results accomplished and provides probable amendments to the developed methods and their applications. In Chapter 2, we developed a novel model, namely the efficiency conceptualization model (ECM). The Chapter focuses on the mathematical formulation of the ECM strategy and its basis for constructing equations to compute the TOFs. The method has been extended further to calculate the TONs of catalysts. Chapter 3 comprises the application of the ECM strategy to water oxidation reaction with a special reference to transition metals (TMs) catalysts. To validate the applicability of the method, twenty-six transition metals (TMs) have been considered, with thirteen being ruthenium catalysts (4d), while the other thirteen belong to the 3d and 5d transition metals. The results obtained from the ECM conclude that the theoretical TONs corroborate with experimental TONs. Chapter 4 discusses the *MaxKinEff* model, which is purely a kinetic model built on the collision theory. The method provides a lucid perspective of TOF to determine the activity of the catalysts.

With the same set of twenty-six water oxidation catalysts, Chapter 5 evaluated the TOFs and TONs of catalysts in the light of the *MaxKinEff* model. In Chapter 6, a comparison of the developed methods, i.e., the ECM strategy and *MaxKinEff* model, was made to unveil the accuracy of the methods.

List of Publications

From Thesis

1. **H. P. Bhattacharyya**, and M. Sarma, "*MaxKinEff*: A Collision Theory-Based Approach for Analyzing Turnover Frequency and Turnover Number in Catalytic Processes" *Chem. Asian J.* **2024**, *19*, e202400674.

2. **H. P. Bhattacharyya**, and M. Sarma, "Efficiency Conceptualization Model: A Theoretical Method for Predicting the Turnover of Catalysts" *ChemPhysChem* **2024**, *25*, e202400004.

Outside of Thesis

1. **H. P. Bhattacharyya**, and M. Sarma, "Role of Active Centers in Predicting the Catalyst Turnover: A Theoretical Study" *Chem. Eur. J.* **2024**, *30*, 202403631.

2. D. Bora, **H. P. Bhattacharyya**, F. R. Gayen, S. Baguli, P. Patel, M. Sarma, and B. Saha, "Bimetallic Cooperativity of a Ferrocene-Based Iridium NHC

Complex in Water Oxidation Catalysis: A New Frontier for Efficient Oxygen Evolution" *Chem. Asian J.* **2024**, e202401357.

3. B. K. Rajbongshi, S. Abdullah, B. Lama, **H. P. Bhattacharyya**, and M. Sarma, "Regioselective and Solvent-dependent Photoisomerization Induced Internal Conversion in Red Fluorescent Protein Chromophore Analogues" *RSC Advances* **2024**, *14*, 18373.

4. N. Keot, B. Lama, H. K. Singh, **H. P. Bhattacharyya**, and M. Sarma, "Unveiling the Noncovalent Interaction of Thiazol-2-ylidene and Its Derivatives as N-heterocyclic Carbene with Different Proton Donor Molecules" *ChemPhysChem* **2023**, *24*, e202300413.

5. T. L. Fischer, M. Bödecker, S. M. Schweer, J. Dupont, V. Lepère, A. Zehnacker-Rentien, M. A. Suhm, B. Schröder, T. Henkes, D. M. Andrada, R. M. Balabin, H. K. Singh, **H. P. Bhattacharyya**, M. Sarma, S. Käser, K. Töpfer, L. I. Vazquez-Salazar, E. D. Boittier, M. Meuwly, G. Mandelli, C. Lanzi, R. Conte, M. Ceotto, F. Dietrich, V. Cisternas, R. Gnanasekaran, M. Hippler, M. Jarraya, M. Hochlaf, N. Viswanathan, T. Nevolianis, G. Rath, W. A. Kopp, K. Leonhard, and R. A. Mata, "The First HyDRA Challenge for Computational Vibrational Spectroscopy" *Phys. Chem. Chem. Phys.* **2023**, *25*, 22089.

6. S. Kumar, H. K. Singh, **H. P. Bhattacharyya** and M. Sarma, "Low Energy

Electron Interaction with Citric Acid: A Local Complex Potential based Time-Dependent Wavepacket Study" *J. Chem. Sci.* **2023**, *135*, 88.

7. H. K. Singh, R. R. Changmai, N. Keot, **H. P. Bhattacharyya**, and M. Sarma, "A Computational Insight on the Noncovalent Interactions of Aminothiazole-based Palladium (II) Complexes with DNA as a Potent Anticancer Agent" *Polyhedron* **2023**, *239*, 116448.

8. P. Kalita, B. Medhi, H. K. Singh, **H. P. Bhattacharyya**, N. Gupt, and M. Sarma, "Perturbing π-clouds with Substituents to Study the Effects on Reaction Dynamics of gauche-1, 3-Butadiene to Bicyclobutane Electrocyclization" *ChemPhysChem* **2023**, *24*, e202200727.

9. B. K. Rajbongshi, H. P. Bhattacharyya, C.D. Pegu, S. Sharma, P.K. Baruah and M. Sarma, "Ultra-High Stokes Shift in Polycyclic Chromeno [2, 3-b] Indoles" *Polycyl. Aromat. Comp.* **2022**, *42*, 1710.

List of Conference Proceedings

1. **H. P. Bhattacharyya** and M. Sarma, "Efficiency Conceptualization Model in the light of Bio-Inspired Molecular Water Oxidation Catalysts", 6th Symposium on Advanced Biological Inorganic Chemistry (SABIC) 2024, *January 07 – 11, 2024*, Altair Boutique Hotel, Salt Lake, Kolkata (Poster).

2. **H. P. Bhattacharyya** and M. Sarma, "Developing A Model to Theoretically Assess the Turnover Frequency in The Light of Collision Theory", 6th International Conference on Molecular Simulations (ICMS), *October 06 – 09, 2023*, National Taiwan University, Taiwan (Oral Talk).

3. **H. P. Bhattacharyya** and M. Sarma," Assessing the Efficiency for Water Splitting Reaction: A Step Towards Sustainable Development", North-Eastern Research Conclave (NERC), *May 20 – 22, 2022*, Indian Institute of Technology Guwahati, Assam, India (Oral Talk).

4. **H. P. Bhattacharyya** and M. Sarma, "Computational Strategy to Determine the Efficacy of the Catalyst(s): Efficiency Conceptualization Model (ECM)",

Theoretical Chemistry Symposium (TCS), *December 11 – 14, 2021*, Online, Indian Institute of Science Education and Research (IISER) Kolkata, Mohanpur, India (Poster).

5. **H. P. Bhattacharyya** and M. Sarma, "Roadmap for Designing the Strategy to Mimic the Experimental Turnover Numbers: A Case Study to Artificial Water Splitting Reaction", 57th Symposium on Theoretical Chemistry (STC), *September 20 – 24, 2021*, Online, University of Würzburg, Germany (Poster).

6. **H. P. Bhattacharyya** and M. Sarma, "Molecular Water Oxidation Catalyst(s): An Approach for Predicting the Efficiency", Recent Trends in Chemical Sciences (RTCS-2020), *December 26 – 29, 2020*, Kolkata, West Bengal, India (Oral Talk).

7. **H. P. Bhattacharyya** and M. Sarma, "Prediction of Efficiency of Photocatalyst(s) in Water Splitting: A Computational Study", Spectroscopy and Dynamics of Molecules and Clusters (SDMC) 2020, *February 20 – 23, 2020*, Kumbhalgarh, Rajasthan, India (Poster).

8. **H. P. Bhattacharyya** and M. Sarma, "Efficiency of a Photocatalyst: A Computational Investigation", Recent Advances in Chemistry (RAC) 2019, *October 14 – 15, 2019*, National Institute of Technology Meghalaya, Shillong, India (Poster).

List of Abbreviations

Abbreviations	Description
DFT	Density Functional Theory
IUPAC	International Union of Pure and Applied Chemistry
TOF	Turnover Frequency
TON	Turnover Number
ECM	Efficiency Conceptualization Model
ECE	Efficiency Conceptualization Energy
RDS	Rate Determining Step
HOMO	Highest Occupied Molecular Orbital
LUMO	Lowest Unoccupied Molecular Orbital
EA	Electron Affinity
TS	Transition State
TST	Transition State Theory
PCET	Proton-Coupled Electron Transfer
MaxKinEff	Maximum Kinetic Efficiency

TM	Transition Metal
MWOC	Molecular Water-Oxidation Catalyst
NHE	Normal Hydrogen Electrode
I2M	Interaction of Two Metal-oxo Units
AIMD	Ab Initio Molecular Dynamics
PSII	Photosystem II
CAN	Ceric Ammonium Nitrate
OEC	Oxygen-Evolving Complex
TDTS	TOF-Determining Transition State
TDI	TOF-Determining Intermediate
DRC	Degree of Rate Control
LFSR	Linear Free Energy Scaling Relationship
e.e.	Enantiomeric Excess
ECP	Effective Core Potential
BS	Broken Spin-Symmetry
SMD	Solvation Model Density
ZPE	Zero-point Energy
pda	1,10-phenanthroline-2,9-dicarboxylate
bda	2,2′-bipyridine-6,6′ -dicarboxylate

pic	4-picoline
py	pyridine
Br-py	4-Bromopyridine
bpy	2,2′-bipyridine
tpy	2,2′;6,2″-terpyridine
dpp	2,9-dipyrid-2′-yl-1,10-phenanthroline
Py	pyridinophane
cbc	4,11-dimethyl-1,4,8,11-tetraazabicyclo[6.6.2]hexadecane
OTf	Trifluoromethanesulfonate ($CF_3SO_3^-$)
Me_2Pytacn	1-(2′-pyridylmethyl)-4,7-dimethyl-1,4,7-triazacyclononane
mep	N,N′-dimethyl- N,N′-bis-(2-pyridylmethyl)-ethane-1,2-diamine
12-TMC	1,4,7,10-tetramethyl-1,4,7,10-tetraazacyclododecane
qpy	2,2′:6′,2″:6″,2‴-quaterpyridine
PY5	2,6-bis(1,1-bis(2-pyridyl)ethyl)pyridine
pyalk	2-pyridyl-2-propanoate
κ^2-N,O	2-pyridinecarboxylate
13-TMC	1,4,7,10-tetramethyl-1,4,7,10-tetraazacyclotridecane
Py_3P	N,N -bis(2-(2-pyridyl)ethyl)pyridine-2,6-dicarboxamidate
Hbpp	2,6-bis(pyridyl)pyrazole

List of Symbols

Symbols	Description
$\boldsymbol{c}^0$	Standard concentration
ΔG_a	Standard Gibbs energy of activation
$\boldsymbol{k}_B$	Boltzmann's constant
$\boldsymbol{R}$	Universal gas constant
$\boldsymbol{T}$	Temperature
$\mathbf{k}_{overall}(T)$	Overall reaction rate constant
$\kappa(T)$	Transmission coefficient
ω^*	Imaginary frequency
$\mathbf{E}_0$	Ground vibrational state energy of the stationary points
$\mathbf{E}$	Total energy of system
$P^C(\mathbf{E})$	Probability obtained from the transition state theory
$P^T(\mathbf{E})$	Quantum tunnelling probability
$\mathbf{V}_f$	Energy of the forward barrier
$\mathbf{V}_r$	Energy of the reverse barrier

ΔE_f	Zero-point corrected forward energy barrier
$\Gamma^0_{computed\ TOF}$	Computed turnover frequency
$\tau^0_{computed\ TON}$	Computed turnover number
$\Gamma^0_{experimental\ TOF}$	Experimental turnover frequency
$\tau^0_{experimental\ TON}$	Experimental turnover number
ΔG_r	Feasibility of the reaction
E_f	Formation energy
α	Stability of associated adduct
$\mathbf{G}_R$	Free energies of the reactant in RDS
$\mathbf{G}_{[C]}$	Free energies of the catalyst complex in RDS
$\mathbf{G}_{[R-C]}$	Free energies of the product in RDS
$\mathbf{E}_R$	Energy of the reactant in RDS
$\mathbf{E}_{[C]}$	Energy of the catalyst complex in RDS
$\mathbf{E}_{[R-C]}$	Energy of the product in RDS
$\mathbf{E}_{ECE}$	Efficiency conceptualization energy
$\boldsymbol{N}$	Amount of product formed per unit time
$\boldsymbol{N}_0$	Amount of catalyst used
$\left(\frac{N}{N_0}\right)$	Fraction of molecules with energy E_{ECE} (equal to the TOF of the catalyst)

$\mathbf{t}_{\frac{1}{2}}$	Half-life of catalysts
$\mathbf{K}^{\neq}$	Equilibrium constant
σ_{RC}	Collision diameter between $\boldsymbol{R}$ and $\boldsymbol{C}$
$\boldsymbol{N}_R$	Number of reactant molecules per unit volume
$\boldsymbol{N}_C$	Number of catalysts molecules per unit volume
$\mathbf{P}$	Orientation factor
$\mathbf{E}_a$	Activation barrier
$\boldsymbol{r}$	Pearson's correlation coefficient

List of Figures

List of Tables

Contents

1

Introduction to Catalysis

1.1 History of Catalysis

In 1835, the term "catalysis" was coined by Jons Jakob Berzelius.[1] According to Berzelius, during catalysis, instead of the affinity among the molecules, a new operative "catalytic force" exists.[1] The chemical driving force, termed affinity, is recognized without comprehension at the molecular level of reaction rates. Nevertheless, catalysis has served as a fundamental tool for conducting chemical reactions. The application of catalysis was established thousands of years back in the fermentation process. In the Middle Ages, sulphuric acid was produced in the catalytic reactions by burning sulphur with humid air.F[2] Towards the beginning of the nineteenth century, it was further demonstrated that catalysis is a selective process. The decomposition

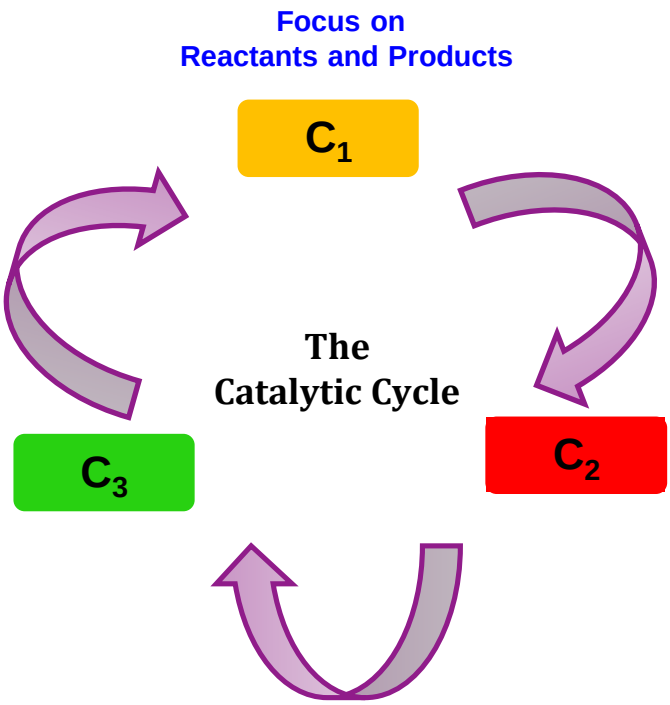

Figure 1.1: The changes in the catalytic forms in a catalytic cycle.

of alcohol is a well-accepted example of selectivity. In the presence of copper (Cu) or iron (Fe), it produces carbon and inflammable gas, whereas in the presence of pumice stone, ethane and water are observed as products.[3] Later on, Ostwald defined that during catalysis, the thermodynamic equilibrium of the reactants and products does not shift; rather, it affects the rate of a chemical reaction.[4]

In modern chemistry, a catalyst is defined as a substance that accelerates the rate of a reaction by choosing an alternate path of lower free energy of activation. A catalyst forms a bond with the reactant to form the product. After forming the product, it gets detached from the catalyst, leaving it unaltered and, therefore, becomes avail-

able for the next catalytic cycle. Therefore, catalysis can be termed as a cyclic event in which the catalyst takes part in the reaction and recovers in its original form at the end of the cycle, as illustrated in Figure 1.1. For example, in the catalytic reaction of the conversion of CO and O_2 into CO_2, both reactants first diffuse to the reactant surface and get adsorbed onto the surface of the catalyst.[5] Energy is released during adsorption, after which the reactants undergo a chemical reaction via the formation of a transition state (TS) to form the product, CO_2.

The free energy of activation for the catalyzed reaction ($\Delta G^{\ddagger}_{cat}$) is defined as the free energy difference between the transition state involved in the catalyzed reaction ($G_{TS,cat}$) and reactant (G_{react}) [Figure 1.2 (a)]. Therefore,

$$\Delta G^{\ddagger}_{cat} = G_{TS,cat} - G_{react} \tag{1.1}$$

Similarly, the free energy of activation for the uncatalyzed reaction, $\Delta G^{\ddagger}_{uncat}$ is defined as

$$\Delta G^{\ddagger}_{uncat} = G_{TS,uncat} - G_{react} \tag{1.2}$$

where $G_{TS,uncat}$ is the free energy of the transition state involved in the uncatalyzed reaction.

The free energy of activation for an uncatalyzed reaction, $\Delta G^{\ddagger}_{uncat}$ is higher than that of the catalyzed ($\Delta G^{\ddagger}_{cat}$) reaction. This is because the catalyst provides an

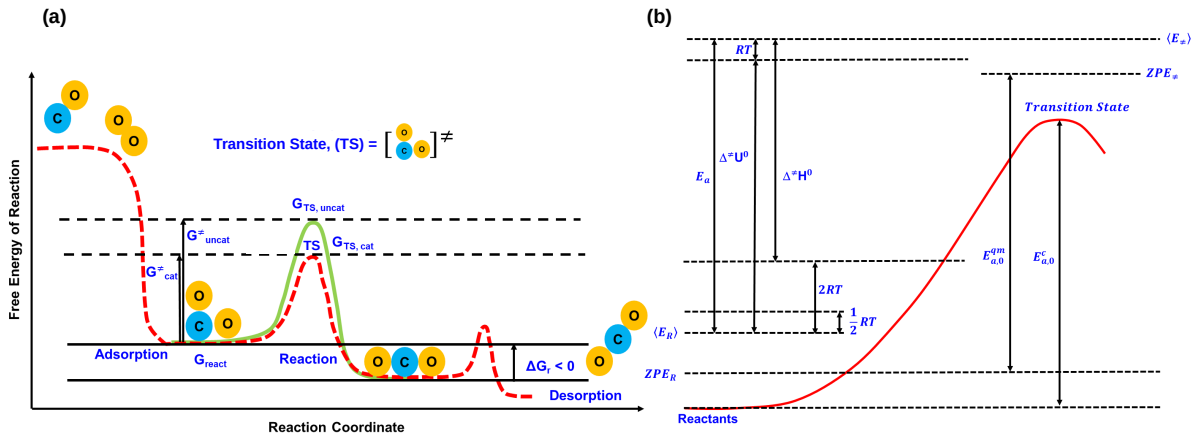

Figure 1.2: (a) The free energy profiles for catalyzed and uncatalyzed reactions; (b) energy diagram showing the energy changes and thermodynamic parameters relationship. In (b), the classical energy barrier, $E^{c}_{a,0}$, quantum energy barrier, $E^{qm}_{a,0}$, ZPE_R, $ZPE_{\neq}$ are the zero-point energies (ZPE) of the reactant and the activated complex, respectively; $<E>_R$, $<E>_{\neq}$ are the average electronic energies of reactant and activated complexes, respectively, $\Delta^{\ddagger}H^0$ is the standard enthalpy of activation, and $\Delta^{\ddagger}U^0$ is the standard change in internal energy. The $\frac{1}{2}$RT refers to the average energy of the colliding molecules.

alternate pathway with lower activation energy for the reaction, which makes the catalyzed reaction faster than the uncatalyzed reaction. For both catalyzed and uncatalyzed forward reactions, the reactants (CO + O) have higher energy than that of the product (CO_2), and therefore, both reactions are exothermic (Gibbs free energy of the reaction, $\Delta G_r < 0$).

Figure 1.2(b) shows the relation between the energy changes in a reaction and the thermodynamic parameters. The kinetic energy of an ensemble at a finite temperature is equal to the average kinetic energy. At absolute zero temperature, the energy difference between the minimum energies of the reactant and the activated complex

is the classical energy barrier, $E^{c}_{a,0}$ of the reaction. On the other hand, the difference between the zero-point corrected energies (ZPE) of the reactants and the activated complex is the quantum energy barrier, $E^{qm}_{a,0}$ of the reaction.[6] When the degrees of freedom of the activated complex and reactant become the same, both species show similar thermal behaviour. Under that condition, the activation energy of the system will not depend upon the temperature of the reaction. For the bimolecular catalyzed reaction [Figure 1.2(a)],

$$\mathbf{CO} + \mathbf{O} \rightleftharpoons [\mathbf{CO\text{-}O}]^{\ddagger} \longrightarrow \mathbf{CO_2},$$

the rate constant, k, is given by

$$k = \frac{k_B T}{h} K_C^{\ddagger}. \tag{1.3}$$

In the above expression, k_B and h are the Boltzmann constant and Planck constant, respectively, and T is the reaction temperature. $K_C^{\ddagger}$ is the equilibrium constant for the reaction given by

$$K_C^{\ddagger} = \frac{[CO-O]^{\ddagger}}{[CO][O]} = \frac{q^{\ddagger}}{[q_{CO}][q_O]} e^{-\frac{E^{qm}_{a,0}}{RT}} \tag{1.4}$$

In Eq. (1.4), q_{CO}, q_O and $q^{\ddagger}$ are the partition functions of the carbon monoxide (CO), oxygen (O), and the activated complex, [CO-O]‡, respectively. Taking the logarithm

and differentiating with respect to T on both sides of Eq. (1.3) results,

$$\frac{d\ ln\ k}{dT} = \frac{d}{dT}[ln\ T + ln\ K_C^{\ddagger}] \tag{1.5}$$

$$\frac{d\ ln\ k}{dT} = \frac{1}{T} + \frac{d(ln\ K_C^{\ddagger})}{dT} \tag{1.6}$$

The variation of the $K_C^{\ddagger}$ with temperature, T, is represented as[6]

$$\frac{d\ ln\ K_C^{\ddagger}}{dT} = \frac{\Delta^{\ddagger}U^0}{RT^2} \tag{1.7}$$

In Eq. (1.7), $\Delta^{\ddagger}U^0$ is the standard change in internal energy and R is the universal gas constant. Using Eq. (1.7) in Eq. (1.6), the equation modifies to

$$\frac{d\ ln\ k}{dT} = \frac{1}{T} + \frac{\Delta^{\ddagger}U^0}{RT^2} \tag{1.8}$$

The rate constant, k is related to the experimental activation energy, E_a, by the relation[6]

$$\frac{d\ ln\ k}{dT} = \frac{E_a}{RT^2} \tag{1.9}$$

The experimental activation energy, E_a, is related to the quantum barrier, $E_{a,0}^{qm}$, by the relation[6]

$$E_a = E_{a,0}^{qm} + mRT \tag{1.10}$$

where m is a temperature-dependent empirical parameter. On comparing Eq. (1.8) and Eq. (1.9),

$$\Delta^{\ddagger}U^0 = E_a - RT \tag{1.11}$$

Further,

$$\Delta^{\ddagger}U^0 = \Delta^{\ddagger}H^0 - P\Delta^{\ddagger}V^0 = \Delta^{\ddagger}H^0 - \Delta^{\ddagger}nRT \tag{1.12}$$

$\Delta^{\ddagger}n$ is the difference in the number of moles between the products ($n_{product}$) and reactants ($n_{reactant}$) when the reaction proceeds via an activated complex. For the considered catalyzed reaction,

$$\Delta^{\ddagger}n = n_{product} - n_{reactant} = 1 - 2 = -1 \tag{1.13}$$

Using the value of $\Delta^{\ddagger}n$ [Eq. (1.13)], Eq. (1.12) modifies to

$$\Delta^{\ddagger}U^0 = \Delta^{\ddagger}H^0 + RT \tag{1.14}$$

$$\Delta^{\ddagger}H^0 = \Delta^{\ddagger}U^0 - RT \tag{1.15}$$

Using Eq. (1.11) in Eq. (1.15),

$$\Delta^{\ddagger}H^0 = E_a - 2RT \tag{1.16}$$

The observed magnitudes of the standard change in internal energy, $\Delta^{\ddagger}U^0$ [Eq. (1.11)] and the standard enthalpy of activation, $\Delta^{\ddagger}H^0$ [Eq. (1.16)], for a bimolecular reaction is schematically represented in Figure 1.2(b).

1.2 Types of Catalysis

A catalyst can exist from the atomic scale to large molecules such as zeolites. Depending on the phases it exists, catalysis may be of various kinds. Understanding different types of catalysis is important for the design and optimization of catalytic processes. A few of them are discussed below.

1.2.1 Homogeneous Catalysis

In homogeneous catalysis, the catalyst and the reactant are in the same phase. For example, in the ruthenium (Ru) catalyzed molecular water-oxidation [Figure 1.3],[7] the water molecule is first attached to the active centre of the metal complex, forming catalyst-water complex, $[Ru^{II} - OH_2]^0$. After that, it undergoes a proton-coupled electron transfer (PCET) process to form the metal-oxo complex, $[Ru^{V} = O]^+$. At this stage, a second water molecule reacts with it to form the metal-hydroperoxo complex, $[Ru^{III} - OOH]^0$. This step requires high activation energy and is, therefore, considered as the rate-determining step (RDS) of the reaction. The metal-hydroperoxo complex further undergoes the PCET process to generate metal-peroxo complex, $[Ru^{IV} - OO]^0$, which subsequently eliminates oxygen and regenerates the catalyst.

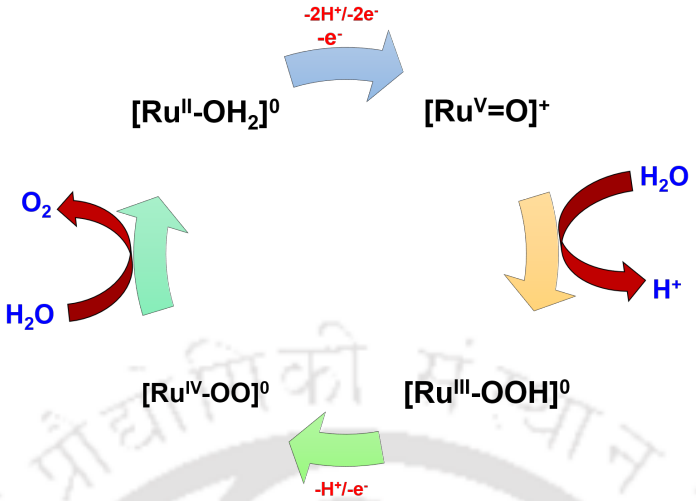

Figure 1.3: Catalytic cycle for ruthenium-catalyzed molecular water-oxidation. This figure is adapted from ref. 7 with permission © 2011 John Wiley & Sons Inc.

1.2.2 Heterogeneous Catalysis

In heterogeneous catalysis, the catalyst and the reactant are in different phases. The catalytic hydrogenation of ethylene (CH_2=CH_2) on the Pt (111) surface is one of the prominent examples of heterogeneous catalysis [Figure 1.4]. The ethylene molecule first undergoes physisorption on the Pt (111) surface via van der Waals forces.[8] After physisorption, the ethylene molecule undergoes chemisorption and forms a chemical bond with the surface of Pt (111). In this step, an equilibrium is maintained between the di-σ-bonded ethylene and π-bonded ethylene. The chemisorption proceeds via a catalytic path followed by the reversible formation of the ethyl intermediate. The intermediate then forms the second C-H bond in the reaction and finally undergoes desorption from the Pt (111) surface to form ethane.[8]

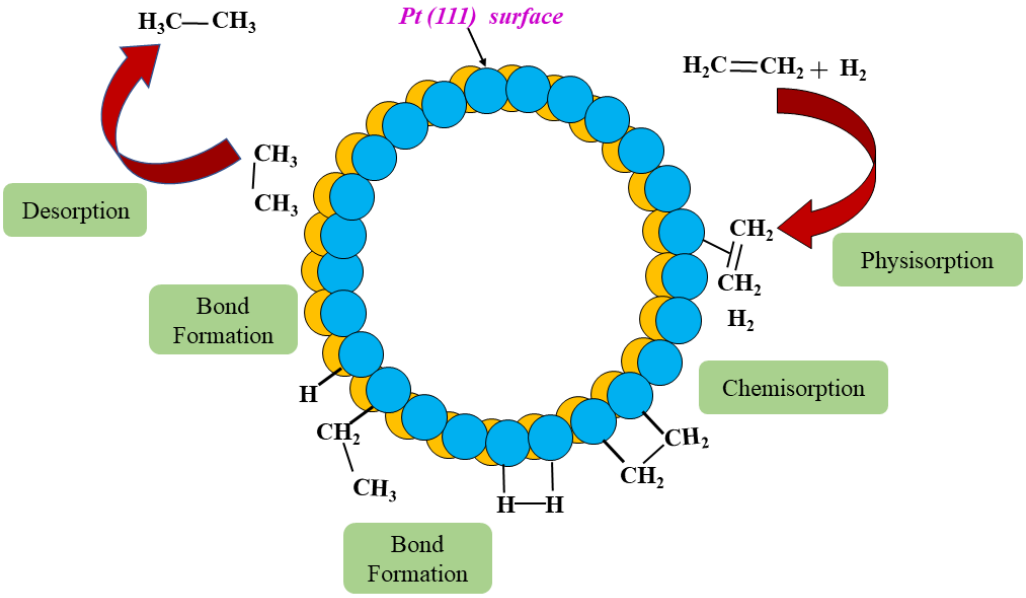

Figure 1.4: Catalytic hydrogenation of ethylene to ethane over Pt (111) surface. This figure is adapted from ref. 8 with permission © 2012 American Chemical Society.

1.2.3 Bio-catalysis

Bio-catalysis is the process in which natural catalysts like enzymes help to accelerate the biological reactions occurring in a living body. For instance, hydrogen peroxide (H_2O_2) is formed in the human body as a by-product of many chemical reactions, such as the breakdown of fatty acids or cellular respiration.[9] The natural decomposition of H_2O_2 is very slow. Therefore, to make the decomposition of H_2O_2 faster, the catalase enzyme is used that decomposes 10^7 peroxide molecules per second. In cytochrome P450, the high valent iron active complex $[Por - Fe^{III}]$ undergoes oxidation in the presence of H_2O_2 and generates oxyferryl porphyrin cation radical, $[Por^{\cdot+} - Fe^{IV} = O]$

(Reaction I). The generated high valent iron complex, $[Por^{\cdot+} - Fe^{IV} = O]$, is responsible for oxidations in the cytochrome P450.[10] The complex thus formed immediately reacts with the second molecule of H_2O_2, forming O_2 and H_2O (Reaction II). The reaction with the second molecule of peroxide occurs at a very rapid rate, making it efficient in the presence of the catalase enzyme.[10]

Reaction-I: $Enz[Por - Fe^{III}] + H_2O_2 \rightarrow [Por^{\cdot+} - Fe^{IV} = O] + H_2O$

Reaction-II: $[Por^{\cdot+} - Fe^{IV} = O] + H_2O_2 \rightarrow Enz[Por - Fe^{III}] + H_2O + O_2$

1.3 Defining Efficiency

1.3.1 Turnover Frequency (TOF)

The primary concern across different types of catalysis lies in assessing the catalyst's efficiency, typically measured through turnover number (TON) and turnover frequency (TOF).[11] In 1966, Boudart defined that in heterogeneous catalysis, efficiency should be based on the catalytic activity relative to the number of exposed surface atoms of a specific type.[12] The author suggested a practical measure of catalytic activity could be expressed using TON, which indicates the number of reactant molecules converted per minute per catalytic site under specific reaction environments.[12] This definition later leads to the term "turnover frequency". In

recent times, although the term TOF is widely used, it does not have a proper definition. The IUPAC gold book has concisely defined TOF as *"commonly called the turnover number, N, and defined, as in enzyme catalysis, as molecules reacting per active site in unit time."*[13] Turnover frequency (TOF) refers to the rate at which a catalytic cycle completes, making it a key measure for comparing the reaction rates of different catalysts. Thus, TOF is defined as

$$TOF = \frac{reaction - rate}{N_{active-site}} = \frac{moles}{volume \times time}\frac{volume}{moles} = time^{-1} \tag{1.17}$$

where $N_{active-site}$ is the number of active sites per unit volume.

1.3.2 Challenges in Defining TOF

The kinetic nature of the catalyst and the complexity of the catalytic systems pose a significant challenge in predicting the efficiency of the catalyst. For catalytic reactions, the occurrence of side reactions and catalyst deactivation may significantly affect the yield of the reaction.[14] Thus, at an arbitrary time, the inevitable catalyst deactivation or other side reactions will pose a challenge in obtaining the actual yield. Therefore, measuring TOF is not straightforward.

Further, TOF is considered to be identical to the rate constant, as[11]

$$rate = TOF \times [Cat] \tag{1.18}$$

where *[Cat]* is the concentration of the catalyst.

Considering the reaction to be unimolecular,

$$R \rightarrow P \tag{1.19}$$

$$rate = -\frac{d[R]}{dt} \tag{1.20}$$

Therefore, from Eq. (1.18) and Eq. (1.20), TOF for the unimolecular reaction (TOF_1) is,

$$TOF_1 = rate \times \frac{1}{[Cat]} \tag{1.21}$$

$$or, \qquad TOF_1 = -\frac{d[R]}{dt} \times \frac{1}{[Cat]} \tag{1.22}$$

Further, on considering the same reaction as bimolecular, TOF for the reaction (TOF_2) can be expressed as

$$2R \rightarrow P \tag{1.23}$$

$$TOF_2 = -\frac{1}{2}\frac{d[R]}{dt} \times \frac{1}{[Cat]} \tag{1.24}$$

Therefore, from Eq. (1.22) and Eq. (1.24),

$$TOF_2 = \frac{1}{2} \times TOF_1 \tag{1.25}$$

$$or, \qquad TOF_1 = 2 \times TOF_2 \tag{1.26}$$

Thus, if a catalyst completes equal turns in the same time for both reactions, then mathematically, the bimolecular reaction consumes the reactant twice that of the unimolecular reaction. Since TOF varies with the number of turns in catalytic cycles, it should be the same for the same reaction irrespective of the molecularity. This creates an ambiguity in the definition of TOF.

In enzyme catalysis, the Michaelis-Menten reaction considers only one reactant. For this model, the TOF is independent of the species that reaches saturation. However, for other reactions of the catalytic cycle, reaching saturation may not be possible. If any reactants that have high concentrations are consumed at other steps of the catalytic cycle, the TOF may depend on the concentrations of those species.[11] Thus, in catalytic reactions, the concentration of the catalyst is lower than that of the reactants, and products are not sufficient conditions to define TOF. Rather than concentration, reaching the saturation regime is a more important condition for the reaction to define the TOF.

Further, at high concentrations, in catalytic reactions, the interaction between

species involved in the reaction affects their behavior. Therefore, in catalytic reactions, the concentration of the catalyst is lower than that of the reactants. Thus, for practical considerations, a low concentration of the catalyst is used and is diluted to infinite dilution conditions. The above discussion suggests that TOF is a bad descriptor in terms of the intrinsic rate of the reaction. Further, there is no standardized method to calculate the TOF.[11] In addition, TOF is a condition-dependent parameter. Therefore, defining TOF universally is difficult under different reaction conditions.

Moreover, for a reaction following first-order kinetics, the reactant concentration is asymptotic (tends to zero). Therefore, to consider the total catalyst consumption for a first-order reaction, the infinite time interval should be considered. In fact, the time required to consume 90% of the initial concentration will be different from that of the remaining 10% consumption.[11] As the TOF depends on the concentration of the reactant, defining the TOF for the first-order reaction creates confusion. In such cases, defining the TOF in terms of the instantaneous condition is more accurate. This led us to define the TON under half-life conditions to formulate theoretical catalytic models: (i) efficiency conceptualization model (ECM) [discussed in Chapter 2] and (ii) *MaxKinEff* model [discussed in Chapter 4].

1.3.3 Turnover Number (TON)

In assessing catalytic activity, besides the TOF, the TON is a crucial parameter that measures the stability of the catalyst.[11] In homogeneous as well as heterogeneous catalysis, TON has no dimension and represents the number of molecules produced before deactivation of the catalyst under the given reaction conditions per active site.[15] Consequently, it signifies the total number of turnovers achievable until the catalyst becomes inactive, irrespective of reaction duration. Theoretically, the "ideal catalyst" possesses exceedingly high (numerically becomes infinite) TON.[16] Thus, TON can also be interpreted as the maximum product yield obtained from an active catalytic site before activity decay for a particular reaction.

$$TON = \frac{N_{product}}{N_{active-site}} \tag{1.27}$$

Where $N_{product}$ is the number of product molecules formed per unit volume, and $N_{active-site}$ is the number of active sites per unit volume.

The TON and TOF are significant parameters to assess the efficiency of designed catalysts. The TON rendered by a designed catalyst often may not satisfy the targeted reaction. A notable limitation is the inability to foresee the TONs of many designed catalysts before proceeding with the reaction. Given this shortfall, formulating methods is necessary to anticipate TON and TOF.

1.4 Models for Catalytic Evaluation of Predicting Turning Over of Catalysts

Over the past two decades, computational calculation by analyzing the kinetics of reaction efficiency using various catalytic models has been demonstrated as a useful tool. Among them, computations with the energetic span model,[17−22] degree of rate control,[23,24] molecular volcano plots,[25−27] and micro-kinetic modeling[28] have been very beneficial. To analyze the efficiency involving single-step or multi-step reaction mechanisms, the discussion of the kinetics is established to be a powerful factor. While various models may diverge in their interpretations of efficiency, some prioritize analyzing catalytic cycles, while others favour evaluating catalytic activity based on the rate-determining step (RDS). However, for the reaction with a single catalytic turn (*i.e.*, a single turnover), the RDS may provide valuable information. In this section, details of the established catalytic models are discussed.

1.4.1 Energetic Span Model

The quantum mechanical kinetic model, namely the energetic span model, focuses on catalytic cycles.[17−19] An efficient catalyst demonstrates a substantial turnover frequency within its catalytic cycle. To calculate the accurate TOF of the catalyst involving an N-step catalytic process in the steady state regime, the rate constants,

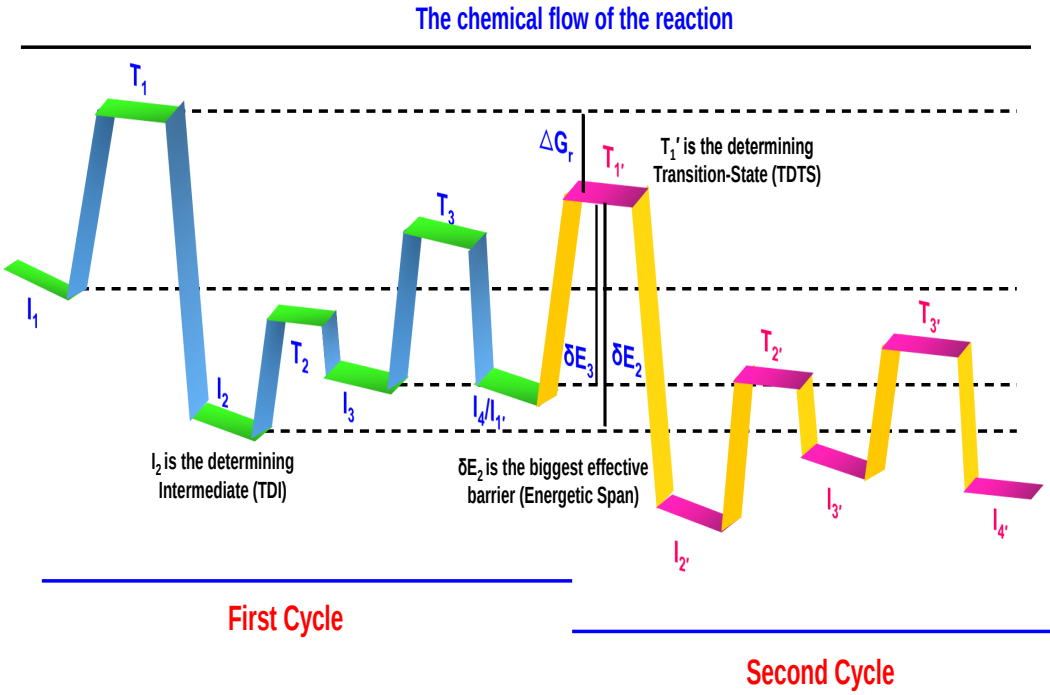

Figure 1.5: Schematic representation of the energetic span model. This figure is adapted from ref. 17 with permission © 2011 American Chemical Society.

k_i (k-representation), and the equilibrium constants (E-representation) in energetic terms are defined as[19]

$$k_i' = \frac{k_B T}{h}\, e^{\left(-\frac{\Delta G_i^{\neq}}{k_B T}\right)} = \frac{k_B T}{h}\, e^{\frac{G(I_{i-1})-G(T_i)}{k_B T}} \tag{1.28}$$

$$k_{-i}' = \frac{k_B T}{h} e^{\left(-\frac{\Delta G_{-i}^{\neq}}{k_B T}\right)} = \frac{k_B T}{h}\, e^{\frac{G(I_i)-G(T_i)}{k_B T}} \tag{1.29}$$

where $G(I_i)$ and $G(T_i)$ are the Gibbs free energy of the intermediates and tran-

sition states (TS), respectively. $G(I_{i-1})$ is the Gibbs free energy of the intermediate before the TS. Simplifying Eq. (1.28) and Eq. (1.29) as $I_i = \frac{G(I_i)}{k_B T}$, the standard state Gibbs energies of the intermediates and $T_i = \frac{G(T_i)}{k_B T}$, the standard state Gibbs energies of the transition states, the rate constants, k_i's in the unit of $\frac{k_B T}{h}$ ($\mathrm{k}_i = \mathrm{k}_i' \frac{k_B T}{h}$) can be defined as[19]

$$k_i = e^{I_{i-1} - T_i} \tag{1.30}$$

$$k_{-i} = e^{I_i - T_i} \tag{1.31}$$

In catalytic cycles, Eq. (1.30) represents the Christiansen's k-representation in the light of transition state theory (TST) that converts rate constants into energy levels.[29] On further mathematical simplification, Christiansen's k-representation demonstrates that the precise TOF can be calculated using the relation[17]

$$TOF = \frac{k_B T}{h} \frac{e^{\frac{-\Delta G_r}{RT}} - 1}{\sum_{i,j=1}^{N} e^{\frac{T_i - I_j - \delta G'_{i,j}}{RT}}} \tag{1.32}$$

Depending on the position of T_i's, $\delta G'_{i,j}$ will be

$$\delta G'_{i,j} = \begin{cases} \Delta G_r, & \text{if } \mathrm{T}_i \text{ appears before } \mathrm{I}_j. \\ 0, & \text{if } \mathrm{T}_i \text{ appears after } \mathrm{I}_j. \end{cases} \tag{1.33}$$

For an exothermic reaction, the second term ("-1 term") of the equation can be neglected. Further, in the denominator, only one term of summation dominates mostly. Thus, Eq. (1.32) simplifies to,

$$TOF = \frac{k_B T}{h} e^{-\frac{\delta E}{RT}} \tag{1.34}$$

$$\delta E = \begin{cases} T_{TDTS} - T_{TDI} & \text{if TDTS emerges after TDI.} \\ T_{TDTS} - T_{TDI} + \Delta G_r, & \text{if TDI emerges after TDTS.} \end{cases} \tag{1.35}$$

In Eq. (1.35), TDTS is the TOF-determining transition state (TDTS), and TDI is the TOF-determining intermediate. The δE obtained from Eq.(1.35) is the energy difference obtained between the TDTS and TDI, is reported as the driving force for the reaction. Upon the emergence of TDTS before TDI in the catalytic cycle, δE acts as the principal driving force behind the reaction and is equivalent to the activation energy of the cycle. However, if TDTS appears after the TDI, then the driving force ΔG_r is added to the δE.[17] Mathematically,

According to the energetic span model, the TOF in catalytic cycles is determined by a single transition state (TS) and one intermediate, TDTS and TDI, respectively. From many states that are present in the catalytic cycles, TDTS and TDI can be

tracked by assessing the degree of TOF control (X_{TOF})[17,20] given by

$$X_{TOF,i} = \left| \frac{1}{TOF} \frac{\partial (TOF)}{\partial E_i} \right| \tag{1.36}$$

where E_i is the energy of the TS or intermediate.

The higher value of X_{TOF} suggests a higher influence in the transition state or intermediate. On applying Eq. (1.36) to Eq. (1.32), the degree of TOF control can be defined as[17]

$$X_{TOF,T_i} = \frac{\sum_{j} e^{\frac{T_i - I_j - \delta G'_{i,j}}{RT}}}{\sum_{ij} e^{\frac{T_i - I_j - \delta G'_{i,j}}{RT}}} \tag{1.37}$$

$$X_{TOF,I_j} = \frac{\sum_{i} e^{\frac{T_i - I_j - \delta G'_{i,j}}{RT}}}{\sum_{ij} e^{\frac{T_i - I_j - \delta G'_{i,j}}{RT}}} \tag{1.38}$$

The energetic span model further describes that a single transition state or intermediate can not express the overall kinetics of the reaction. In contrast to rely on a solitary RDS, the energetic span model supports rate-determining states of the catalytic process. Considering the concentration factor, the model assumes that the reaction rate will accelerate if the reactant and the product are positioned between the TDTS and TDI.

1.4.2 Degree of Rate Control

Multi-step reactions are widespread in chemistry, in which the RDS has been demonstrated as a useful factor.[23] Formulating the rate law becomes straightforward once the RDS is located within a reaction sequence. Moreover, understanding the RDS aids in analyzing the reaction mechanism and optimizing reaction environments to improve the rate. To address a comparable objective, the degree of rate control (DRC) helps analyze the mechanistic and kinetic details.[23,24]

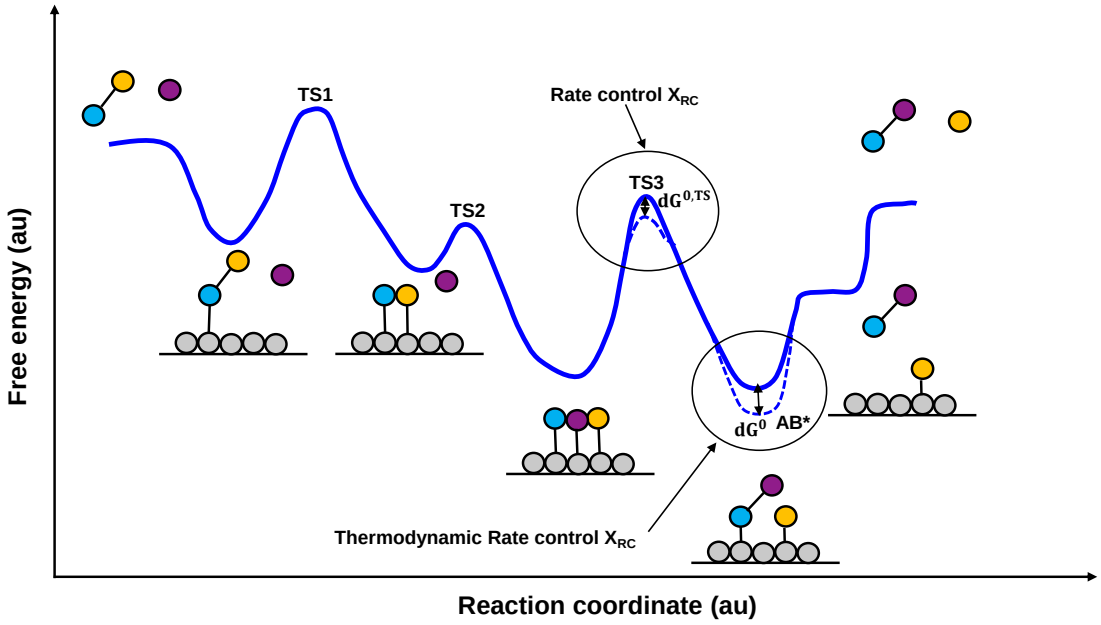

Figure 1.6: Illustration of the degree of rate control (DRC) in context to the catalytic pathway. Here, the blue, purple, and yellow circles indicate A, B, and C, respectively. The AB* is the intermediate formed in the reaction. This figure is adapted from ref. 32 with permission © 2017 American Chemical Society.

To illustrate the DRC and analyze the overall kinetics of the reaction, it is essential to have an idea of the individual elementary reaction kinetics. To elucidate a novel expression for the elementary step, i, the degree of rate control, $X_{RC,i}$, is expressed as[30,31]

$$X_{RC,i} = \frac{k_i}{r}\left(\frac{\partial r}{\partial k_i}\right)_{k_{j\neq i},K_i} = \left(\frac{\partial\, lnr}{\partial\, lnk_i}\right)_{k_{j\neq i},K_i} \tag{1.39}$$

Here, r denotes the rate of reaction for product formation, and k_j's are the corresponding rate constants, keeping it constant for all other steps j $\neq$ i. The K_i's are the corresponding equilibrium constants steps i.

Keeping the k_i's constant suggests that the forward and backward reactions are proceeding at equal rates. Eq. (1.39) indicates that for any ith-step, the proportional augmentation in the reaction rate (r) per incremental change in the k_i. The positive value of $X_{RC,i}$ delineates an increase in the rate constant, k_i enhances the net rate of the reaction, termed as the rate-limiting steps (RLS). On the other hand, $X_{RC,i} < 0$ will suggest the reaction step as an inhibition step. The parameters in Eq. (1.39) are kept constant to interpret $X_{RC,i}$ as a potential energy surface. Using transition state theory (TST) and taking the logarithm of both sides, we have[32]

$$k_i = \left(\frac{k_B T}{h}\right) exp\left(-\frac{\Delta G_i^{0,TS}}{RT}\right) \tag{1.40}$$

$$ln\, k_i = ln\left(\frac{k_B T}{h}\right) - \left(\frac{\Delta G_i^{0,TS}}{RT}\right) \tag{1.41}$$

On differentiating the k_i, we have[32]

$$d(ln\ k_i) = d\left(ln\left[\frac{k_B T}{h}\right]\right) - d\left(\frac{\Delta G_i^{0,TS}}{RT}\right) = -d\left(\frac{\Delta G_i^{0,TS}}{RT}\right) \tag{1.42}$$

Therefore, $X_{RC,i}$ can be written as the standard-state free energy of activation involved in the ith-step ($\Delta G_i^{0,TS}$) and standard-state free energy of the ith TS ($G_i^{0,TS}$)[30]

$$X_{RC,i} = \frac{k_i}{r}\left(\frac{\partial r}{\partial k_i}\right)_{k_{j\neq i},K_i} = \left(\frac{\partial\, lnr}{\partial lnk_i}\right)_{k_{j\neq i},K_i} \tag{1.43}$$

$$X_{RC,i} = \left[\frac{\partial\, ln\, r}{\partial(-\frac{\Delta G_i^{0,TS}}{RT})}\right]_{k_{j\neq i},K_i} = \left[\frac{\partial\, lnr}{\partial(\frac{-G_i^{0,TS}}{RT})}\right]_{G_{j\neq i}^{0,TS},G_m^0} \tag{1.44}$$

Eq. (1.44) illustrates $X_{RC,i}$ as the fractional alterations in $\Delta G_i^{0,TS}$ concerning the transition state for the ith step. This leads to a relative augmentation in the overall rate towards the desired product while maintaining constant standard-state free energies of the intermediate, $\Delta G_i^{0,i}$ and transition state, $\Delta G_i^{0,TS}$. The partial derivative in Eq. (1.44) is applied to preserve $\Delta G_i^{0,j}$, for all alternate TS j, where j $\neq$ i, while holding the intermediate m constant. This is analogous to maintaining k_j of all steps j, where j $\neq$ i, and K_j, of all steps, at an invariant j. The concept is elucidated further in Figure 1.6.

In the energy profile diagram of a reaction, the DRC is understood as the variation in k_i resulting from alterations in the energy of a maximum point. Thus, it

was proposed that DRC could encompass intermediates instead of solely TSs. An analogous concept, resembling the DRC, was subsequently posited and defined as[23]

$$X_{TRC,n} = \frac{1}{r}\left[\frac{\partial r}{\partial(\frac{-G_n^0}{RT})}\right]_{G^0_{m\neq n},G_i^{0,TS}} = \left[\frac{\partial\, lnr}{\partial(\frac{-G_n^0}{RT})}\right]_{G^0_{m\neq n},G_i^{0,TS}} \tag{1.45}$$

Considering G_m^0, G_n^0, and $G_i^{0,TS}$ constant for all intermediates with m $\neq$ n, the partial derivative was evaluated. $X_{TRC,i}$ denotes the proportional enhancement in the overall rate towards the target product for infinitesimal alterations. Originally, the degree of rate control was termed the degree of thermodynamic rate control due to the inherent thermodynamic nature of intermediate free energy. Since the terms are analogous, both are employed interchangeably for transition states, and intermediates are denoted simply as the degree of rate control.[32]

$$DRC_i = X_i = \frac{1}{r}\left[\frac{\partial r}{\partial(-\frac{G_i^0}{RT})}\right]_{G^0_{j\neq i}} = \left[\frac{\partial\, lnr}{\partial(\frac{-G_i^0}{RT})}\right]_{G^0_{j\neq i}} = \left[\frac{-\partial\, lnr}{\partial(\frac{G_i^0}{RT})}\right]_{G^0_{j\neq i}} \tag{1.46}$$

Eq. (1.46) connects the overall reaction rate and individual energy terms. Furthermore, considering the reactant as the reference state of zero standard-state free energy (G_i^0) and standard enthalpy, the G_i^0 can be expressed as the sum of an enthalpy component (ΔH_i^0) and an entropy component (- TΔS_i^0), represented as $G_i^0 = \Delta G_i^0 = \Delta H_i^0$ - TΔS_i^0, where Δ signifies differences relative to the reactants. As $\Delta H_i^0 = \Delta U_i^0$ + P(ΔV_i^0), variations in solvents cause infinitesimal changes in the molar

entropy and molar volume of all species i, resulting in T $\Delta\Delta S_i^0$ and P($\Delta\Delta V_i^0$) being substantially smaller than $\Delta\Delta U_i^0$. Consequently, $\Delta G_i^0 = \Delta U_i^0$, where Δ now denotes alterations induced by the modification.[32] Computational techniques such as density functional theory (DFT) coupled with experimental data enable the model to predict ΔS_i^0 using Eq. (1.46), facilitating quantitative assessment of the effects on the overall reaction rate and selectivity.

1.4.3 Microkinetic Modeling

To predict the reaction rates, the computation of the free energy barrier is an important parameter. However, to accurately calculate the reaction rate, the variation of free energy with concentration and time is the main objective of microkinetic modeling. In microkinetic modeling, the initial step involves assigning reaction rates to all elementary reaction steps by establishing a reaction network. The reaction rate governing each elementary step requires a differential equation that is numerically solvable using initial concentration conditions. Through the microkinetic model, a comprehensive depiction of concentration variations for each species over time is obtained.[28] For a microscopic reaction

$$\mathbf{n}_a\mathbf{A} + \mathbf{n}_b\mathbf{B} \underset{k_{rev}}{\overset{k_{fwd}}{\rightleftharpoons}} \mathbf{n}_c\mathbf{C} + \mathbf{n}_d\mathbf{D} \tag{1.47}$$

where k_{fwd} is the forward rate constant and k_{rev} is the backward rate constant of the reaction.

The reaction-rate (r) is expressed as[33]

$$r = \frac{1}{n_c}\frac{d[C]}{dt} = \frac{1}{n_d}\frac{d[D]}{dt} = -\frac{1}{n_a}\frac{d[A]}{dt} = -\frac{1}{n_b}\frac{d[B]}{dt} = k_{fwd}[A]^{n_a}[B]^{n_b} \tag{1.48}$$

The concentrations of species are related to the equilibrium constant K_{eq} by the equation[33]

$$K_{eq} = \frac{[C]^{n_c}[D]^{n_d}}{[A]^{n_a}[B]^{n_b}} = \frac{k_{fwd}}{k_{rev}} = exp\left(-\frac{\Delta G}{RT}\right) \tag{1.49}$$

where $\Delta G = \Delta G^{\ddagger}_{fwd}$ - $\Delta G^{\ddagger}_{rev}$, in which $\Delta G^{\ddagger}_{fwd}$ is the forward energy barrier and $\Delta G^{\ddagger}_{rev}$ is the reverse energy barrier. In the light of transition state theory (TST), considering the tunnelling corrections (κ), the reaction rate constant can be expressed as

$$k_{TST} = \frac{\kappa k_B T}{hc^o}\ exp\left(-\frac{\Delta G^{\ddagger}}{RT}\right) \tag{1.50}$$

where c^0 = standard concentration, $\Delta G^{\ddagger}$ is the Gibbs free energy of activation, k_B is the Boltzmann's constant, R is the universal gas constant, h is the Planck's constant, and T is the temperature.

For reactions beyond the zeroth order, the rate constant's value is contingent

upon the chosen reference state. When the energies of various species serve as the reference state, the free energy of activation of the respective species also undergoes alteration. The majority of the homogeneous catalytic process proceeds via a multi-step process from a pre-catalyst to product formation following different intermediates or adducts. For a multi-step catalytic process with intermediates INT_1, INT_2, and INT_3, the reaction scheme is shown as follows.

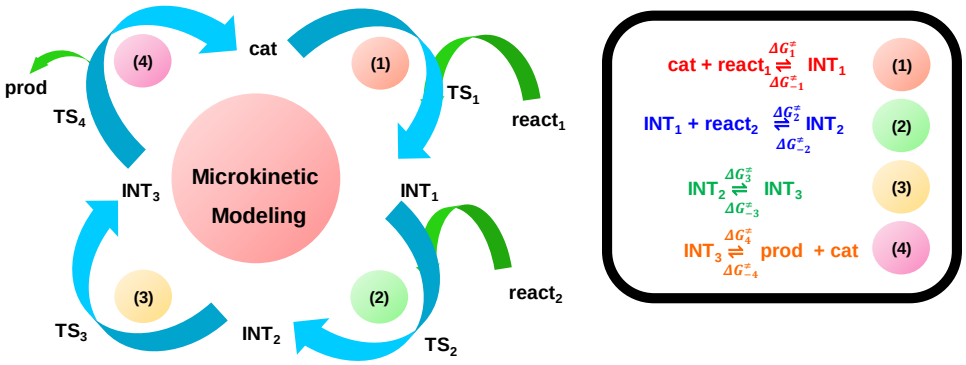

Figure 1.7: The catalytic cycle associated with free energies involved in the microkinetic modeling. This figure is adapted from ref. 28 with permission © 2018 John Wiley & Sons Inc.

Considering all the forward and reverse reactions, the following differential equations can be expressed[28]

$$\frac{d[cat]}{dt} = -k_1[cat][react_1] + k_{-1}[INT_1] + k_4[INT_3] - k_{-4}[cat][prod] \quad (1.51)$$

$$\frac{d[INT_1]}{dt} = k_1[cat][react_1] - k_{-1}[INT_1] - k_2[INT_1][react_2] + k_{-2}[INT_2] \quad (1.52)$$

$$\frac{d[INT_2]}{dt} = k_2[INT_1][react_2] - k_{-2}[INT_2] - k_3[INT_2] + k_{-3}[INT_3] \quad (1.53)$$

$$\frac{d[INT_3]}{dt} = k_3[INT_2] - k_{-2}[INT_3] - k_4[INT_3] + k_{-4}[prod][cat] \tag{1.54}$$

$$\frac{d[react_1]}{dt} = -k_1[cat][react_1] + k_{-1}[INT_1] \tag{1.55}$$

$$\frac{d[react_2]}{dt} = -k_2[INT_1][react_2] + k_{-2}[INT_2] \tag{1.56}$$

$$\frac{d[prod]}{dt} = k_4[INT_3] - k_{-4}[prod][cat] \tag{1.57}$$

The connection between the rate constant and the evolution of concentration can be predicted that facilitates the prediction of the qualitative dynamics of the system. However, predicting the outcomes from the free energy profile becomes complex for systems characterized by a complex reaction network in which different species exhibit different concentrations.[28]

1.4.4 Molecular Volcano Plot

In catalysis, volcano plots are considered a potent tool for optimizing the conditions of catalytic reactions.[25] The volcano plots originate from Sabatier's principle[34,35] which states that an ideal catalyst exhibits neither too strong binding nor too weak binding for the reactants. Historically, the concept was adopted by Gerischer[36] and Parsons[37] independently embraced this concept to elucidate the metallic activities in electrochemical H_2 evolution.

The contemporary volcano plot employs the descriptor variable (such as the hydrogen binding energy) in the abscissa, whereas, the observed catalytic activity is

along the ordinate. The generated plot will have the shape of a volcano that delineates how the descriptor variable correlates with catalytic activity.[25] The resulting volcano plot generally has three domains - (a) the right slope - too weak binding of the catalyst with the intermediates; (b) the left slope - too strong binding of the catalysts with intermediates; (c) the middle plateau region, termed as volcano plateau where catalysts exhibit intermediate binding affinities that are neither excessively strong nor excessively weak.[25] The catalysts on the plateau adhere to Sabatier's principle and are esteemed as optimal catalysts for a specific reaction.

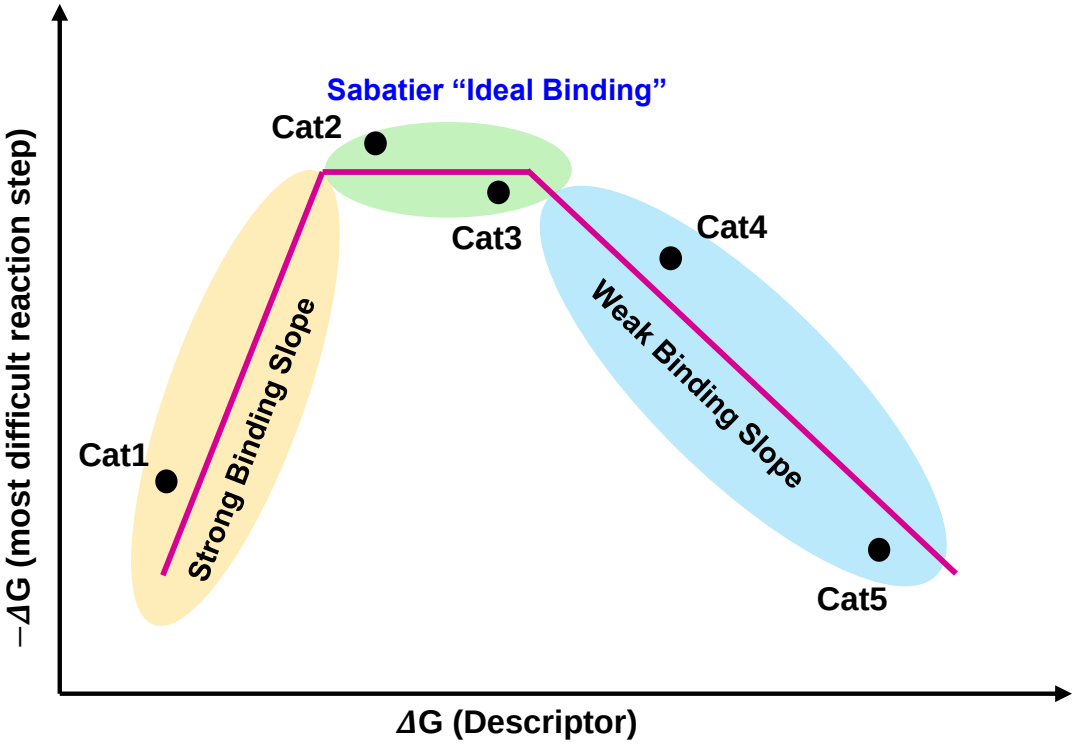

Figure 1.8: Representation of the volcano plot using Sabatier's principle. This figure is adapted from ref. 25 with permission © 2021 American Chemical Society licensed under CC-BY-NC-ND 4.0.

The volcano plots are classified mainly into two categories- (a) Thermodynamic Volcano and (b) Kinetic Volcano.

(a) Thermodynamic Volcano

The thermodynamic volcano plot is expressed by considering a homogeneously catalyzed reaction. From the chosen catalysts, the robust linear free energy scaling relationship (LFSR) delineates the relative free energies of distinct intermediates in the catalytic cycle. Thus, the relative energy of a particular intermediate with reference to the isolated catalyst and substrate will be the best descriptor variable.[27] Representing the energy of species involved in the reaction using the best descriptor variable and processing the LFSRs will result in a thermodynamic volcano plot. In the thermodynamic volcano plot, the ordinate consists of the descriptor variable, and the abscissa consists of ΔG values (< 0) belonging to the RDS.[27]

With individual relations, a unified thermodynamic picture of the reaction can be portrayed. With the information on the energy barrier of the most difficult step (potential-determining step, pds), it is easier to reveal the position of the specific volcano. The comprehension of a 3D volcano is enhanced through the amalgamation of 2D volcano plots, wherein the descriptor variable is plotted along the X-axis, -ΔG(pds) along the Z-axis, and the largest thermodynamic barrier on the Y-axis.[27] When the difficulty of the most difficult reaction step decreases, the value of the potential-determining step tends to decrease. This leads to narrowing the volcano

plateau with lesser ideal catalysts with thermodynamic profiles. Finally, the most difficult step becomes energetically feasible, leaving a single peak in which the right and left slopes are for other reactions of the catalytic reaction.[27]

(b) Kinetic Volcano

Apart from thermodynamic volcano, kinetics also plays a vital role in homogeneous catalysis. Hence, Wodrich *et al.* have designed "kinetic volcanoes" from a catalyst database.[27] The predicted activation barriers are derived with acceptable precision from the descriptor variable, replicating experimental trends observed with catalysts located near the summit of the volcano plot. On examining the LFSR, different scaling relationship results indicate the variances in the morphology of the ligand's bulk. By formulating identical volcanoes for each ligand, it has been observed that the decrease in the pivotal TS barrier enhances the steric bulk. The transition state barrier is defined as the largest energy difference between a connected intermediate and transition state found in the catalytic cycle, termed as the kinetic-determining step, kds and delineates the most active catalyst.[25] In addition, the relationship of different peaks from the different volcanoes is an estimate of steric bulk, which predicts the height of the volcano and determines the structure-activity relationship.[25]

1.5 Recent Developments on Theoretical Tools for Catalysis

The design and development of efficient catalysts may be forecasted only using the computations. Therefore, the rational design of catalysts is an essential criterion in modern chemical technology. Throughout the years, various efforts have been utilized to develop modern tools to enhance efficiency. Designing high throughput catalysts also includes tailoring the molecular structure or the ligand environment in chemical space. In an attempt to do so, Kalikadien *et al.* have recently developed a tool named *ChemSpaX*[38] to explore the chemical space through the automated functionalization of molecular scaffolds. The Python-based *ChemSpaX* explores the reactivity and stability of scaffolds by the systematic post-functionalization (PF) with multiple functional groups within the local chemical space. For exploring the chemical space, *ChemSpaX* suggested the automated placement of the substituents, keeping the original structure unchanged. Based on the input provided, the *ChemSpaX* inserts the substituents at the desired location of the scaffold and utilizes force-field (FF) optimization of the new substituents. The 3D coordinates of the complex may be utilized in *ChemSpaX*, provided the complex under study is catalytically active. Kalikadien *et al.* have applied *ChemSpaX* to generate ∼1100 Co-porphyrin structures as a representative application.[38] The geometries generated are optimized with GFN2-xTB

level of theories to compare with the *ChemSpaX*. The analysis of the results suggests that cartesian heavy-atom (all elements except H) root-mean-square deviation (hRMSD) utilized for comparison of different structures generated by different methods increases with an increase in the number of atoms. In the case of Mn-pincer complexes, it was reported that the geometries generated by using FF are comparable with the GFN2-xTB geometries. Therefore, these geometries may be used for training the machine-learning model to calculate the DFT-computed descriptor, such as HOMO-LUMO energy gap, to enhance the accuracy. Thus, *ChemSpaX* can be used satisfactorily to create local 3D space and extrapolated to generate a structure-property database. The database is helpful for the data-driven discovery of catalyst design.[38]

In a multi-component mixture, probing the chemical space during chemical transformations is challenging. Recently, Pidko and coworkers have developed an expert-bias-free graph-based network named Reaction Network Graph Theoretical Tool (*ReNeGaTe*)[39] for probing the automated mechanistic details in homogeneous catalysis. Given the reaction mixture input, to explore the mechanism, the graph-based network tool involves three key steps- thorough exploration of the conformer, finding the reaction event, and analysis of the reaction network. To recognize the crucial intermediates and the reaction event, root mean square deviation (RMSD) is used in the metadynamics studies to explore the conformers in the potential energy surface

(PES), which is subsequently analyzed within the framework of graph theory. The extensive reaction network was curtailed to a reaction-aware network that contains the species possessing the defined threshold energy. The reaction-aware network offers the understanding and the designing of experiments or high-level computations. The reaction network is freed from the expert bias in any of the above-mentioned three steps. However, chemical intuition is used only in selecting thermodynamic constraints guided by experimental conditions. To validate the strategy, Pidko and coworkers have considered the alkoxide base activation for (de)hydrogenation reaction with pre-catalyst manganese pentacarbonyl bromide $[Mn(CO)_5Br]$[40–42] and cis-N,N′-dimethyl-1,2-cyclohexanediamino manganese tricarbonyl bromide $[MnBr(CO)_3NN]$ complexes.[43,44] The results suggest that *ReNeGaTe* can identify the major and minor reaction pathways. The minor reaction paths were initiated by the activation of the catalyst which leads to sluggish catalyst deactivation. The pre-catalyst, $[MnBr(CO)_3NN]$, when reacts with the alkoxide base followed by subsequent ligand exchange produces the desired Mn-OR intermediate and several minor pathways. These minor pathways lead to the catalyst decomposition started by the nucleophilic attack of the alkoxide anion by the Mn-carbonyl group.

Reactivity analysis is another important aspect of catalysis. To do so, Hashemi *et al.*[45] have developed an automated tool — *HiREX*, for predicting the reactivity of transition metal catalysts. The tool first explores the chemical space around

each transition metal catalyst having unique morphology and then analyzes the large data set for enhanced reactivity. The results obtained are then analyzed using the *HiREX* workflow.[45] The *HiREX* workflow combines the *ChemSpaX*[38] for exploring the chemical space by post-functionalization and generates a database that serves as an input for the reactivity analysis using the *ReNeGaTe* workflow.[39] The chemical space around each catalyst was explored using the RMSD biased metadynamics simulations for the exploration of reactivity. With the structural and reactive properties as observable, the reactivity exploration results are arranged and analyzed to investigate the correlation between the chosen observables. This step is followed by the extraction of the reaction class for each catalyst. This automated and unbiased process helps define the reaction class based on the backbone and ligand modifications. The workflow assumes that the methods used for exploring chemical space are accurate and carry the errors resulting from the method used to describe the system. To identify the reactivity classes, a large database of the Mn-pincer complex[46] discovers relations between the structural and reactive properties and provides new pathways for the transformation of catalysts. The Mn-pincer catalysts with CNC (Carbon-Nitrogen-Carbon), PNN (Phosphorus-Nitrogen-Nitrogen), PNP (Phosphorus-Nitrogen-Phosphorus), and SNS (Sulphur-nitrogen-Sulphur) backbones show hemilability. Further, screening with the workflow identifies two new classes of reactivity- the carbonyl ligand undergoes nucleophilic attack, and the CF_3 groups

undergo migration. The CF_3 migration to the Mn-pincer catalyst corroborates the previous experimental findings. Thus, such an unbiased systematic workflow will open up new avenues in unveiling the reactivity patterns.

Selectivity in asymmetric catalysis is one of the crucial criteria.[44] The prediction of enantiomeric excess (*e.e.*) is one of the major parameters of interest. Although the computational methods are improved, uncertainty in the reaction mechanism and catalyst's nature may affect the accuracy. Owing to the complex behavior of the catalytic mechanism, the computed barrier of two enantio-determining steps determines the *e.e.* of the reaction, assuming the other steps have negligible influence on the reaction mechanism. To challenge such difficulty of the catalytic cycle, the microkinetic model provides the rate constants for the entire reaction and models its variations in the concentration. However, slight changes in the energy may affect the selectivity of catalysts. Therefore, with the assumption that DFT is accurate for the complete catalytic cycle, the work presents the accuracy of the *e.e.* prediction. Krieger *et al.* have defined *e.e.* as [44]

$$e.e. = \frac{|e^{-\frac{\Delta\Delta G^{\neq}}{RT}} - 1|}{e^{-\frac{\Delta\Delta G^{\neq}}{RT}} + 1} \tag{1.58}$$

In Eq. (1.58), $\Delta\Delta G^{\neq}$ is the difference in the barrier in a stereo-selective step forming R and S-enantiomer. Thus, with the information about the barrier, it is possible to determine the theoretical value of *e.e.*

To predict *e.e.*, Krieger *et al.* have considered a Noyori-type homogeneous Mn(I)-

diamine catalyst.[44] The *e.e.* during the progress of the reaction was calculated and compared to the concentration profiles from the microkinetic modeling.[28] The trajectory achieved and the *e.e.* of the reaction at different time intervals were compared with the experimental trajectories. The microkinetic modeling based on the DFT-computed energy profile suggests the maximum influence of the enantio-determining step in the selectivity of the reaction. In their work, Krieger *et al.* demonstrated that the *e.e.* becomes maximum when the barrier of formation of R-phenylethanol is decreased and S-phenylethanol is increased, making the $\Delta\Delta G = +10$ kJ mol^{-1} of two enantiomers. However, the minimum and inverse value of *e.e.* is obtained by lowering the barrier of S-phenylethanol and simultaneously increasing the barrier for R-phenylethanol. It was further reported that the inconsistency in the free energies for the stereo-inducing step has a prominent role in predicting selectivity. In addition, the alkoxide elimination step is also reported to affect the *e.e.* For instance, in alkoxide elimination, going through the R-isomer, the forward reaction is reported to be fifteen times faster than the backward reaction and, thus, contributes significant changes in *e.e.*[44]

Pidko and coworkers have designed another state-of-the-art unified approach to design and synthesize organometallic catalysts using chemical theory and computational screening, Death and Life of Catalysts (DeLiCAT).[47] The DeLiCAT is a hierarchical operando modelling approach that helps in understanding the variations

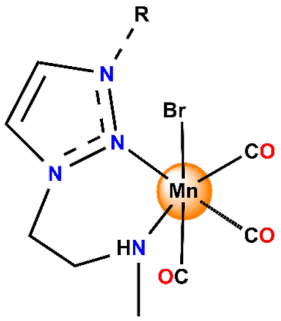

Figure 1.9: Mn-NHC catalyst for catalytic transfer hydrogenation (TH) of acetophenone.

in the reaction condition and behavior of a catalytic system. The model provides special importance to the side reaction occurring in catalysis. The catalyst deactivation is an unavoidable process that decreases the efficiency of catalysts. Due to the catalyst deactivation, the concentration of the catalyst decreases, and the reaction stops, leading to the "death" of the catalyst.

To exemplify the DeLiCAT, van Putten *et al.*[48] have shown the catalytic transfer hydrogenation (TH) of acetophenone using the Mn-NHC complexes. With 50 ppm Mn, the Mn-NHC catalyst [Figure 1.10] exhibits a very high TOF of 11.800 h^{-1} at 70 ^{o}C. However, when the reaction is set up at 60 ^{o}C, although the reaction is initially reported as slow, it crosses the integral TON (TON = 9600) of the reaction after $\sim$ 2.5 hours at 70 ^{o}C. After 76% of completion, the reaction reports 15.100 turnovers. Decreasing the catalyst loading (to 25 ppm) accelerates the deactivation process, and after 20 minutes, the TON cross-over takes place (TON = 1800). At this stage, the progress of the reaction stops at 8%, and the catalyst dies. Thus, the

catalyst deactivation pathway is a temperature-dependent process. On increasing the temperature of the reaction, the deactivation of the catalyst becomes more prominent than catalysis. Thus, for the same Mn-NHC catalyst, van Putten *et al.* have reported that with the same catalyst loading (50 ppm), the rate of deactivation was enhanced at 70 ^{o}C compared to 60 ^{o}C.[48] Thus, the reaction at the latter temperature becomes more efficient, leading to higher catalytic turnovers.

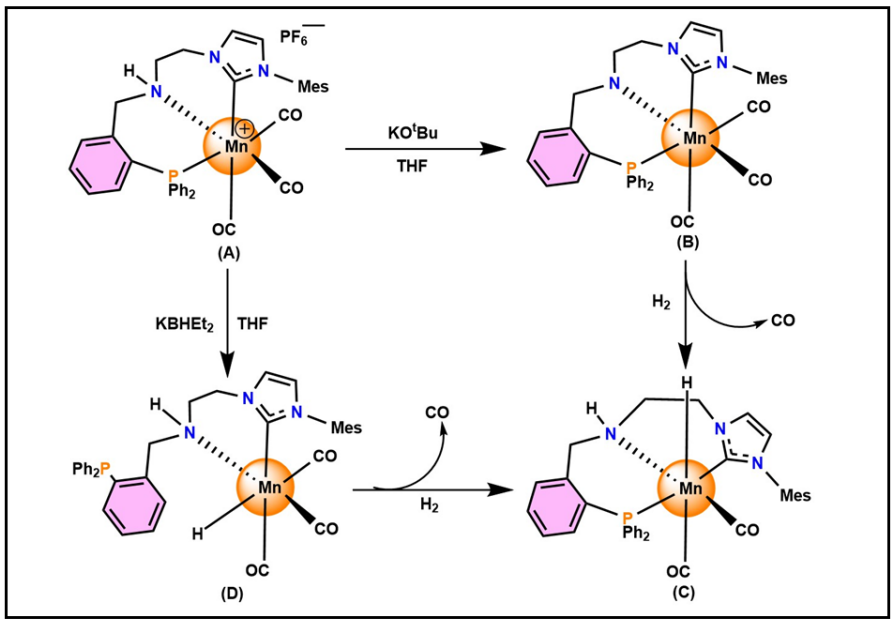

Figure 1.10: Schematic illustration of the addition of phosphine donor ligand to prohibit catalyst deactivation. This figure is adapted from ref. 49 (an open source).

Yang *et al.* have also established that tuning the ligand from monodentate to bidentate generates a robust pincer catalyst.[14] It was reported that attaching the bidentate CN ligand with a phosphine donor group activates the robust Mn-CNP catalyst, thereby regulating the deactivation of catalysts.[14,49] In Figure 1.10, the

metal complex ***A*** is cationic and forms complex ***B*** under basic environments. As complex ***B*** is coordinatively saturated, the elimination of one -CO ligand makes the complex unsaturated, and therefore, H_2 can bind to form a Mn-hydride complex ***C***. Since the replacement of CO is slow, the conversion from complex ***A*** to complex ***C*** is very slow. On the other hand, when the hydrogenation proceeds via complex ***D***, the rearrangement of the phosphine group (PPh_2) takes place. The PPh_2, being a strong donor, enables the dissociation of CO and accelerates the formation of complex ***C*** that is stable at high temperatures.[14,49]

1.6 Objective

The turning over of catalysts, *i.e.*, turnover frequency (TOF) and turnover number (TON) serve as a crucial metric for assessing the efficiency of catalysts under examination. The theoretical prediction of TON for a catalyst presents a difficult task. Designing a catalyst with a high TOF and TON for the targeted reaction is of extensive interest. Over the years, many catalysts have been designed and developed. However, the TON delivered by the designed catalysts may not satisfy the targeted reaction. Along the line, one of the major limitations lies in the fact that the TON of designed catalysts can not be predetermined. Considering the inadequacy, there is a need for the formulation of an approach to predict TOFs and TONs effectively.

In Chapter 2, we have derived the efficiency conceptualization model (ECM)

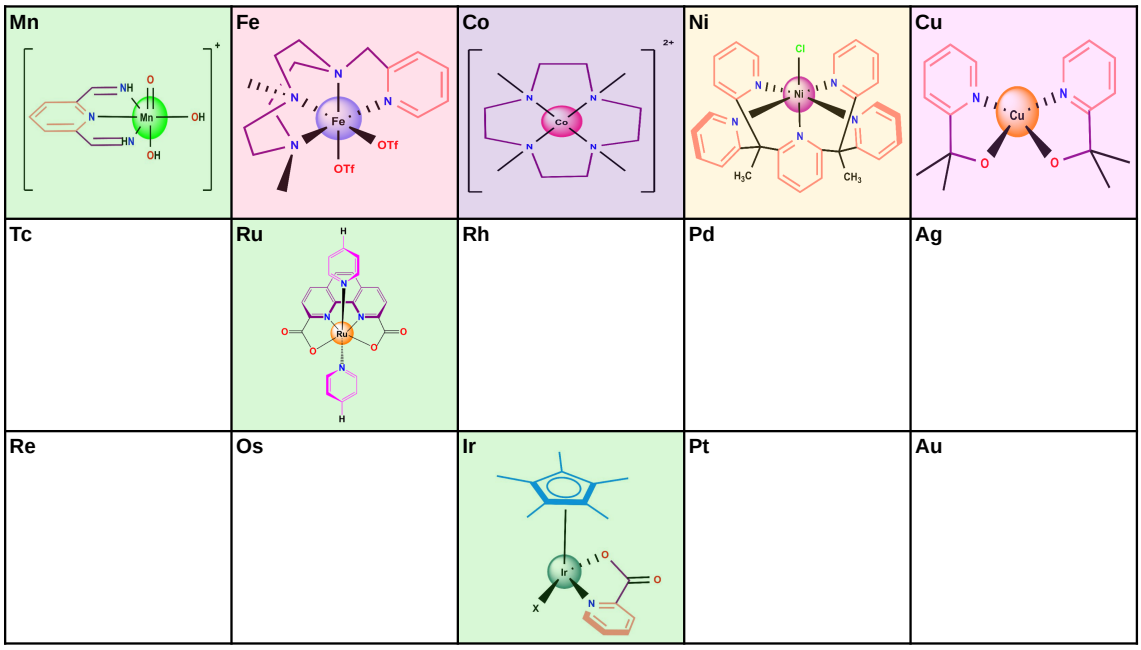

Figure 1.11: Schematic representation illustrating the positioning of 3d (Mn, Fe, Co, Ni, and Cu), 4d (Ru), and 5d (Ir) metals on the periodic table, utilized in crafting synthetic bio-inspired MWOCs. The elements in the empty boxes are inactive for molecular water-oxidation.

that uses quantum mechanical computations to evaluate efficiency through TOF and TON.[50] Considering the kinetic and thermodynamic aspects relevant to the rate-limiting step, the mathematical model calculates the turnover frequency, $\Gamma^0_{computed\ TOF}$, and the turnover number, $\tau^0_{computed\ TON}$. The model assumes that the feasibility of the reaction (ΔG_r) and the stability (α) of the associated adduct in the RDS influence both $\Gamma^0_{computed\ TOF}$ and $\tau^0_{computed\ TON}$. From a kinetic perspective, we incorporated the transition state theory (TST),[51] to calculate the reaction rate constant. The classical TST rate was corrected using the Eckart and Wigner tunnelling methods.[52–54]

For comparative purposes, the turnover number ($\tau^0_{computed\ TON}$) was defined under experimental conditions of temperature, pressure, and pH.

In Chapter 3, we calculated the rate constants for twenty-six catalysts using the transition state theory (TST). Among the twenty-six catalysts, thirteen Ru-based catalysts were from the 4d transition metals, while the remaining thirteen catalysts were from the first (3d) and third-row (5d) transition metals. The calculated rates were corrected by multiplying by the transmission coefficient (κ). We assessed the feasibility of each catalyst for the rate-determining O-O bond formation step and investigated the stability of the associated adduct considering the formation energy (E_f). The results were further confirmed with ab initio molecular dynamics (AIMD) simulations. Finally, we used these results in the ECM equation to compute the turnover numbers (TONs). The computed TONs were fitted with the experimental TONs to observe the correlation.

In Chapter 4, we demonstrate a kinetic model known as the Maximum Kinetic Efficiency (*MaxKinEff*).[55] This model is based on collision theory, which assumes that the catalyst and substrate behave as hard spheres. The *MaxKinEff* is straightforward and is designed to predict the maximum turnover frequency ($\Gamma^0_{max\ TOF}$). Furthermore, we have calculated the half-life of the catalyst ($t_{\frac{1}{2}}$). Based on these results, *MaxKinEff* determines the maximum turnover number of the catalyst ($\tau^0_{max\ TON}$) under half-life conditions.

In Chapter 5, the *MaxKinEff* assessed the validity of the model for thirteen Ru-based catalysts. The chosen ruthenium catalysts were varied with rigidity, substitution, and chelation. The chapter also investigated thirteen MWOCs based on 3d metals (from manganese to copper) and 5d metals (iridium). The first-row transition metals, due to their high abundance, are highly used as an active center for water-oxidation reaction. All catalysts were considered for water-oxidation reactions to predict the maximum turnover frequency ($\Gamma^0_{max\ TOF}$) and maximum turnover number ($\tau^0_{max\ TON}$) under the half-life ($t_{\frac{1}{2}}$) condition.

Chapter 6 illustrates the comparative discussion between the two catalytic models - the efficiency conceptualization model (ECM) and *MaxKinEff* model. The chapter discusses the similarities and differences in the methodology, assumptions of models, and application in terms of the twenty-six catalysts chosen for investigation.

Chapter 7 provides a summary of the thesis on the two catalytic models for predicting efficiency. The chapter concludes with the results observed for the water-oxidation reaction and discusses the significance of the two models. The chapter summarizes the limitations of both models and the possible future amendments to the models.

We believe the developed models applied to the water-oxidation will be helpful to the chemistry community due to their approach and practical utility. The models will help to forecast the catalytic efficiency before proceeding with experimental reactions.

2

Efficiency Conceptualization Model: A Method for Computing the Turnover of Catalysts

Quantum mechanical studies enable the detailed computation of the energy landscape of a catalytic cycle, allowing us to infer catalyst efficiency in terms of turnover numbers (TONs) and turnover frequencies (TOFs). However, predicting catalytic efficiency via TONs remains challenging. With the advent of the density functional theory (DFT), reliable quantitative computations have become possible. Modern researchers often use hybrid models, combining DFT with molecular mechanics (MM). Incorporating a tool that can accurately evaluate catalyst efficiency into this state-of-the-art approach would be highly valuable. Despite significant efforts to design methods with high TOFs, predicting these frequencies involves considerable inade-

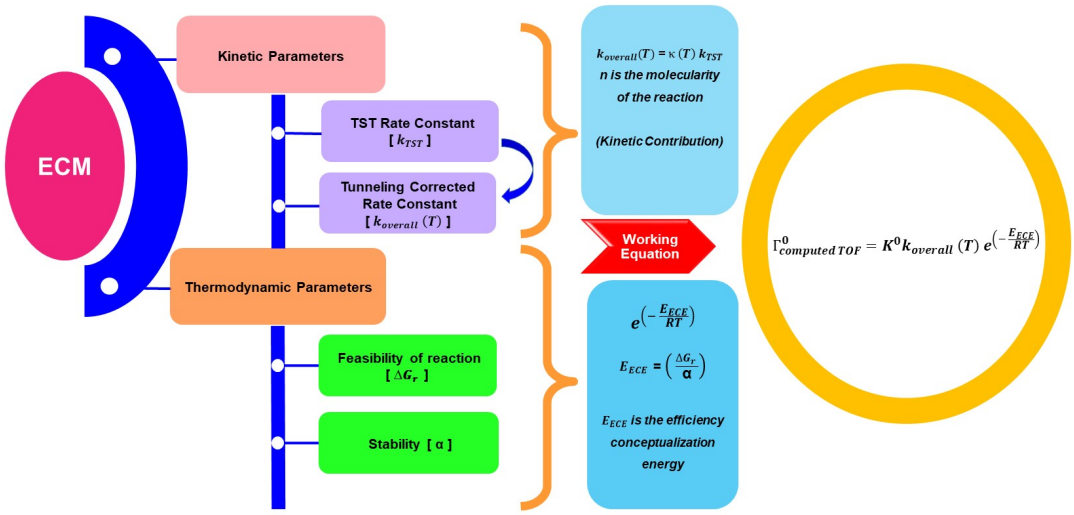

Figure 2.1: Roadmap to efficiency conceptualization model (ECM).

quacies. The theoretical methods or computational results are often anticipated to replicate experimental findings. However, it is worth mentioning that the connection between the theory and experiment is not always necessary and obvious as the "languages" of both the disciplines are different as noted by Kozuch *et al.*[17] Considering all the facts, in the current chapter, we illustrated the mathematical formulation of a model, namely the efficiency conceptualization model (ECM)[50] to compute TOF, $\Gamma^0_{computed\ TOF}$ based on the kinetic and thermodynamic perspectives involved in the rate-limiting process. The ECM will be extended to calculate the TON, $\tau^0_{computed\ TON}$. For a comparative study, we define TOF ($\Gamma^0_{computed\ TOF}$) under the experimental conditions of temperature, pressure, and pH.

2.1 Theory

2.1.1 Kinetic Perspectives: Rate Constants and Tunnelling Phenomena

For any rate-determining step (RDS) of a chemical reaction with molecularity n and rate constant, k_1,

$$\mathbf{nR} \xrightarrow{k_1} \mathbf{P}$$

The rate of the reaction depends on the concentration of the reacting species taking part in the RDS and can be expressed as

$$rate \propto [R]^n \tag{2.1}$$

$$rate = k_1[R]^n \tag{2.2}$$

In this expression, $[R]$ is the concentration of the reactant involved in the RDS.

The rate constant k_1 is derived from the transition state theory (TST)[51] and is given by

$$k_1 = \frac{k_B T}{hc^o}\ exp\left(-\frac{\Delta G_a}{RT}\right) \tag{2.3}$$

where c^0 = standard concentration of the reactant, ΔG_a is the standard Gibbs energy of activation, k_B is the Boltzmann's constant, R is the universal gas constant, h is

the Planck's constant, and T is the temperature.

The reaction coordinate for the targeted reaction may involve substantial motion of light atoms in its transition-state (TS) geometry. Therefore, one may consider the overall reaction rate constant, $k_{overall}(T)$, to include a significant contribution from light-atom tunnelling, even at room temperature (298.15 K). Considering this fact, the rate of the reaction is expressed as[56]

$$rate = \kappa(T)k_1[R]^n \tag{2.4}$$

$$rate = k_{overall}(T)[R]^n \tag{2.5}$$

where

$$k_{overall}(T) = \kappa(T)k_1 \tag{2.6}$$

where $\kappa(T)$ is the quantum mechanical transmission coefficient.

To compute the transmission coefficient, $\kappa(T)$, the ECM considers the one-dimensional Eckart[52,53] and Wigner[54] tunnelling methods. The $\kappa(T)$ can be computed with the Wigner tunnelling method given by[57]

$$\kappa(T) = 1 + \frac{1}{24}\left(\frac{h\omega^*}{k_B T}\right)^2 \tag{2.7}$$

In Eq. (2.7), ω^* is the imaginary frequency of the TS involved in the RDS.

However, the Wigner tunnelling method fails to consider the barrier height of the reaction profile and, therefore, is inadequate to evaluate $\kappa(T)$.[57] Hence, the Eckart tunnelling method is a viable alternative to calculate the $\kappa(T)$, addressing the barrier height. Thus, in the RDS, within the realm of the Eckart tunnelling method, the $\kappa(T)$ can be expressed as the ratio of thermally averaged quantum tunnelling probability to the quasi-classical transmission probability.[57] Therefore,

$$\kappa(T) = \frac{\int_{E_0}^{\infty} P^T(E) e^{-E/k_B T}}{\int_{E_0}^{\infty} P^C(E) e^{-E/k_B T}} \tag{2.8}$$

In Eq. (2.8), E_0 is the ground vibrational state energy of the stationary points (reactant or product) at 298.15 K, and E is the system's total energy. P^C(E) is the probability obtained from the TST rates, and P^T(E) is the quantum tunnelling probability. The P^T(E) can be defined as[57]

$$P^T(E) = 1 - \left[\frac{cosh[2\pi(\alpha - \beta) + cosh[2\pi\delta]}{cosh[2\pi(\alpha + \beta) + cosh[2\pi\delta]}\right] \tag{2.9}$$

The ratio defined in Eq. (2.9) can be evaluated to represent the quantum tunnelling probability of light atoms or molecules.[57]

In Eq. (2.9),

$$\alpha = \frac{4\pi}{\omega^*}\left[\sqrt{\frac{1}{\sqrt{\mathrm{V_f}}}} + \sqrt{\frac{1}{\sqrt{\mathrm{V_r}}}}\right]^{-1}\sqrt{\mathrm{E}} \tag{2.10}$$

$$\beta = \frac{8\pi^2}{\mathrm{h}\omega^*}\left[\sqrt{\frac{1}{\sqrt{\mathrm{V_f}}}} + \sqrt{\frac{1}{\sqrt{\mathrm{V_r}}}}\right]^{-1}\sqrt{\mathrm{E} - \mathrm{V_f} + \mathrm{V_r}} \tag{2.11}$$

$$\delta = 4\pi\left[\frac{\mathrm{V_f V_r} 2\pi}{(\mathrm{h}\omega^*)} - \frac{1}{16}\right]^{\frac{1}{2}} \tag{2.12}$$

where V_f is the energy of the forward barrier, V_r is the energy of the reverse barrier, and E is the system's total energy.

With the obtained zero-point corrected forward and reverse energy barriers, the tunnelling corrected rates, $\mathrm{k}_{overall}(T)$, were solved by numerically integrating probability, $P^T(\mathrm{E})$ over Boltzmann distribution energy (dE),[52,57] as shown in Eq. (2.13)

$$k(T) = \frac{1}{k_B T}\, e^{\Delta E_f / k_B T} \int_0^\infty P^T(E) e^{-E/k_B T} dE \tag{2.13}$$

where ΔE_f is the zero-point corrected forward energy barrier integrated over the total energy, E of the system.

A reaction with a higher value of $\mathrm{k}_{overall}(T)$ suggests a faster catalytic cycle.[17] Increasing the $\mathrm{k}_{overall}(T)$ suggests more cycles over the same time (defined as TOF, $\Gamma^0_{computed\ TOF}$) completed by the catalyst.[11] Therefore, the $\Gamma^0_{computed\ TOF}$ of a catalyst

varies directly to $k_{overall}(T)$ of the reaction as

$$\Gamma^{0}_{computed\ TOF} \propto k_{overall}(T) \tag{2.14}$$

For an elementary reaction, in addition to the yield of the reaction, the performance of the catalyst is defined by the improvements in the kinetic behaviour. In ECM, while dealing with the elementary RDS, the kinetic behaviour of the catalysts was improved on the incorporation of the tunnelling corrected rate constants, which is directly proportional to the turnover frequency (TOF) of catalysts. Thus, the kinetic perspective of ECM discusses the performance of the catalysts.

2.1.2 Thermodynamic Perspectives

To compute turnover frequency, $\Gamma^{0}_{computed\ TOF}$, the dependence on the kinetic and thermodynamic parameters is the basic assumption of the efficiency conceptualization model (ECM). In the RDS, when the catalyst, $\boldsymbol{M}$, reacts with a reactant, $\boldsymbol{R}$, the association between the two species forms an associated adduct, ***[R-M]***, as shown below.

$$\boldsymbol{R} + \boldsymbol{M} \rightarrow \boldsymbol{[R\text{-}M]} \tag{2.15}$$

In ECM, we introduced a new thermodynamic energy term for RDS, efficiency conceptualization energy, E_{ECE}. ECM proposed that E_{ECE} is the thermodynamic driving

force of the reaction that depends upon two factors- change in the Gibbs free energy of the RDS, $\Delta G_{r,RDS}$ and stability (α) of the associated adduct, ***[R-M]***. ECM suggests that to be an efficient catalyst, the value of E_{ECE} has to be minimized.

The $\Delta G_{r,RDS}$ is expressed as

$$\Delta G_{r,RDS} = G_{[R-M]} - (G_R + G_M) \tag{2.16}$$

Here, G_R, G_M, and $G_{[R-M]}$ are the Gibbs free energies of the reactant, catalyst, and associated adduct, respectively.

When the Gibbs free energy of the reaction ($\Delta G_{r,RDS}$) is more negative, the feasibility of the reaction increases. On decreasing the $\Delta G_{r,RDS}$ of the reaction, the catalyst will complete more turns. Thus, over the same time, the TOF of the catalyst increases. However, ECM proposes that increasing the TOF of the catalyst requires decreasing the value of E_{ECE}. Therefore,

$$E_{ECE} \propto \Delta G_{r,RDS} \tag{2.17}$$

During the RDS, different catalysts will have different computed free energies (G_M). Similarly, different products formed in the RDS will also have different values of computed Gibbs free energy ($G_{[R-M]}$). Since G_M and $G_{[R-M]}$ have different values for different catalysts, according to Eq. (2.16), the $\Delta G_{r,RDS}$ is different for different

catalysts.

The formation energy, E_f, for the reaction is expressed as

$$E_f = E_{[R-M]} - (E_R + E_M) \tag{2.18}$$

Here, $E_{[R-M]}$ is the energy of the associated adduct, E_R is the energy of the reactant, and E_M is the energy of the catalyst. Since E_f is a measure of the stability, α of the associated adduct formed in the reaction, from now onwards, we denote E_f as α.

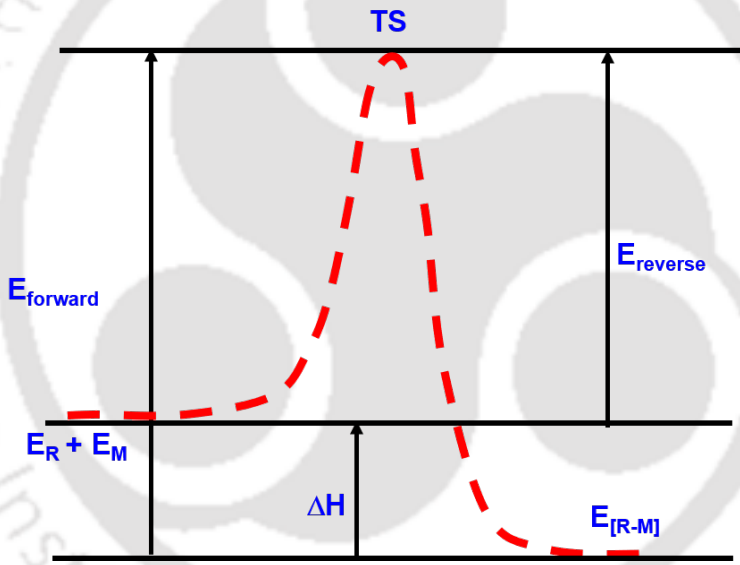

Figure 2.2: A schematic energy profile for an exothermic reaction

From Figure 2.2 and Eq. (2.18), we have

$$E_f = E_{[R-M]} - (E_R + E_M) = \Delta H \tag{2.19}$$

Further, from Figure 2.2, enthalpy is the difference between the forward energy barrier ($E_{forward}$) and reverse energy barrier ($E_{reverse}$).

$$\Delta H = E_{forward} - E_{reverse} \tag{2.20}$$

Therefore, from Eq. (2.19) and (2.20), E_f can also be related to the kinetic barriers of the energy profile as $E_f = E_{forward}$ -$E_{reverse}$.

According to the Bell–Evans–Polanyi (BEP) principle, the activation energy varies linearly with changes in enthalpy of the elementary reaction.[58] An exothermic reaction indicates the increased stability of the associated adduct. Therefore, when the energy of the associated adduct decreases, according to the BEP principle, the activation energy also decreases. As a result, over the same time, the catalyst with lower activation energy will take more turns and accordingly exhibit higher TOF. Thus, the stability of the associated adduct increases the TOF of the catalyst. However, according to ECM, increasing the TOF of the catalyst requires decreasing the value of E_{ECE}. Therefore, when a more stable associated adduct is formed, the value of E_{ECE} decreases. Thus, α varies to E_{ECE} as

$$E_{ECE} \propto \frac{1}{\alpha} \tag{2.21}$$

However, the excessive stability of the catalytically active intermediate can contribute

to catalyst deactivation. If the reactant binds too tightly with the catalyst, the irreversible binding of the catalyst in the associated adduct makes the reaction highly exothermic and will stabilize it sufficiently. These lead to loss of catalyst activity over time and, eventually, catalyst poisoning. Deactivation is an inevitable process. However, it may be slowed down or prevented. Therefore, optimum binding between the reacting species is necessary to facilitate catalysis.

Thus, by combining Eqs. (2.17) and (2.21),

$$E_{ECE} \propto \left(\frac{\Delta G_{r,RDS}}{\alpha}\right) \tag{2.22}$$

$$E_{ECE} = \left(\frac{\Delta G_{r,RDS}}{\alpha}\right) \times E^{o} \tag{2.23}$$

Here, E^0 is the proportionality constant and remains identical for a given reaction under standard conditions of temperature and pressure.

2.1.3 Computing Turnover Frequencies

The ratio of the amount of product formed per unit time, $\boldsymbol{N}$, to the amount of catalyst used, $\boldsymbol{N}_0$, *i.e.* $\left(\frac{N}{N_0}\right)$, defines the TOF of catalysts.[59] The amount of catalyst used delineates the number of catalytic sites participating in the reaction. Thus, on

increasing $\left(\frac{N}{N_0}\right)$, the $\Gamma^0_{computed\ TOF}$ of a catalyst also increases.

$$\Gamma^0_{computed\ TOF} \propto \left(\frac{N}{N_0}\right) \tag{2.24}$$

Among the available $\boldsymbol{N_0}$ catalyst molecules, all molecules may not lead to product formation. ECM approximates that the probability of the effective number of product molecules formed per catalyst molecule per unit time, $\left(\frac{N}{N_0}\right)$ must possess the minimum thermodynamic energy, E_{ECE}, to drive the catalytic reaction successfully. Thus, similar to the Boltzmann distribution,

$$\left(\frac{N}{N_0}\right) \propto exp\left(-\frac{E_{ECE}}{RT}\right) \tag{2.25}$$

Thus, from Eq. (2.24) and Eq. (2.25), we can have

$$\Gamma^0_{computed\ TOF} \propto exp\left(-\frac{E_{ECE}}{RT}\right) \tag{2.26}$$

Therefore, by combining Eq. (2.14) and Eq. (2.26), we have

$$\Gamma^0_{computed\ TOF} \propto k_{overall}(T) \times exp\left(-\frac{E_{ECE}}{RT}\right) \tag{2.27}$$

$$\Gamma^0_{computed\ TOF} = K^0 k_{overall}(T) \times exp\left(-\frac{E_{ECE}}{RT}\right) \tag{2.28}$$

In Eq. (2.28), the value of K^0 is taken to be 1 unit under standard temperature and pressure conditions. However, depending on the reaction environments and kind of reaction, the value of K^0 may vary.

2.1.4 Predicting Half-lives and Turnover Numbers

To calculate the half-life of the catalyst, it is necessary to understand the catalyst deactivation. Let us consider a reaction scheme

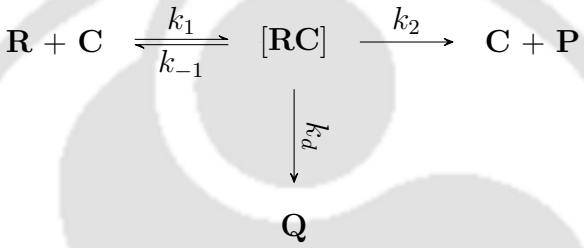

In the reaction, k_1 and k_{-1} are the rate constants for the forward reaction and the backward reaction. On the other hand, k_2 and k_d are the rate constants for product formation and catalyst deactivation, respectively. At equilibrium, for homogeneous catalysis

$$[R]_0 = [R] + [RC] \tag{2.29}$$

Further, the equilibrium constant, $K^{\neq}$ is given by,

$$K^{\neq} = \frac{k_1}{k_{-1}} = \frac{[RC]}{[R][C]} \tag{2.30}$$

$$\implies \frac{k_1}{k_{-1}}[R][C] = [RC] \tag{2.31}$$

Replacing ***[RC]*** in Eq. (2.29),

$$[R_0] = [R] + \frac{k_1}{k_{-1}}[R][C] \tag{2.32}$$

$$\implies [R_0] = [R]\left(1 + \frac{k_1}{k_{-1}}[C]\right) \tag{2.33}$$

$$\implies [R_0] = [R](1 + K^{\neq}[C]) \tag{2.34}$$

$$\implies [R] = \frac{[R]_0}{(1 + K^{\neq}[C])} \tag{2.35}$$

Applying the steady-state approximation on ***[RC]***,

$$\frac{d[RC]}{dt} = 0 \tag{2.36}$$

$$Or, \qquad k_1[R][C] - k_{-1}[RC] - k_2[RC] - k_d[RC] = 0 \tag{2.37}$$

$$\implies k_1[R][C] = (k_{-1} + k_2 + k_d)[RC] \tag{2.38}$$

$$\implies [RC] = \frac{k_1[R][C]}{(k_{-1} + k_2 + k_d)} \tag{2.39}$$

If the deactivation barrier is very high and catalysis is dominant, then k_d is very small. Thus, $k_d << k_2$, and $k_2 >> k_{-1}$. Therefore, in such cases, deactivation may be ignored and is more apparent at low concentrations. Thus, $k_{-1} + k_2 + k_d \cong k_2$.

Therefore, Eq. (2.39) changes to

$$[RC] = \frac{k_1[R][C]}{k_2} \tag{2.40}$$

The rate of the reaction is

$$Rate = k_2[RC] \tag{2.41}$$

Replacing Eq. (2.40) in Eq. (2.41),

$$Rate = \frac{k_2 k_1[R][C]}{k_2} = k_1[R][C] \tag{2.42}$$

In terms of catalyst concentration, the rate can be expressed as

$$Rate = -\frac{d[C]}{dt} = k_1[R][C] \tag{2.43}$$

On replacing Eq. (2.35) in Eq. (2.43),

$$-\frac{d[C]}{dt} = \frac{k_1[R]_0}{1+K^{\neq}[C]}[C] \tag{2.44}$$

$$\implies \frac{1+K^{\neq}[C]}{[C]}d[C] = -k_1[R_0]dt \tag{2.45}$$

$$\implies \int_{C_0}^{C_t}(\frac{1}{[C]}+K^{\neq})\,d[C] = -\int_0^t k_1[R]_0 dt \tag{2.46}$$

$$\implies ln\frac{[C]_t}{[C]_0} + K^{\neq}([C]_t - [C]_0) = -k_1[R]_0(t-0) \tag{2.47}$$

$$\implies ln\frac{[C]_0}{[C]_t} - K^{\neq}([C]_t - [C]_0) = k_1[R]_0 t \tag{2.48}$$

At t $\longrightarrow t_{\frac{1}{2}}$; [C]$_t$ $\longrightarrow \frac{[C]_0}{2}$

$$ln\frac{[C]_0}{\frac{[C]_0}{2}} - K^{\neq}(\frac{[C]_0}{2} - [C]_0) = k_1[R]_0 t_{\frac{1}{2}} \tag{2.49}$$

$$\implies ln\,2 + K^{\neq}(\frac{[C]_0}{2}) = k_1[R]_0 t_{\frac{1}{2}} \tag{2.50}$$

$$\implies 2ln\,2 + K^{\neq}[C]_0 = 2k_1[R]_0 t_{\frac{1}{2}} \tag{2.51}$$

$$\implies t_{\frac{1}{2}} = \frac{2ln\,2 + K^{\neq}[C]_0}{2k_1[R]_0} \tag{2.52}$$

In Eq. (2.52), [R]$_0$ is the initial concentration of the reactant, and [C]$_0$ is the initial concentration of the catalyst. k$_1$ is the forward rate constant, which can be evaluated using the transition state theory (TST) [Eq. (2.3)].

Thus, using the values of $\Gamma^0_{computed\ TOF}$ [Eq. (2.28)] and half-life of the catalysts

($t_{\frac{1}{2}}$) [Eq. (2.52)] in Eq. (2.53), we obtained the TON, $\tau^0_{computed\ TON}$ of the twenty-six catalysts using the relation[11] ,

$$\tau^0_{computed\ TON} = \frac{\Gamma^0_{computed\ TOF} \times t_{\frac{1}{2}}}{ln\ 2}, \tag{2.53}$$

under experimental conditions of temperature, pressure, and pH.

2.2 Concluding Remarks

Based on the kinetic and thermodynamic perspectives, we mathematically formulated a catalytic model - ECM to compute TOF ($\Gamma^0_{computed\ TOF}$) of catalysts for any targeted reaction under experimental conditions of temperature, pressure, and pH. For computing the efficiency of catalysts, ECM focuses on the RDS of the reaction and is applicable for any reaction, regardless of the molecularity of the reaction. To consider the kinetic effects, we have calculated the rate constants for the rate-determining step (RDS) using the transition state theory (TST) followed by the correction of rate constants incorporating the Eckart and Wigner tunnelling correction methods. However, ECM assumes that the Wigner tunnelling corrected method is not suitable for predicting the TOFs and TONs of the catalyst as it does not account for the barrier height of the reaction. Further, ECM demonstrates that the TOF of a catalyst is governed not only by the rate constants of the reaction but also by the thermodynamic feasibility ($\Delta G_{r,RDS}$) of the reaction and the stability (α) of the associated-adduct

in the RDS, measured in terms of formation energy (E_f) of the bond formation process. ECM integrates the two thermodynamic parameters and introduces the term efficiency conceptualization energy (E_{ECE}), the threshold thermodynamic energy of a catalyzed reaction. The smaller value of E_{ECE} suggest greater TOF of the reaction. Thus, the TOF obtained from ECM was extended to predict the TON of catalysts following the Eq. (2.53) by providing the value of $t_{\frac{1}{2}}$ calculated using Eq. (2.52).

We hope the computational approach to the ECM will be a useful tool for catalysts and chemists. This strategy provides a lucid mathematical framework to unravel catalysts' TOF and TON. Currently, the ECM is implemented under experimental temperature, pressure, and pH. However, these conditions may be varied, and accordingly, the expressions may be amended as required. Further, catalyst deactivation will be extended in the future, and accordingly, the ECM strategy will be amended. Discussions in this context will be elaborated to provide a more detailed understanding of the turnover of catalysts. These discussions will initially focus on TOFs and TONs, with an application to the molecular water-oxidation reaction.

3

Implementation of ECM: An Application to the Transition Metal-Catalyzed Water-Oxidation Reaction

3.1 Introduction

The turnover number (TON) is a crucial metric for assessing the efficiency of designed catalysts. However, the TON achieved by a given catalyst often falls short of the intended reaction. It has always been challenging to reproduce the experimental TONs computationally. To address this, we have developed the efficiency conceptualization model (ECM) strategy, which employs quantum mechanical computations to evaluate efficiency in terms of TON. For comparative analysis, we define the turnover

frequency, $\Gamma^0_{computed\ TOF}$ and turnover number, $\tau^0_{computed\ TON}$ under specific experimental conditions, including temperature, pressure, and pH.

To examine the validity of ECM, we focus on the mononuclear transition-metal-catalyzed water-oxidation reaction, which has significant potential in artificial photosynthetic energy-conversion technology. We considered twenty-six mononuclear transition-metal catalysts for our study. The rate determining step (RDS) of the reaction is found to be the formation of the O-O bond between the metal-oxo complex and the water molecule.[50] The evolution of the mononuclear transition-metal water-oxidation catalysts is presented below.

3.2 The Molecular Water-Oxidation Reaction

To address global energy challenges, artificial water splitting is considered a potential alternative for clean and green energy.[60,61] However, this process is energetically demanding ($\Delta G = 237\,\mathrm{kJ/mol}$)[62] that necessitates the design of a robust and efficient catalyst capable of facilitating the loss of $4H^+/4e^-$ and the simultaneous formation of an O-O bond.[63] The half-cell reactions occurring at both electrodes are presented as follows[62]

At Cathode: $2H_2O \longrightarrow 4H^+ + 4e^- + O_2$

At Anode: $4H^+ + 4e^- \longrightarrow 2H_2$

Overall Reaction: $2H_2O \longrightarrow 2H_2 + O_2$ (E^0=1.23 eV vs. NHE)

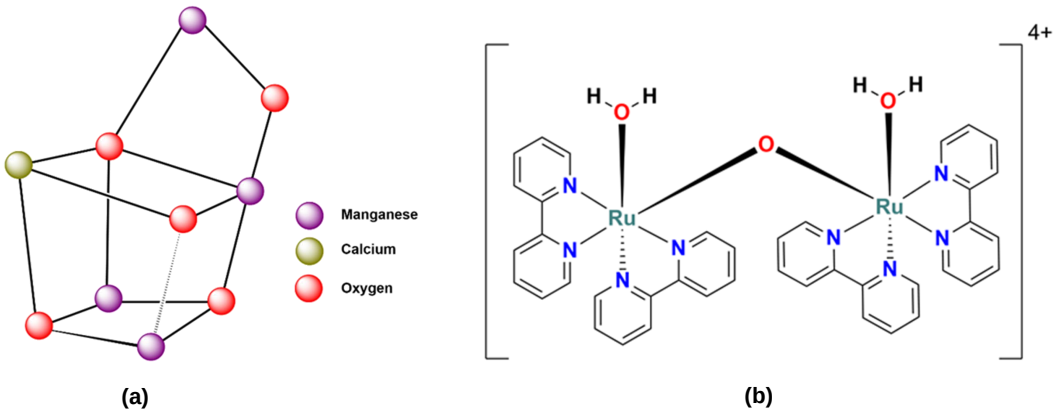

Figure 3.1: (a) Natural multi-metallic Mn_4CaO_5 core of oxygen-evolving center (OEC); (b) Blue dimer, *cis, cis*-$[Ru^{II}(bpy)_2(H_2O)]_2(\mu\text{-}O)]^{4+}$.

In recent decades, extensive efforts have been dedicated to understand the synthesis of natural photosynthetic systems, mechanisms, electronic structures, oxidation states, and spectroscopic properties.[64–71] Concurrently, *in vitro* development of robust catalysts with high TONs and lower overpotentials has been undertaken to achieve the goal of mimicking natural photosynthesis.[72–82]

3.2.1 Evolution of Ru-based Molecular Water-Oxidation Catalysts

Among various mononuclear transition metal catalysts, ruthenium (Ru) active centres have garnered significant attention due to their well-defined structures[83–87] and their diagonal relationship to manganese (Mn) centres.[60,88] Pioneering work by Meyer and coworkers introduced the first biomimetic catalyst, the blue dimer (BD), cis, cis-$[Ru^{II}(bpy)_2(H_2O)]_2(\mu\text{-}O)]^{4+}$ [Figure 3.1(b)], which set the stage for the development

of numerous water-oxidation catalysts.[89–91] The success of the blue dimer highlighted the critical role of proton-coupled electron transfer (PCET) processes and underscored the importance of stable polypyridine ligands capable of withstanding strong oxidative conditions.

Initially, the success of the blue dimer led researchers to hypothesize that multiple metal centres were necessary for effective synthetic water-oxidation catalysts, as these centres were thought to facilitate the four-electron accumulation required for water-to-oxygen conversion. However, subsequent work by Llobet and his team introduced a catalyst, $[Ru^{II}_2(bpp)(tpy)_2(H_2O)_2]^{3+}$ (complex **4**), with a rigid Hbpp [Hbpp = 2,6-bis(pyridyl)pyrazole] backbone, following similar design principles.[92] Thummel and colleagues further expanded on this approach by investigating a series of Ru-based water-oxidation catalysts featuring rigid polypyridyl-based equatorial and axial pyridine-based ligands, as illustrated in complex **5** [Figure 3.2].[93,94]

The Thummel group's groundbreaking discovery of a mononuclear complex **6** capable of catalyzing water-oxidation was particularly notable.[94] This finding demonstrated that O-O bond formation via the water nucleophilic attack (WNA) pathway leading to the generation of $[Ru^{V}{=}O]^{3+}$ species, thereby proving that one active center could be adequate for water-oxidation catalysis.[95] Further validation came from Meyer *et al.*, who confirmed that a single metal center was sufficient for water-oxidation using the ruthenium complex $[Ru^{II}_2(tpy)(bpy)(H_2O)]^{3+}$.[96] These pivotal

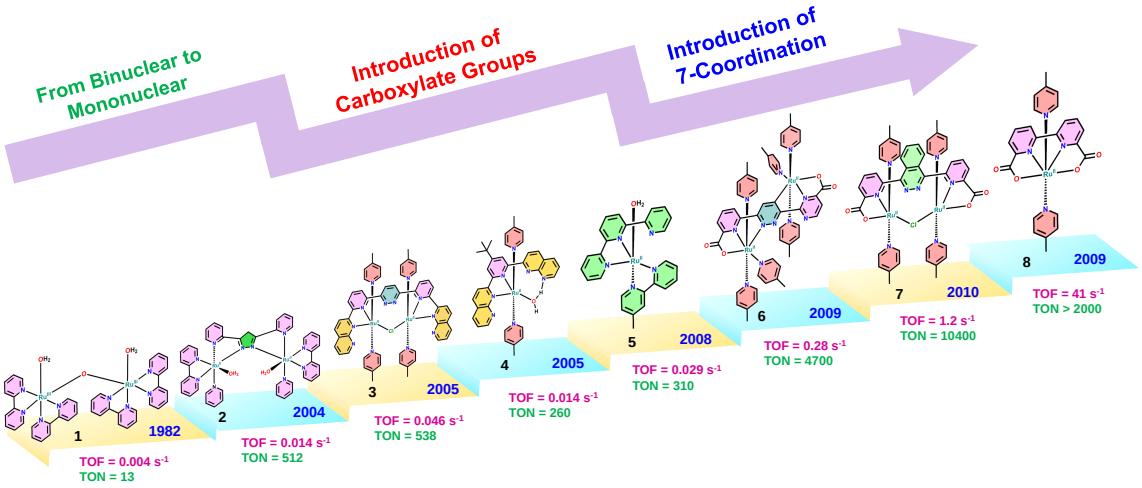

Figure 3.2: Illustration of the evolution of the MWOCs with ruthenium active centers with their TONs and TOFs under highly acidic conditions (pH = 1) using the Ce^{IV} oxidant.

discoveries have paved the way for the synthesis of MWOCs, extending beyond Ru-based systems.[97–99]

Among the various Ru-based catalysts, those based on carboxylates have been extensively studied due to their distinctive morphology. A significant breakthrough in this area was the discovery of the $[Ru(bda)(pic)_2]$ complex (where bda stands for 2,2′-bipyridine-6,6′-dicarboxylate and pic stands for 4-picoline), which demonstrated a turnover number (TON) more than 2000.[100] This finding revolutionized the field by suggesting that a single active center could suffice for complete water-oxidation, contrary to the previous belief that multiple metallic centers were necessary. Additionally, the complex exhibited an overpotential of 180 mV, comparable to natural photosystem II.[99]

Table 3.1: Overview of the historical advances in the Ru-based MWOCs.[92–96]

MWOCs	TONs	Synthesized By
1	13	Meyer (1982)
2	512	Llobet (2004)
3	538	Thummel (2005)
4	260	Thummel (2005)
5	310	Meyer/Sakai/Berlingutte (2008)
6	4700	Sun and Åkermark (2009)
7	$>$ 2000	Sun (2009)
8	10400	Sun (2010)

The Ru-bda catalysts are further distinguished by the proton-accepting properties of the carboxylate groups and the wide O-Ru-O cleft of 123°, which is significantly larger than the ideal octahedral angle.[100] This wide bite angle facilitates the binding of incoming ligands to the metal center, leading to the formation of seven-coordinated species that exhibit enhanced catalytic performance. These attributes make Ru-bda catalysts highly promising candidates for water-oxidation applications.

3.2.2 Mechanistic Understanding of Ru-based MWOCs

The Ru-based water-oxidation catalysts follow two major mechanistic pathways. While some catalysts follow the water nucleophilic attack (WNA) pathway,[98,100–103] other

catalysts follow the radical coupling two metal-oxo moiety (I2M) pathway.[104–109] For the ruthenium catalysts with bda backbone, $[Ru(bda)(pic)_2]$ was reported to follow the second-order kinetics with respect to the catalyst, indicating an I2M mechanism. Nevertheless, when the equatorial ligand is changed from bda to pda (1,10-phenanthroline-2,9-dicarboxylic acid), the catalysts switch to the WNA pathway over the I2M pathway.[110] The schematic representations of both mechanisms are shown in Figure 3.3.[98,100–103,110]

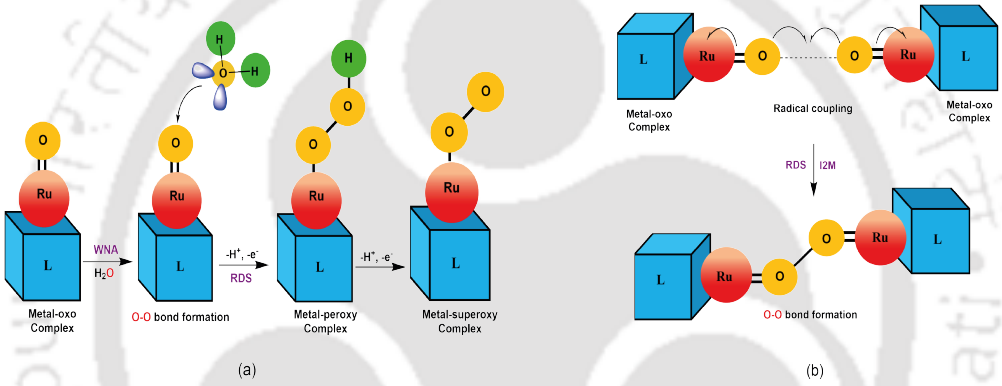

Figure 3.3: O-O bond formation process via (a) water nucleophilic attack (WNA) mechanism. (b) radical coupling (I2M) mechanism. (RDS = Rate determining step; L = Ligand).

In the context of the WNA mechanism, the catalyst initially binds a water molecule at its active site. To efficiently reach a high oxidation state, the catalyst is activated through multiple proton-coupled electron transfers (PCET) that require minimal energy, forming a metal-oxo species.[102,111,112] This high-valent metal-oxo complex, $[M^V{=}O]$, plays a crucial role in determining both the stability and activity of the

metal complexes and initiates the pathway for the formation of the O-O bond.[102] The resulting [M^{V}=O] species is typically electrophilic and exhibits reduced spin density in the oxo moiety. These metal-oxo complexes feature a low-lying, lowest unoccupied molecular orbital (LUMO) that is accessible for the substrate water molecule to participate in O-O bond formation. Following the formation of the O-O bond, the complex undergoes rapid conversion, generating a metal hydroperoxide intermediate (M—OOH) with the metal in a lower oxidation state. The final step involves the evolution of O_2, completing the cycle with lower energy requirements compared to the preceding reaction steps.[102] The detailed mechanism for water-oxidation with Ru-center is illustrated in Figure 3.4.

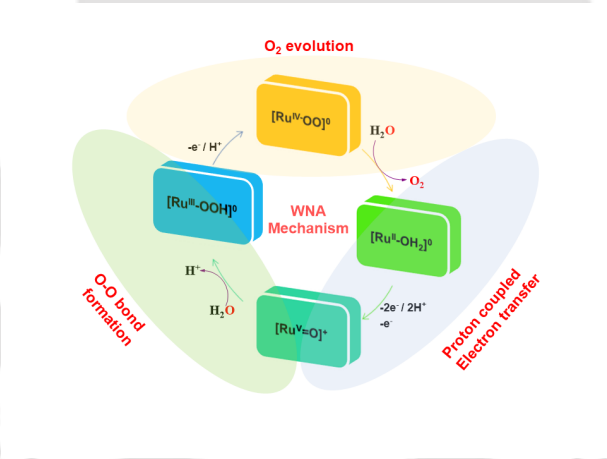

Figure 3.4: Schematic illustration of the molecular water-oxidation reactions.

Regarding the stability and reactivity of [M^{V}=O] complexes, these properties are contingent upon the ligand environment and the metal center. When an oxo ligand (O^{2-}) coordinates with the metal center, it induces a distortion in the molecular

symmetry from O_h to C_{4v} due to the shortened M=O bond length. This distortion destabilizes the d_{z^2} orbital, as illustrated in Figure 3.5.[112] The electronic structure projected by this configuration allows for a rational determination of the stability and reactivity of $[M^V{=}O]$ complexes based on their *d*-electron count. Transition metals (TM) characterized by intermediate *d*-electron counts are particularly effective at generating reactive metal-oxo complexes because they possess suitable vacant d orbitals capable of accepting electrons donated by the $2p_x$ and $2p_y$ orbitals of the oxo ligand. This rationale supports the selection of ruthenium (Ru) for developing synthetic MWOCs.[113]

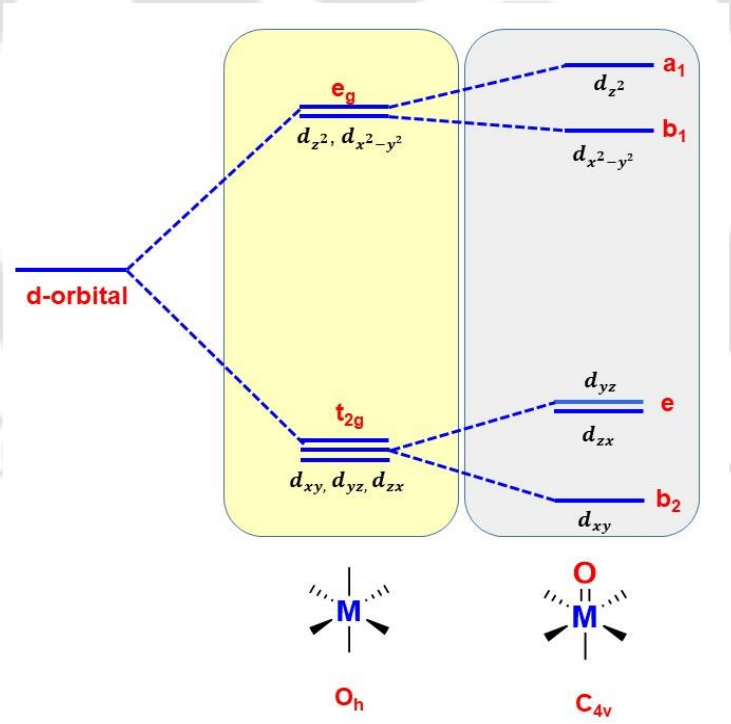

Figure 3.5: Schematic representation of (a) the splitting of d-orbital in O_h and C_{4v} environment.

3.2.3 First (3d) and Third (5d)-Row Transition Metal-based Molecular Water-Oxidation Catalysts

The employment of first-row transition metals in designing proficient molecular catalysts for water-oxidation draws significant research interest due to their plentiful availability and economical cost. The design of MWOCs with these metals is hindered by their substitutional lability. Thus, the ligands attached to such metals can be substituted by water or solvents. However, the original precursor complexes frequently break down into catalytically active metal oxide particles that precipitate out. Consequently, investigations into water-oxidation catalysts utilizing first-row transition metals must be meticulously assessed to ensure that metal oxide particles do not take part as catalysts for water-oxidation. To surmount these obstacles, ligands must be modified with a robust affinity for metal ions, even in aqueous environments, to facilitate and stabilize higher oxidation states.

Nevertheless, to mimic the natural PSII and to improve the design and efficiency of water-oxidation catalysts, there is a high interest in the transition elements. Third-row (5d) transition metals such as iridium (Ir) are esteemed for their exceptional catalytic activity and resilience in water-oxidation. Conversely, ubiquitous and economical first-row (3d) transition metals can also affect water-oxidation under milder conditions. A plethora of research has been undertaken on

catalysts incorporating manganese (Mn),[72−74,114] iron (Fe),[115−118] cobalt (Co),[119,120] nickel (Ni),[81,121] and copper (Cu),[80,122−124]. Nonetheless, these catalysts frequently necessitate a high formal oxidation state, positioning first-row elements as more apt catalytic systems relative to their ruthenium (Ru)-based counterparts. However, the reasonable design and synthesis of water-oxidation catalysts with 3d-transition metals as the active center require further exploration.

Furthermore, only a limited number of first-row transition metals can efficiently catalyze water-oxidation in the presence of cerium ammonium nitrate (CAN) as the oxidizing agent.[63,92] Numerous MWOCs composed of metals that are abundant on earth exhibit functionality for electrocatalytic or photocatalytic water-oxidation under neutral or alkaline conditions.[121,125−127] However, the true nature of the catalysts under such circumstances is still debated. Only Fe-based MWOCs have been extensively documented to catalyze the oxidation of water with the sacrificial oxidant CAN, similar to ruthenium and iridium catalysts.[115]

In the Figure 3.6, (a) MWOC-1: $[Ru(pda)(py)_2]$; (b) MWOC-2: $[Ru(pda)(pic)_2]$; (c) MWOC-3: $[Ru(pda)(Br\text{-}py)_2]$; (d) $[Ru(bpy)(tpy)Cl]^+$ derivatives with MWOC-4: R= -H ; MWOC-5: R = Methyl (-Me) ; MWOC-6: R= Methoxy (-OMe) ; MWOC-7: R= Nitro ($-NO_2$) ; and MWOC-8: R= Ethoxycarbonyl (-COOEt) ; (e) MWOC-9: $[Ru(tpy)(bpy)(pic)]^{2+}$; (f) MWOC-10: $[Ru(bpy)_3]^{2+}$; (g) MWOC-11: $[Ru(tpy)(pic)_3]^{2+}$; (h) MWOC-12: $[Ru(tpy)_2]^{2+}$; (i) MWOC-13: $[Ru(dpp)(pic)_2]^{2+}$;

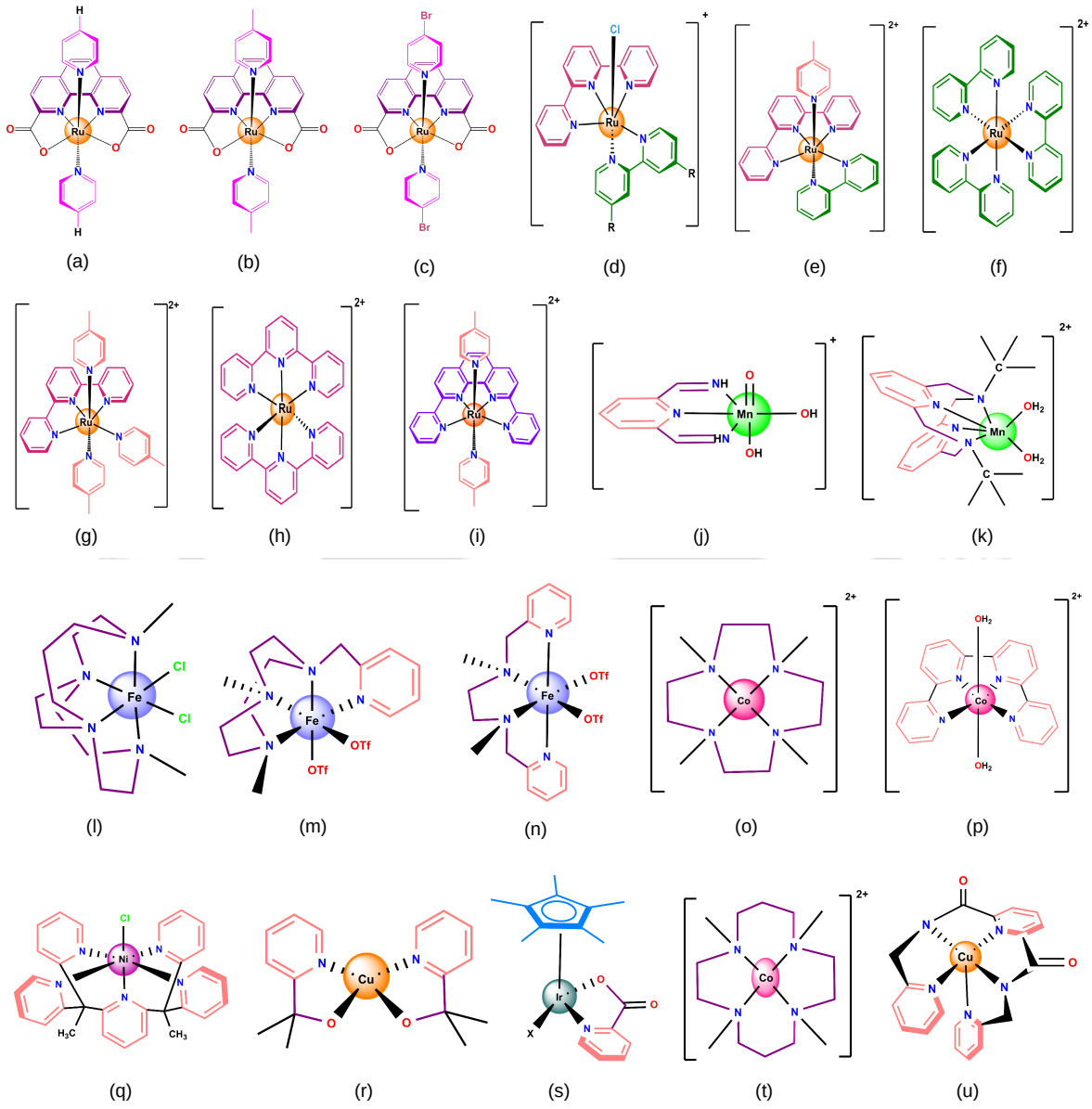

Figure 3.6: Structures of twenty-six representative molecular water-oxidation catalysts.

(j) MWOC-14: $[Mn(Py)(O)(OH)_2]^+$; (k) MWOC-15:$[Mn(Py)_2NR_2(H_2O)_2]^{2+}$] with R = ^{t}Bu ; (l) MWOC-16: cis-$[Fe(cbc)Cl_2]^+$; (m) MWOC-17: $[Fe(OTf)_2(Me_2Pytacn)]$; (n) MWOC-18: $[Fe(OTf)_2(mep)]$; (o) MWOC-19: $[Co(12\text{-}TMC)]^{2+}$; (p) MWOC-20: trans-$[Co(qpy)_2(OH_2)_2]^{2+}$; (q) MWOC-21: Ni-PY5 ; (r) MWOC-22: $[Cu(pyalk)_2]$; (s) $[Cp^*Ir(\kappa^2\text{-}N,O)X]$ with MWOC-23: X = Cl ; and MWOC-24: X = NO_3 ; (t) MWOC-25: $[Co(13\text{-}TMC)]^{2+}$; (u) MWOC-26: $[Cu(Py_3P)]$.

3.3 Systems Under Investigation

3.3.1 Ruthenium (Ru)-based Molecular Catalysts

To evaluate the strategy, we analyzed thirteen experimentally synthesized Ru-based molecular water-oxidation catalysts (Ru-MWOCs)[7,128,129], illustrated in Figure 3.6 (a) - (i). These selected Ru-MWOCs exhibit diverse structural, electronic, and chelating properties, and all follow the WNA mechanism.[7,100,129] Catalysts MWOC-1 to MWOC-3 [Figure 3.6 (a)-(c)] are monomeric carboxylate-based catalysts,[7,100,128] while MWOC-4 to MWOC-8 [Figure 3.6 (d)] have the general formula of $[Ru(bpy)(tpy)Cl]^+$ (bpy = 2,2′-bipyridine; tpy = 2,2′;6,2″-terpyridine) and differ in their functional groups.[129] The carboxylate catalysts (MWOC-1 to MWOC-3) are more planar with C_{2v} symmetry, and due to the closer spacing of the two metal-coordinated oxygen donor atoms in the pda system, these units are prone to distortions. The crystallographic analysis revealed that the O-Ru-O angle for the rigid equatorial pda sys-

tems is 130.5°.[7] In contrast, MWOC-9 to MWOC-13 [Figure 3.6 (e)-(i)] represent chelating complexes with varying ligand rigidity. The reduction potential (E^0) for the catalysts is below 120 mV except for MWOC-13, which reports $E^0 > 120$ mV. For such catalysts, with the original ligands being intact, it isn't easy to imagine a seven-coordinated complex. Hence, such catalysts accept two electrons to form a more reactive 16-electron species, making the ruthenium center electrophilic.[100] The reduced 16-electron form of the catalyst is potent to react with the water and generate the seven coordinated Ru(IV) complex with an L-Ru-L (L = Ligand) bite angle less than 90° thereby creating strain in the Ru(dpp) and Ru(tpy) molecules.[100]

3.3.2 Manganese (Mn)-based Molecular Catalysts

The reactivity of the oxygen-evolving complex (OEC) in water-oxidation has garnered significant attention for the development of catalysts aimed at solar-driven water-oxidation, especially those incorporating cost-effective and earth-abundant first-row transition metals. Manganese plays a vital role in biological oxygen chemistry, particularly at the active centers of oxygen-generating enzymes like manganese catalase (MnCAT) and the OEC of Photosystem II.[130] In this study, we utilized a pertinent six-coordinate model system of $[Mn^{V}{=}O]$ along with high-spin Mn^{II} pyridinophane complexes $[Mn^{II}(py_2NR_2)(H_2O)_2]^{2+}$ (R = ^{t}Bu) [Figure 3.6 (j) - (k)] to promote O_2 formation.[73]. The pyridinophane macrocycle offers donor functionality akin to

that of certain open-chain aminopyridine ligands, which facilitate the electrochemical oxidation of Mn^{II}–OH_2 complexes into [Mn^{IV}-(μ-O)$_2$ Mn^{IV}] dimers under alkaline conditions.[131] Mechanistic studies reveal that this oxidation process is coupled with proton transfer from the aqua ligands, echoing the behaviour of water-oxidation catalysts that generate [M^V=O] intermediates via PCET events.[73]

3.3.3 Iron (Fe)-based Molecular Catalysts

Nonheme iron complexes serve as efficacious model catalysts for the activation of oxygen and the oxo-functionalization of hydrocarbons.[132] Within these catalytic processes, the intermediates formed by nonheme iron catalysts include Fe=O and Fe–OOH species, which facilitate the formation of O–O bonds.[115] Thus, the nonheme homogeneous iron complexes with water coordination sites were proven by Fillol in 2011.[115] The activity of such catalysts is reported to be higher than the tetraamido macrocyclic ligands (TAMLs), composed of high-valent metal ions. In the current chapter, we have considered the nonheme iron catalysts [Figure 3.6 (l) - (n)] proposed by Fillol *et al.*[115]

3.3.4 Cobalt (Co)-based Molecular Catalysts

Designing cobalt catalysts for water-oxidation under oxidative conditions has proven to be obscured, as pre-catalyst complexes are susceptible to degradation.[133] Upon degradation, cobalt-based complexes yield Co^{2+}/Co^{3+} ions, forming hydroxide (with

or without oxide) complexes that can efficiently catalyze water-oxidation reactions and release oxygen.[134] In this study, we investigated monomeric water-soluble Co(IV) complexes [Figure 3.6 (o), (p), and (t)], which facilitate water-oxidation at a remarkably low oxidation potential of 1.23 V versus NHE at pH 6.[119,120] The extraordinary catalytic efficiency of these cobalt complexes is attributed to the unique environments surrounding the single Co sites. The deprotonated alkoxide linkers integrated into the bipyridine coordination framework form a desirable tetradentate ligand structure that tightly envelops the Co(IV) center.[119] This configuration ensures a stable, catalytically active Co coordination environment, preventing significant structural distortion regardless of the cobalt center's valence state during reactions.[120]

3.3.5 Nickel (Ni)-based Molecular Catalysts

Most reported water-splitting catalysts are proficient in catalyzing only one of the two half-reactions involved in water splitting, with a scarcity of catalysts capable of facilitating water-oxidation and proton reduction.[121] Regarding water-oxidation, Sun *et al.* introduced the homogeneous pre-electrocatalyst $[Ni^{II}(PY5)Cl]$, where PY5 = 2,6-bis(1,1-bis(2-pyridyl)ethyl)pyridine), as illustrated in Figure 3.6 (q).[135] The catalyst shows a TON of 19 at pH 10.8 and TOF $\sim$ 145 s^{-1}. The structural analyses of the catalyst in bulk reported that the replacement of the chloride ligand with water indicated the pre-catalyst form to be $[Ni^{II}(PY5)(H_2O)]^{2+}$.[135] The hydrogen ion from

the water molecule that engages with the metal oxo [Ni^{V}=O] intermediate is conveyed to the phosphate present in the buffer solution, thereby enabling the APT necessary for O–O bond formation.[135]

3.3.6 Copper (Cu)-based Molecular Catalysts

Among the reported copper complexes, $Cu(pyalk)_2$ [Figure 3.6 (r)] is known to be an effective and robust electrocatalyst for water-oxidation in an alkaline environment.[122] It exhibits a TOF of 0.7 s^{-1} at a pH of 12.5, with the reaction rate being first-order with respect to copper.[122] The catalyst was reported to be active for more than 30 (thirty) catalytic cycles, exhibiting the lowest degradation. Upon examining a succession of alternating chemical and electrochemical processes, the catalyst operates, generating a metal oxyl radical entity. This radical entity experiences the WNA mechanism, facilitating the O–O bond formation.[122]

Further, Meyer and coworkers reported the electrocatalyst [$Cu^{II}(Py_3P)$] [Py_3P = N,N-bis(2-(2-pyridyl)ethyl)pyridine-2,6-dicarboxamidate] [Figure 3.6 (u)], that can oxidize water at pH 8. The establishment of the O-O linkage is hypothesized to be enabled by the PCET mechanism.[136]

3.3.7 Iridium (Ir)-based Molecular Catalysts

In 2008, Bernhard *et al.* reported a cyclometalated bis-aqua complex and a surrogate catalyst, $[Ir^{III}(ppy)_2(bipy)]^+$ (where, bpy = 2,2′-bipyridine, ppy = 2-phenylpyridine),

without coordinated aqua ligands.[137] The Iridium complex reached a turnover number (TON) of 2760, and the surrogate catalyst exhibited catalytic activity without producing any oxygen.[137] In 2009, Crabtree and coworkers pioneered pentamethylcyclopentadienyl (Cp^*) and 2-phenylpyrimidine (or ppy) derived precatalysts.[138]

The precursor, $[Ir^{V}(Cp^*)(O)\ (ppy)]^{+}$, was proposed as a possible intermediate. Herein, we considered the iridium catalyst developed by MacChioni and coworkers with the inclusion of the carboxylate ligand.[139] In the presence of Ce^{IV}, which acts as a sacrificial oxidant, both complexes $[Cp^*Ir(\kappa^2\text{-N,O})X]$ with X = -Cl (MWOC-23); and X = $-NO_3$ (MWOC-24) [Figure 3.6 (s)] show excellent TOFs of 287 min^{-1} and 277 min^{-1} respectively, under optimized conditions.[139]

3.4 Methodology

The geometry optimization of the $[M^{II}]^{n+}$, $[M^{V}{=}O]^{(n+1)+}$, $[M^{V}{=}O{:}H_2O]^{(n+1)+}$, and $[M^{IV}\text{-}OO]^{n+}$ (M = Mn, Fe, Co, Ni, Cu, Ru, and Ir; n = 0, 1, 2) complexes were performed at the M06-L[140] and MN15-L[141] level of theories with LANL2DZ effective core potential (ECP) for all the metal (M) atoms (M = Mn, Fe, Co, Ni, Cu, Ru, and Ir) and Br atom, and 6-31G(d) basis set was used for remaining elements[142–143] using Gaussian 16[145] package. For solvent phase calculations, we adopted the solvation model density (SMD)[146] with water as the medium of interest under the experimental conditions of temperature, pressure, and pH. As far as the density functional

theory (DFT) is concerned, the spin expectation values increase with a rise in the HF exchange component.[147] To observe the reliability of the MN15-L functional, the spin expectation values, $< S^2 >$,[148] were compared with the M06-L functional and reported in Table 8.5. The rate constants for the water-oxidation were obtained for the twenty-six representative MWOCs in both gas and solvent phases using the transition state theory (TST)[51] and further corrected with the Eckart[52,53] and Wigner tunnelling methods.[54] The zero-point corrected Gibbs free energy and the electronic energies of the optimized systems were evaluated at the same computational level of theory. The energies of the optimized geometries were corrected in both M06-L and MN15-L functional with LANL2TZ effective core potential (ECP)[149,150] for all the metal (M) atoms (M = Mn, Fe, Co, Ni, Cu, Ru, and Ir), LANL2DZ for Br, and def2-TZVP[151] basis set for remaining atoms.

3.4.1 Yamaguchi Broken Spin-Symmetry (BS) Approach

In the transition metal-catalyzed water-oxidation reaction, various reactive intermediates were generated. A single determinant can not explicitly describe the electronic structure of such species. In such cases, the Kohn-Sham density theory failed to explain such phenomena.[152] Therefore, to adopt such situations, we considered the Yamaguchi broken spin-symmetry (BS) approach[153] to calculate the energy of spin-

purified low-spin complexes using the relation

$$^{LS}E = \frac{^{BS}E^{HS} < S^2 > - ^{HS}E^{BS} < S^2 >}{^{HS} < S^2 > - ^{BS} < S^2 >} \tag{3.1}$$

In Eq. (3.1), HS represents the coupled states with high spin and correlates the spin flipping in the low spin state. The $< S^2 >$ is the spin expectation value of the appropriate determinant of the spin operator.

3.5 Results and Discussion

3.5.1 Transition State Theory and Tunnelling Corrected Rate Constants

The transition states for twenty-six catalysts have been evaluated in both M06-L and MN15-L levels of theories. The computed transition states (TSs) were characterized by one imaginary frequency. The free energies of activation (ΔG_a) calculated for the O-O bond formation as the difference in free energies of TS and the reactant. For the formation of the highest oxidation state, the redox potential for all the catalysts was calculated. Under experimental conditions, at constant potential electrolysis, the formation of the highest oxidation state species is found to be endergonic, and the corresponding energy cost is added to the total barrier. Hence, based on the total energy barrier, the rate constants (k_1) governing the O-O bond formation process was

calculated using the transition-state theory.[51]

Among the Ru-based catalysts, the carboxylate-based catalysts were mostly explored because of their unique morphology. Privalov and coworkers have nicely discussed the necessity of the three water molecules as in the case of $[Ru^{II}(pda)^{2-}(py)_2]$, where py = pyridine.[154] In water-oxidation, the reactive metal-oxo complex is the final product of a sequential PCET reaction. Within the realm of water nucleophilic attack, the inner solvation shell water of the metal-oxo complex results in the formation of metal-peroxo complex $[Ru^{III}\text{-}OOH]^0$ with a release of one proton in a concerted pathway. Thus, based on the previous experimental and theoretical reports,[154] using a water trimer $(H_2O)_3$ is essential and necessary and is considered a more realistic approach. Therefore, to model the O-O bond formation, we have considered the concerted atom-proton transfer (APT) process, as shown in Figure 3.7. The obtained

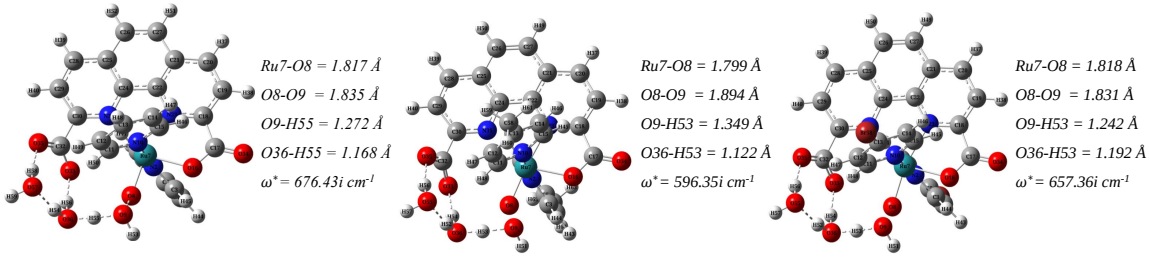

Figure 3.7: The transition state structures involved in the concerted atom-proton transfer (APT) process for the carboxylate catalysts (MWOC-1, MWOC-2, and MWOC-3). ω^* represents the imaginary frequency involved in the transition state.

TST rate constants for the rate-limiting O-O bond formation process was further corrected to evaluate $k(T)$ using the one-dimensional Eckart tunnelling method and

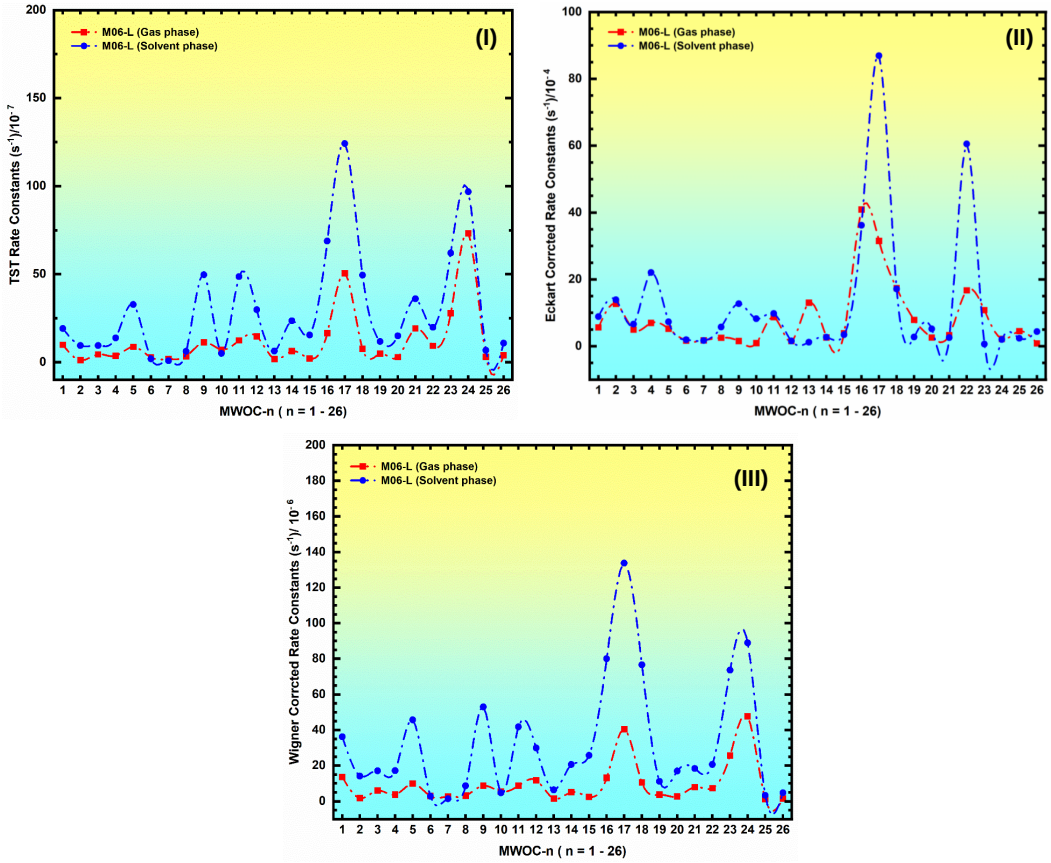

Figure 3.8: TST rate constants (s^{-1}), Wigner tunnelling corrected rate constants (s^{-1}), and Eckart tunnelling corrected rate constants (s^{-1}) for twenty-six catalysts in solvent phase using solvation model density (SMD).

the Wigner tunnelling method. Our computations indicate that MWOC-17 exhibits a comparatively higher TST rate constant within the framework of the M06-L level of theory. The obtained TST rate constants for the rate-limiting O-O bond formation process (Figure 3.8) was further corrected to evaluate $\kappa(T)$ using the one-dimensional Eckart tunnelling method and the Wigner tunnelling method. For both Eckart and Wigner methods, the rate constant of catalysts enhances that of the TST rate con-

stants, as shown in Figures 3.8 (II) and (III). For instance, with the Eckart and Wigner tunnelling correction methods, MWOC-17 shows a kinetically higher rate constant.

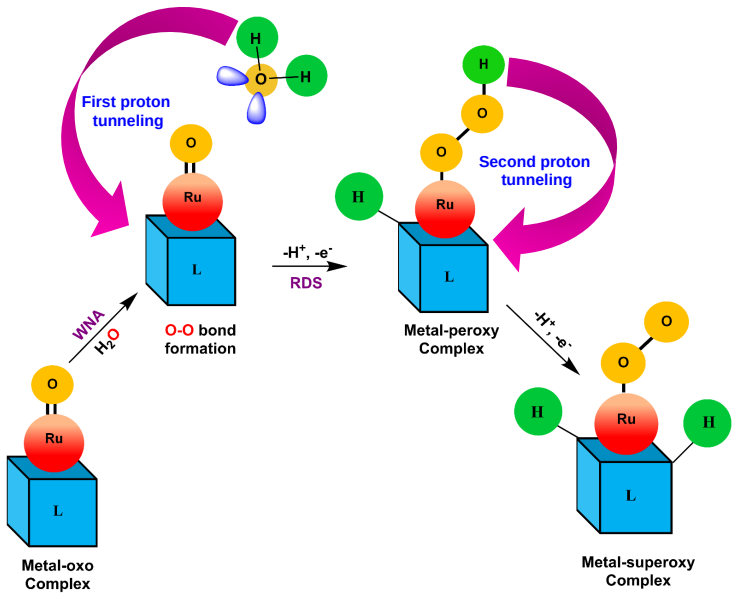

Figure 3.9: Schematic illustration of the proton transfer from water to different parts of the ligand (L) occurring in the rate-determining O-O bond formation process.

3.5.2 Feasibility of the RDS

In the RDS of the molecular water-oxidation reaction, the metal-oxo, $[M^{V}{=}O]^{(n+1)+}$ form of the catalyst reacts with the water molecule. After interaction with the water molecule, O-O bond is formed, and the generated complex undergoes sequential PCET to form metal-peroxo, $[M^{IV}\text{-}OO]^{n+}$ complex. The chemical interpretation of the RDS is

$$\mathbf{[M^{V}{=}O]^{(n+1)+} + H_2O \rightarrow [M^{IV}\text{-}OO]^{n+}}$$

The change in the Gibbs free energy of the RDS, $\Delta G_{r,RDS}$ is expressed as

$$\Delta G_{r,RDS} = G_{[M^{IV}-OO]^{n+}} - (G_{[M^{V}=O]^{(n+1)+}} + G_{H_2O}) \tag{3.2}$$

where $G_{[M^{IV}-OO]^{n+}}$, $G_{[M^{V}=O]^{(n+1)+}}$, and G_{H_2O} are free energies of the $[M^{IV}\text{-}OO]^{n+}$ complex, $[M^{V}{=}O]^{(n+1)+}$ complex, and water, respectively.

During the RDS of the water-oxidation reaction, the metal-oxo form of different molecular water-oxidation catalysts (MWOCs) will have different computed free energies, $G_{[M^{V}=O]^{(n+1)+}}$. Similarly, different metal-peroxo complexes formed as a product in the RDS will also have different values of Gibbs free energy, $G_{[M^{IV}-OO]^{n+}}$. Since $G_{[M^{V}=O]^{(n+1)+}}$ and $G_{[M^{IV}-OO]^{n+}}$ have different values for different MWOCs, according to Eq. (3.2), the $\Delta G_{r,RDS}$ will be different for different MWOCs in the RDS.

The viability of the water-oxidation process was discovered to be dependent on the energy of the lowest unoccupied molecular orbital (LUMO), E_{LUMO}, of the metal-oxo $[M^{V}{=}O]^{(n+1)+}$ species.[100] According to Pearson[155], the energy of the LUMO can be correlated to the electron affinity (EA) as E_{EA} = -E_{LUMO}, which determines the strength of the O-O bond formation. Thus, the $\Delta G_{r,RDS}$ is plotted against the $E_{EA}[M^{V}{=}O]^{(n+1)+}$ as shown in Figure 3.10 (I). On computing, our results showed that MWOC-19 has more negative $\Delta G_{r,RDS}$ = - 8.90 kcal mol^{-1} indicating the feasibility of RDS in its presence. On the other hand, in the presence of MWOC-26, the $\Delta G_{r,RDS}$

is 10.01 kcal mol^{-1}. This leads us to conclude that from the $\Delta G_{r,RDS}$ point of view, the MWOC-26 is a less preferable catalyst for water-oxidation.

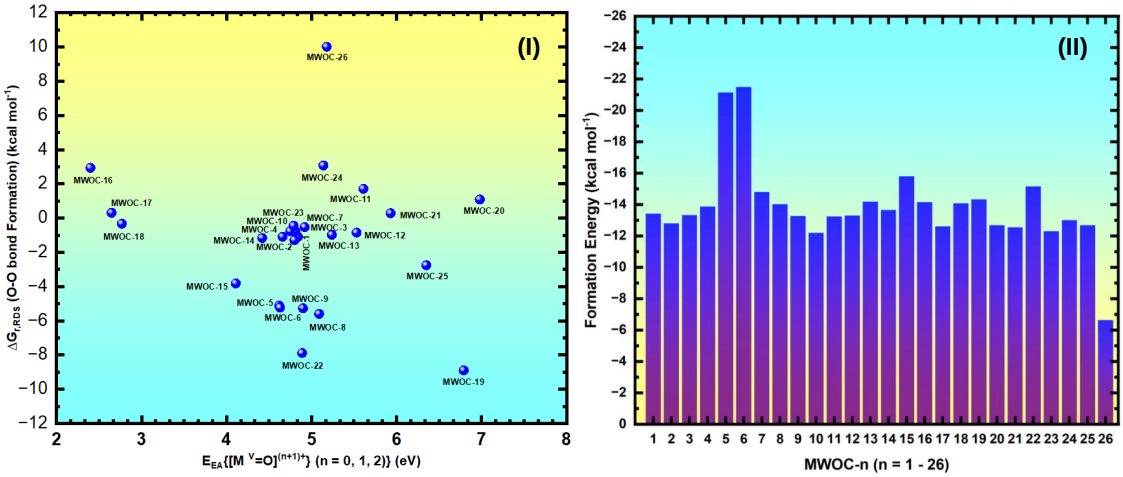

Figure 3.10: Variations in the (I) feasibility of the reaction, $\Delta G_{r,RDS}$ (O-O bond formation) in solvent phase (in kcal mol^{-1}); (II) Formation energies, E_f (in kcal mol^{-1}) involved in the rate-limiting O-O bond formation step of representative twenty-six catalysts in the M06-L level of theory using solvation model density (SMD).

To understand the effect of temperature on the feasibility of the reaction, we varied the temperature from 198 K to 298 K to 398 K for MWOC-19, as shown in Table 3.2. From our computed result, it was observed that at higher temperatures, the feasibility of the catalysis decreases because the catalyst may undergo side reactions or deactivation.

Table 3.2: The temperature dependence of the feasibility of reaction computed at the M06-L level of theory.

Catalyst	Temperature (K)	ΔG_r (kcal mol^{-1})
MWOC-19	198	— 11.18
	298	— 8.91
	398	— 7.83

3.5.3 Stability of Catalysts

In the RDS of water-oxidation reaction, energies of the $[M^{IV}\text{-}OO]^{n+}$, $[M^{V}{=}O]^{(n+1)+}$, and water was calculated for computing the formation energy, E_f of twenty-six catalysts. For the RDS, E_f is expressed as

$$E_f = E_{[M^{IV}-OO]^{n+}} - E_{[M^{V}=O]^{(n+1)+}} - E_{H_2O} \tag{3.3}$$

where $E_{[M^{IV}-OO]^{n+}}$, $E_{[M^{V}=O]^{(n+1)+}}$, and E_{H_2O} are energies of the $[M^{IV}\text{-}OO]^{n+}$ complex, $[M^{V}{=}O]^{(n+1)+}$complex, and water, respectively. Since E_f is a measure of the stability, α of the associated adduct formed in the reaction, from now onwards, we denote E_f as α.

The results from the calculations in the M06-L level of the theory suggest that during the O-O bond formation, all catalysts release energy. The extent of exothermicity of the O-O formation indicates the formation of a more stable product. In the

case of MWOC-26, during the O-O bond formation releases an energy of 6.65 kcal mol^{-1}. The release of such a small amount of energy (less exothermic) in comparison to other catalysts suggests that the O-O bond formation is relatively difficult in the case of MWOC-26 among the chosen catalysts. In contrast, for MWOC-6, the formation energy is highly exothermic (-21.49 kcal mol^{-1}), highlighting the additional stability of this catalyst, as shown in Figure 3.10 (II).

3.6 Ab-Initio Molecular Dynamics Simulation

To further confirm the findings of stability, we conducted ab-initio molecular dynamics (AIMD) simulations[156] using the CP2K software.[157] To achieve a more realistic analysis, we explicitly included the solvent environment and treated it at the quantum-mechanical level. These simulations in a solvated state were conducted within cubic boxes of varying dimensions and depended on the morphology of catalysts.

All ab-initio molecular dynamics simulations utilized the QUICKSTEP module[158] within the CP2K software. We used the GTH-PBE pseudopotential[159] and its accompanying DZVP-MOLOPT-SR-GTH basis sets[160] to characterize all atoms, along with Grimme's D3 (DFT-D3)[161] dispersion correction. The simulations were conducted under NVT ensemble conditions with a Nose–Hoover thermostat,[162] maintaining a constant temperature of 300 K for a total duration of 3 ps (3000 fs). Since from the formation energy, we observed that MWOC-6 is a more stable catalyst

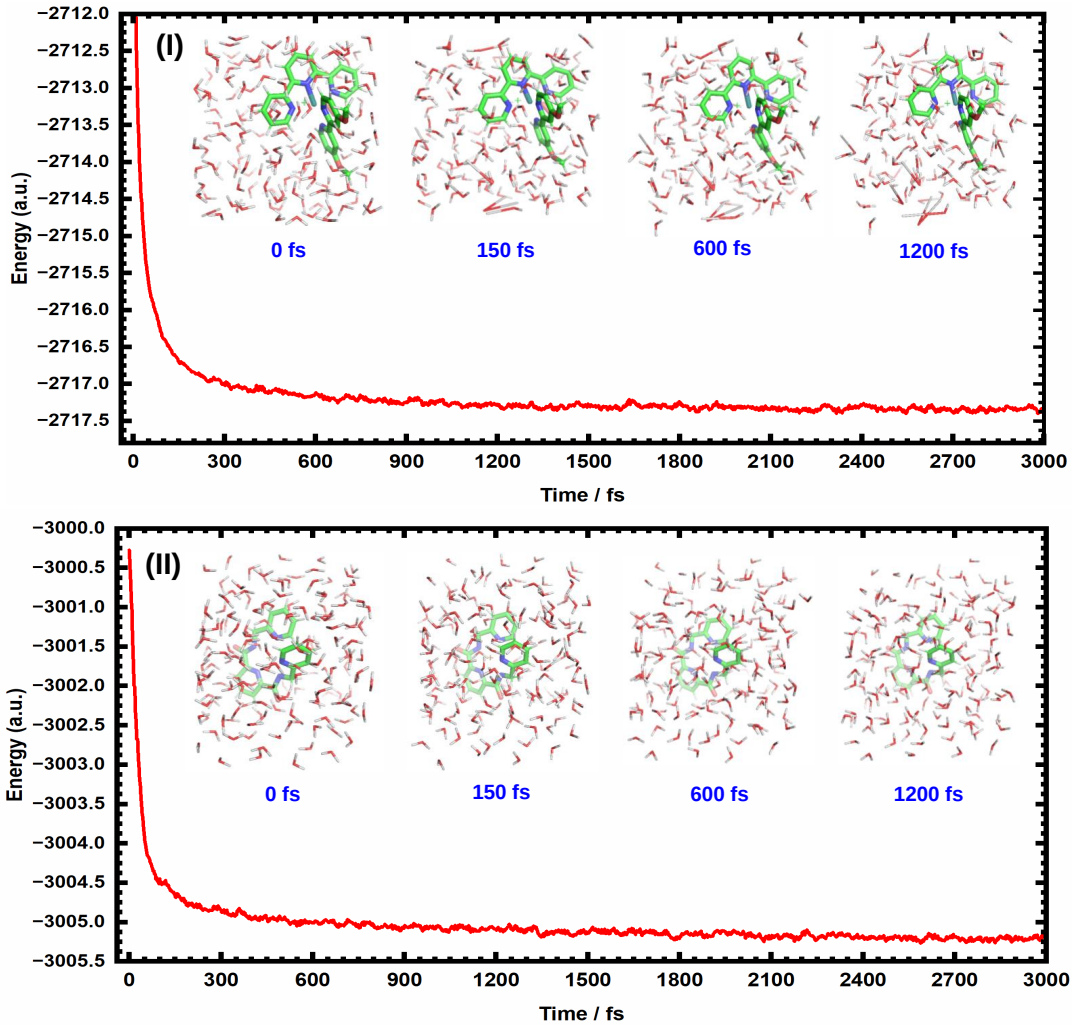

Figure 3.11: Ab-initio molecular dynamics (AIMD) simulation of (I) MWOC-6 and (II) MWOC-26. The snapshots represent different geometries at different time intervals.

and MWOC-26 is the least stable catalyst; hence, a comparative AIMD study was provided for the two catalysts in Figure 3.11.

At the beginning of the simulation, the solvated systems have a very high energy. However, with time evolution, we observe that the energy of both systems decreases rapidly, thereby enhancing their stability. For instance, in the case of MWOC-6, the solvated system achieves a stable conformation at around 1200 fs. After 1200 fs, the energy of the system remains almost constant. On the other hand, for MWOC-26, the energy of the system decreases slowly but spontaneously and remains stable after 2000 fs, suggesting the delayed stabilization of the catalyst in the solvated system. Thus, the results obtained from the AIMD show that MWOC-6 attains stability faster than MWOC-26, thereby supporting the formation energy studies.

3.6.1 Computing TONs, TOFs and Its Experimental Validation

In a water-oxidation reaction, the catalyst first reacts with the water molecule. In the multistep reaction mechanism of water oxidation, the first step often establishes a fast pre-equilibrium, forming a reactive-complex intermediate. The subsequent O-O bond formation step is established to be significantly slower and thus serves as the rate-determining step (RDS). Therefore, in the half-life expression, k_1 [Eq. (2.52)] is related to the rate constant for the first step of the water oxidation reaction.

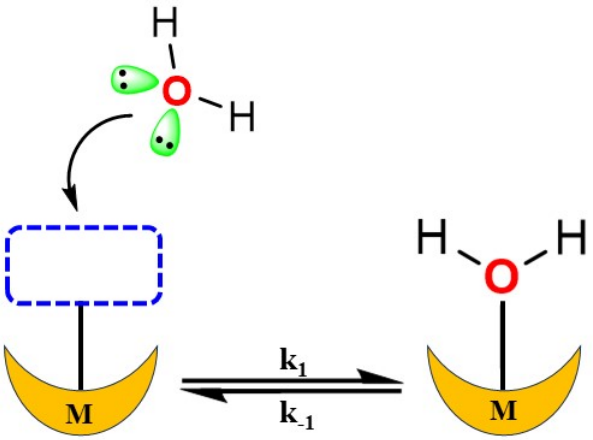

Figure 3.12: The first step of the water-oxidation reaction for calculating half-lives. In the figure, M represents the catalyst, and water is the reactant.

The pictorial representation of the first step of the water oxidation reaction used to calculate the half-lives of the catalyst is given in Figure 3.12.

For computing TONs, we have considered the experimentally defined conditions of temperature, pressure (1 atm), and pH to compute TON values as shown in Table 3.3. Under experimental conditions, to calculate turnover frequency, $\Gamma^0_{computed\ TOF}$ of the individual catalyst, we adopted the ECM and extended it to calculate turnover numbers, $\tau^0_{computed\ TON}$, and were reported in Table 3.4. To understand the extent of degradation, the activity of the catalysts was judged by calculating the catalysts' turnover frequency (TOF).

In pursuit of developing highly active and environmentally friendly catalysts, Costas and coworkers synthesized an exceptionally potent iron-based neutral tetradentate catalyst, [Fe(OTf)$_2$(Me$_2$Pytacn)] (MWOC-17).

Table 3.3: The chosen conditions for predicting experimental and theoretical TOFs and TONs of all catalysts.[7,72,80,114,115,119,120,122,129,135,139,163]

MWOCs	Temperature	pH
MWOC -1	298.15 K	1.0
MWOC -2	298.15 K	1.0
MWOC -3	298.15 K	1.0
MWOC -4	298.15 K	1.0
MWOC -5	298.15 K	1.0
MWOC -6	298.15 K	1.0
MWOC -7	298.15 K	1.0
MWOC -8	298.15 K	1.0
MWOC -9	298.15 K	1.0
MWOC -10	298.15 K	1.0
MWOC -11	298.15 K	1.0
MWOC -12	298.15 K	1.0
MWOC -13	298.15 K	1.0
MWOC -14	_d	_d
MWOC -15	298.15 K	12.2
MWOC -16	298.15 K	4.0
MWOC -17	298.15 K	1.0
MWOC -18	298.15 K	1.0
MWOC -19	298.15 K	8.0
MWOC -20	296.15 K	8.0
MWOC -21	298.15 K	8.0
MWOC -22	298.15 K	12.5
MWOC -23	298.15 K	1.0
MWOC -24	298.15 K	1.0
MWOC -25	298.15 K	8.0
MWOC -26	298.15 K	11.0

_[d] computationally designed and no experimental data is available.

At room temperature (298.15 K), MWOC-17 achieved a maximum experimental turnover frequency (TOF), $\Gamma^{0}_{experimental\ TOF}$ of 436 h^{-1}.[115] Under similar exper-

imental conditions, the efficiency conceptualization model (ECM) computations in conjunction with the M06-L level of theory predict the highest computed turnover frequency, $\Gamma^0_{computed\ TOF}$ of 841.14 $\times$ 10^{-5} s^{-1} for MWOC-17. The remarkable activity and resilience make MWOC-17 an efficient catalyst among the twenty-six water-oxidation catalysts. This highlights the remarkable activity and resilience of MWOC-17 within the catalytic cycle, positioning it as a standout performer among the twenty-six water-oxidation catalysts.

The ruthenium catalysts pioneered by the Sun group are remarkable in advancing the water-oxidation process.[7,100] They demonstrated that substituting the axial picoline (py-Me) as in MWOC-2 with pyridine (py) and Br-pyridine (Br-py) as in MWOC-1 and MWOC-3, respectively, leads to a reduction in catalytic activity. With their experiments, Sun and coworkers reported a decrease in the $\Gamma^0_{experimental\ TOF}$ from MWOC-2 (0.102 s^{-1}) to MWOC-1 (0.092 s^{-1}) to MWOC-3 (0.040 s^{-1}).[7] The trends in $\Gamma^0_{experimental\ TOF}$ were further established by ECM with the computed TOFs *i.e.*, $\Gamma^0_{computed\ TOF}$ of 118.23 $\times$ 10^{-5} s^{-1} (MWOC-2), 77.23$\times$ 10^{-5} s^{-1} (MWOC-1), and 61.85 $\times$ 10^{-5} s^{-1} (MWOC-3). Results from the experimental observations on the same catalysts reveal a corresponding decrease in turnover numbers. For instance, MWOC-1 and MWOC-2 exhibit $\tau^0_{computed\ TON}$= 272 ($\tau^0_{experimental\ TON}$ = 336) and $\tau^0_{computed\ TON}$= 256 ($\tau^0_{experimental\ TON}$ = 310), respectively, while MWOC-3 shows $\tau^0_{computed\ TON}$ = 170 ($\tau^0_{experimental\ TON}$ = 190).[7] Notably, the correspondence between

computational and experimental turnovers of catalysts strengthens the ECM strategy, thereby providing robust support to the computational results.

Additionally, systematic substitution in ruthenium-based catalysts by Thummel and coworkers unveils intriguing insights into functional group effects on turnover numbers.[129] Interestingly, we observed that the functional group influences the turnover number of the catalysts. At pH 1.0 and 298.15 K, the unsubstituted catalyst (MWOC-4) shows $\tau^0_{computed\ TON}$ of 110, and $\tau^0_{experimental\ TON}$ of 390,[129] whereas the insertion of electron-donating groups such as -Me (MWOC-5) and -OMe (MWOC-6), leads to decrease in the $\tau^0_{computed\ TON}$ to 23 ($\tau^0_{experimental\ TON}$ = 190) and 8 ($\tau^0_{experimental\ TON}$ = 110), respectively.[129] However, introducing an electron-withdrawing group such as –NO_2 (MWOC-7) leads to an enhancement of $\tau^0_{computed\ TON}$ to 55 ($\tau^0_{experimental\ TON}$ = 260) compared to the electron-donating groups.[129] This demonstrates the significant influence of functional groups on the efficiency of the catalyst.

In the case of manganese catalysts, activation for water-oxidation with R = ^{t}Bu (MWOC-15) shows a minimum experimental TON of 16 at pH = 12.2.[73] The same catalyst under a similar environment reports $\tau^0_{computed\ TON}$ = 40 and $\Gamma^0_{computed\ TOF}$ = 16.70 × 10^{-5} s^{-1}, validating it to be the second lowest efficient catalyst among the chosen set of twenty-six catalysts. Further, the Sun group has designed a Ni-PY5 (MWOC-21) catalyst that showed $\Gamma^0_{computed\ TOF}$ of 24.60 × 10^{-5} s^{-1}, while $\Gamma^0_{experimental\ TOF}$ is 145 s^{-1} under experimental conditions.[135]

Table 3.4: Computed TOFs ($\Gamma^0_{computed\ TOF}$) and computed TONs ($\tau^0_{computed\ TON}$) with ECM in M06-L levels of theories. The TOFs were reported in s^{-1}.

MWOC	$\Gamma^0_{computed\ TOF} \times 10^5$ (s^{-1})	$\tau^0_{computed\ TON}$	$\tau^0_{experimental\ TON}$
MWOC-17	841.14	2321	82
MWOC-22	295.75	212	30
MWOC-16	280.82	49	1030
MWOC-4	191.22	110	390
MWOC-18	165.31	322	145
MWOC-2	118.23	256	310
MWOC-11	82.28	102	95
MWOC-1	77.23	272	336
MWOC- 9	76.21	131	135
MWOC-10	75.12	31	_[c]
MWOC-3	61.85	157	190
MWOC-20	45.16	21	160
MWOC-8	28.51	462	570
MWOC-5	26.09	23	190
MWOC-21	24.60	69	19
MWOC-14	23.18	5	_[c]
MWOC-15	16.70	40	16
MWOC-26	15.42	534	19
MWOC-25	15.39	232	41
MWOC-7	14.94	55	260
MWOC-12	13.77	154	_[c]
MWOC-24	12.64	107	2000
MWOC-13	10.80	41	416
MWOC-6	8.08	8	110
MWOC-23	5.82	89	1200
MWOC-19	3.97	14	16

Computed TOF

[c] Experimental results not reported

Along the line, Fukuzumi and coworkers conducted a photo-irradiation experiment on the catalyst $[Co(12\text{-}TMC)]^{2+}$ (MWOC-19), where 12-TMC = 1,4,7,10-tetramethyl-1,4,7,10-tetraazacyclododecane. The experimental results reveal that MWOC-19 has the low $\tau^0_{experimental\ TON}$ of 16 among the same set of twenty-six catalysts.[120] ECM computations further confirm this result, yielding a corresponding low $\tau^0_{computed\ TON}$ of

14, providing additional validation to the experimental findings. This harmonization of computed and experimental findings reinforces ECM as a valuable tool in assessing the turnover of catalysts.

Furthermore, for the copper-based catalysts, Batista and group developed $[Cu(pyalk)_2]$[122](MWOC-22) where pyalk = 2-pyridyl-2-propanoate. With the same metal as the active center, the Meyer group has developed another copper catalyst, $[Cu(Py_3P)]$[136] (MWOC-26). Under slightly basic conditions (pH = 8.0), MWOC-26 reported $\tau^0_{computed\ TON}$ of 534. At pH = 12.5, MWOC-22 shows $\tau^0_{computed\ TON}$ of 212. The comparison of the two copper catalysts nicely established the comparative efficiencies of both catalysts, delineating MWOC-26 as the better catalyst.

In addition, to carry out water-oxidation efficiently, Bucci *et al.*[139] synthesized a variety of iridium-based catalysts by changing the functional groups to propose a catalyst with enhanced efficiency. To do so, they designed $[Cp^*Ir(\kappa^2\text{-N,O})X]$, where, κ^2-N,O = 2-pyridine carboxylate; X = -Cl (MWOC-23) and X = $-NO_3$ (MWOC-24) that showed $\tau^0_{experimental\ TON}$ of 1200 and 2000 respectively, and are found to possess the highest experimental TONs among the chosen catalysts.[139] The results of our computations also demonstrate that MWOC-23 and MWOC-24 shows the computed turnover numbers, with $\tau^0_{computed\ TON}$ of 89 and $\tau^0_{computed\ TON}$ of 107, respectively, thus affirming the validity of the experimental findings.[139] The adopted experimental conditions for our computations are provided in Table 3.3. The $\Gamma^0_{computed\ TOF}$ and

$\tau^0_{computed\ TON}$ with $\tau^0_{experimental\ TON}$ are reported in Table 3.4.

It is important to mention that a higher turnover frequency (TOF) of a catalyst does not always assure a higher turnover number (TON). To observe the validity of

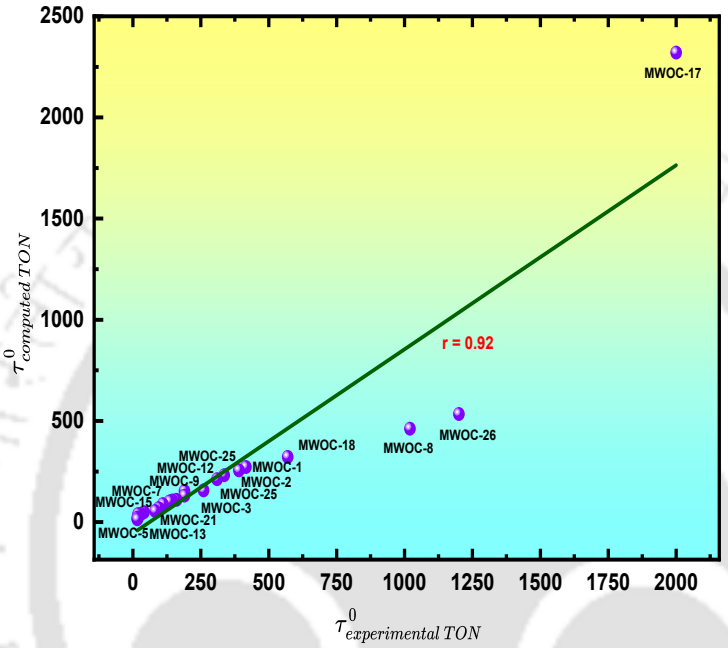

Figure 3.13: Pearson's correlation coefficient analysis between the computed TONs, $\tau^0_{computed\ TON}$, and experimental TONs, $\tau^0_{experimental\ TON}$, at the M06-L level of theory with the correlation coefficient $r = 0.92$.

computed TONs and the correlation of the computed and experimental TONs, we carried out a Pearson's correlation coefficient analysis.[164] We observed that the ECM equation upholds a correlation between the computed TONs and the experimental TONs with $r = 0.92$, as seen in Figure 3.13. Since the correlation for the developed equation shows $r \geq 0.90$ for the M06-L level of theory, the computed results reported

show a strong correlation,[164] and thus, the results are worth mentioning.

3.6.2 Factors Limiting the TON Values

Several factors limit the TON values. Practically, during catalysis, there occurs a loss of the active species, and the remaining active species will move the reaction forward. To counterbalance the effect and enhance efficiency, consideration of catalyst loading is an important factor. When the rate of catalyst deactivation is high, an increase in catalyst loading will help the reaction to achieve more TON. At the current stage, in ECM, we calculated the efficiency at a similar concentration for all catalysts. However, each catalyst may exhibit optimum efficiency at different catalyst loading. Thus, the inclusion of concentration terms may enhance the efficiency of catalysts.

In ECM, enhancing the performance of catalysts is the main focus. To study the catalyst performance, improvements in the kinetic behaviour were studied in terms of the tunnelling corrected rate constants. In addition to the performance of the catalysts, the catalyst deactivation is also an important factor that affects the TON of catalysts. Therefore, although we have considered catalyst deactivation, a more detailed consideration of the same will be necessary, and accordingly, the ECM strategy will be amended.

Further, in the current scenario, the strategy was applied using an implicit solvation process. However, implicit solvation assumes the presence of a dielectric contin-

uum around the molecular surface. Thus, to mimic the experimental condition, the consideration of an explicit solvent box is another vital factor.

Moreover, considering a higher level of theory may be more beneficial in predicting accurate TONs. The consideration of these factors will sufficiently modify ECM and will be able to provide a perfect match between the computational and experimental results in future under the same reaction conditions.

3.7 Concluding Remarks

Based on kinetic and thermodynamic perspectives, we mathematically formulated the method called efficiency conceptualization model (ECM) to compute the TOF, $\Gamma^0_{computed\ TOF}$ and TON, $\tau^0_{computed\ TON}$ of catalysts. To validate this strategy, we initially applied the strategy to the water-oxidation reaction catalyzed by the transition metal-based catalysts following the WNA pathway. For molecular water-oxidation, the O-O bond formation process is the RDS of the catalytic cycle and is the target reaction based on which we computed the efficiency of catalysts. Results from our computations suggest that MWOC-17 shows the highest TST rate constant. After the incorporation of the tunnelling correction, the Wigner and Eckart tunnelling corrected rate constants for MWOC-17 are enhanced. ECM also delineates that MWOC-19 has the more negative Gibbs free energy of the RDS, $\Delta G_{r,RDS}$, indicating the greater feasibility of the O-O bond formation reaction in its presence. In addition, for the O-O

bond formation process, MWOC-6 shows the highest formation energy value, E_f, indicating the greater stability of the associated adduct. The stability results were further confirmed by the ab-initio molecular dynamics (AIMD) simulations. For the water-oxidation reaction, the iron (Fe)-based catalyst MWOC-17 exhibited a very high computed $\Gamma^0_{computed\ TOF}$ of 841.14 $\times$ 10^{-5} s^{-1} using the M06-L level of theory under experimental conditions. This suggests that MWOC-17 takes more turns in unit time in the catalytic cycle. In contrast, the cobalt (Co) catalyst MWOC-19 showed the lowest $\Gamma^0_{computed\ TOF}$ of 3.97 $\times$ 10^{-5} s^{-1}, indicating that it completes lower turns in the catalytic cycle. To understand the lifetime of the catalysts, we calculated the half-life of the catalyst. The concept of TOF was extended to quantify the turnover numbers (TON) of catalysts under half-life conditions. For the water-oxidation reaction, the iron (Fe) catalysts MWOC-17 reported the highest computed turnover numbers, $\tau^0_{computed\ TON}$ of 2321. Further, the cobalt (Co) catalyst MWOC-19 showed the lowest computed $\tau^0_{computed\ TON}$ of 14, corroborating with the experimental turnover number $\tau^0_{experimental\ TON}$ of 16, validating the experimental findings. The experimental and computed TONs were found to be strongly correlated using Pearson correlation coefficient analysis with a Pearson's $r = 0.92$ at the M06-L level of theory. This strong correlation ($r \geq 0.90$) indicates a very strong relationship between the computed and experimental data.

4

Assessing the Activity: The *MaxKinEff* Model

4.1 Introduction

The exploration of kinetics is an important aspect in predicting the efficiency of catalysts. Various research groups have developed different models to explore the efficiency of catalysts. Among them, the energetic span model,[18], degree of rate control[23,24], molecular volcano plot,[26] and microkinetic modeling[28] have proven to be particularly beneficial. In catalytic systems with a known number of active sites, two parameters are used to define catalytic activity: the turnover number (TON) and the corresponding turnover frequency (TOF).[11]

In catalysis, the catalyst concentration varies with time, and its efficiency depends on reaction conditions. Although catalyst activation is crucial, catalyst deactivation also plays a significant role in catalysis.[14] The process of catalyst deactivation relies on the catalyst loading and the adopted reaction environments. Therefore, to comprehend the complex network of catalysis, it is necessary to develop another model considering these necessities. At this stage, the formulation of kinetic models plays an important role in predicting reaction rates under different conditions and helps to optimize the conditions for catalytic processes to enhance efficiency.

Thus, to advance the catalytic modeling for the determination of the catalytic efficiency, herein, we introduced a purely kinetic model, named the maximum kinetic efficiency (*MaxKinEff*), rooted in collision theory. We generalized the catalytic cycle within the steady-state regime to predict the reaction's equilibrium constant and provide a kinetic landscape. Kinetic studies allowed the computation of half-lives, $t_{\frac{1}{2}}$, and the maximum turnover frequency, $\Gamma^0_{max\ TOF}$ of a catalyst. *MaxKinEff* assumes catalytic reactions within a cubic box, considering the collisions at larger distances to calculate the $\Gamma^0_{max\ TOF}$ of the catalyst, where reaction conditions like temperature, pressure, concentrations, and pH are considered. The schematic illustration of *MaxKinEff* model is shown in Figure 4.1.

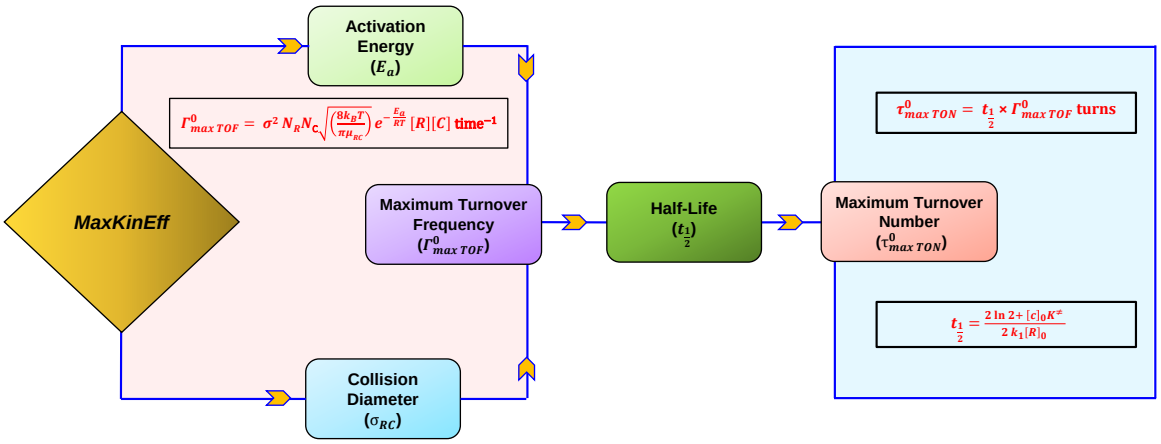

Figure 4.1: Schematic illustration of the maximum kinetic efficiency (*MaxKinEff*) model.

4.2 Kinetics of Catalytic Deactivation

The deactivation of the catalyst is not a sudden process. In the *MaxKinEff* model, the reactant, $\boldsymbol{R}$, and the catalyst, $\boldsymbol{C}$, react to form the intermediate $\boldsymbol{C}_1$. During catalysis, the amount of catalyst that remains active, $\boldsymbol{C}_1$ will carry forward the reaction as $\boldsymbol{C}_2$, $\boldsymbol{C}_3$, ... $\boldsymbol{C}_{N-1}$, and $\boldsymbol{C}_N$, until it gets consumed. Let us assume the intermediate species $\boldsymbol{C}_2$, $\boldsymbol{C}_3$ ...$\boldsymbol{C}_{N-1}$, and $\boldsymbol{C}_N$ as $\boldsymbol{RC}$, the reactant-catalyst complex. During each step of the reaction, the intermediate species undergo catalytic deactivation or side reactions and form $\boldsymbol{Q}$ as the product. Following the reaction, the catalysts eliminate the product, $\boldsymbol{P}$, and subsequently regenerate $\boldsymbol{C}$. For the catalytic cycle [Figure 4.2], the overall reaction scheme will be

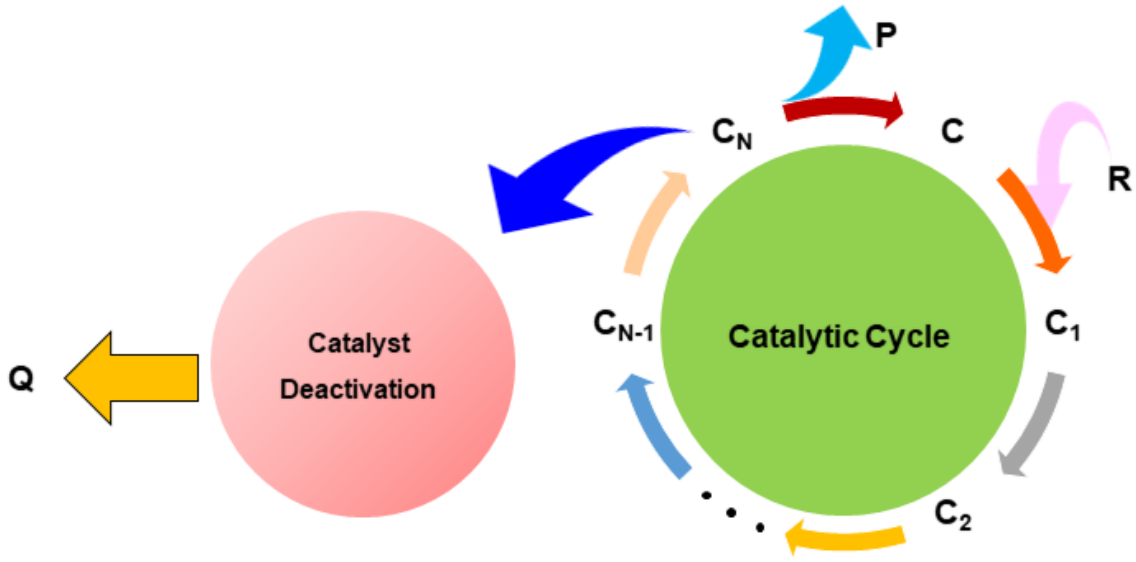

Figure 4.2: Schematic illustration of the catalytic cycle and its chemical reaction representation.

$$\mathbf{R} + \mathbf{C} \underset{k_{-N}}{\overset{k_N}{\rightleftharpoons}} [\mathbf{RC}] \xrightarrow{k_{N+1}} \mathbf{C} + \mathbf{P}$$

$$[\mathbf{RC}] \xrightarrow{k_d} \mathbf{Q}$$

In the reaction, k_N and k_{-N} are the rate constants for the forward and backward reactions, respectively. On the other hand, k_{N+1} and k_d are the rate constants for the product formation and the catalyst deactivation. Applying the steady-state approximation on $\boldsymbol{RC}$,

$$\frac{d[RC]}{dt} = 0 \tag{4.1}$$

$$\implies k_N[R][C] - k_{-N}[RC] - k_{N+1}[RC] - k_d[RC] = 0 \tag{4.2}$$

$$\implies k_N[R][C] = (k_{-N} + k_{N+1} + k_d)[RC] \tag{4.3}$$

$$\implies [RC] = \frac{k_N[R][C]}{(k_{-N} + k_{N+1} + k_d)} \tag{4.4}$$

Therefore, the rate of the product formation is

$$Rate = k_{N+1}[RC] \tag{4.5}$$

Replacing ***[RC]*** in Eq. (4.5)

$$Rate = \frac{k_{N+1}k_N[R][C]}{(k_{-N} + k_{N+1} + k_d)} \tag{4.6}$$

Due to catalyst deactivation, the efficiency of the catalyst decreases. However, catalyst deactivation is not always confined to a single pathway, making its representation very challenging.[14] When the reaction progresses and the catalyst concentration decreases, an increase in catalyst loading proves beneficial in countering the effect. The catalytic cycle will continue forming the product when the catalyst concentration is very high. However, if the rate of deactivation is high (Case-I), then complete conversion is not attainable. On the other hand, if the deactivation barrier for the catalyst is very high (Case-II), the reaction will have a slower rate of deactivation, and the reaction will proceed at low catalyst loading. Both the cases are shown below:

Case-I: If the catalysis is sluggish and deactivation becomes dominant, *i.e.*,

$k_d >> k_{-N}$, and $k_d >> k_{N+1}$, then $k_{-N} + k_{N+1} + k_d \cong k_d$. Eq. (4.6) becomes

$$Rate = \frac{k_{N+1}k_N[R][C]}{k_d} \tag{4.7}$$

Case-II: If the deactivation barrier is very high and catalysis is dominant, then k_d is very small, *i.e.*, $k_d << k_{N+1}$, and $k_{N+1} >> k_{-N}$. Therefore, in such cases, deactivation may be ignored and is more apparent at low concentrations. Thus, $k_{-N} + k_{N+1} + k_d \cong k_{N+1}$. The Eq. (4.6) becomes

$$Rate = \frac{k_{N+1}k_N[R][C]}{k_{N+1}} = k_N[R][C] \tag{4.8}$$

Therefore, in both cases, the rate of the reaction is first order to the concentration of the reactant, $\boldsymbol{R}$ and first order to the concentration of the catalyst, $\boldsymbol{C}$.

4.3 Prediction of Maximum Turnover Frequencies (TOFs)

Considering both the reactant ($\boldsymbol{R}$) and catalyst ($\boldsymbol{C}$) to be hard spheres as assumed by collision theory, collisions per unit volume (Z_{RC}) between two unlike molecules $\boldsymbol{R}$

and $\boldsymbol{C}$ with respective masses m_R and m_C, is given as[6]

$$Z_{RC} = \sigma_{RC}^2 N_R N_C \sqrt{\frac{8k_B T}{\pi \mu_{RC}}} \tag{4.9}$$

where σ_{RC} is the collision diameter between $\boldsymbol{R}$ and $\boldsymbol{C}$, N_R is the number of reactant molecules per unit volume, N_C is the number of catalysts per unit volume, k_B is Boltzmann constant, and T is the temperature. The μ_{RC} is the reduced mass of reactant $\boldsymbol{R}$ and catalyst $\boldsymbol{C}$ given by[6]

$$\mu_{RC} = \frac{m_R \times m_C}{m_R + m_C} \tag{4.10}$$

The collision of systems will be effective if they interact with a suitable orientation that surpasses a minimum threshold energy, E_a. Hence, taking into account the orientation factor, P, along with an activation barrier, E_a, the rate is given as[6]

$$Rate = P Z_{RC} exp\left(- \frac{E_a}{RT} \right) \tag{4.11}$$

Replacing Eq. (4.9) with Eq. (4.11), and diving by N_R and N_C, the rate constant, k, that has a dimension of [L^3 T^{-1}],[6] will be

$$k = P \sigma_{RC}^2 \sqrt{\frac{8k_B T}{\pi \mu_{RC}}} exp\left(- \frac{E_a}{RT} \right) \tag{4.12}$$

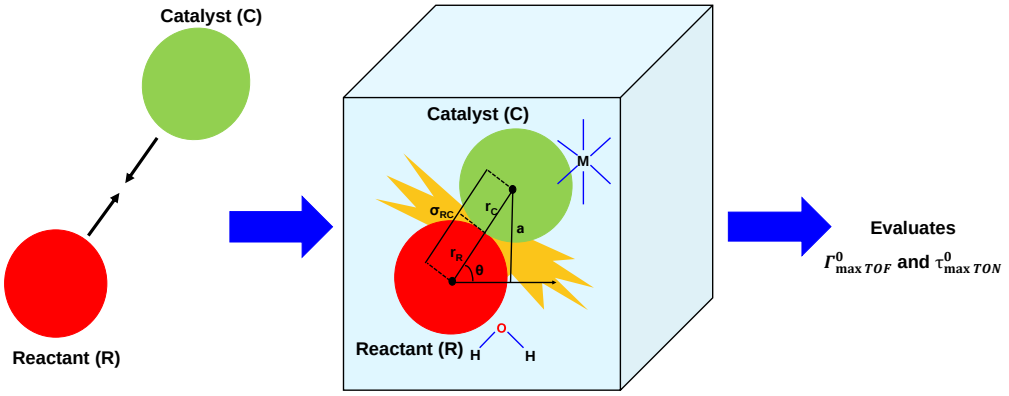

Figure 4.3: Schematic illustration for the collisions between the catalyst ($\boldsymbol{C}$) and reactant ($\boldsymbol{R}$) to evaluate $\Gamma^0_{max\ TOF}$ and $\tau^0_{max\ TON}$.

In *MaxKinEff*, the reaction occurs within a cubic box of unit volume with dimension of [L^3]. A cubic box is chosen to uniformly take care of all the possible collisions at a larger distance from the origin throughout the three-dimensional space. Since the rate constant k is dimensionally [$L^3\ T^{-1}$], therefore, the total number of potential collisions within a cubic box per unit volume will have a dimension equal to [$L^3\ T^{-1}$] $\times$ [L^{-3}] = [T^{-1}]. Thus, the rate constant k dimensionally rearranges to [T^{-1}], highlighting collisions occurring per unit time.

According to Boudart, TOF represents the rate at which reactant molecules are converted per unit time per catalytic site under defined reaction conditions.[12] Hence, Eq. (4.12) can be redefined to express the computed TOF (Γ^0) of the catalyst and is given by

$$\Gamma^0 = P\sigma_{RC}^2\sqrt{\frac{8k_BT}{\pi\mu_{RC}}}exp\left(-\frac{E_a}{RT}\right) \tag{4.13}$$

Collisions between molecules are most effective when they occur with proper orientation. Considering such cases, the theoretically possible maximum value of the orientation factor is P = 1. Under such circumstances, the turnover frequency, Γ^0 converts to the maximum TOF, $\Gamma^0_{max\ TOF}$, and is equal to

$$\Gamma^0_{max\ TOF} = \sigma^2_{RC}\sqrt{\frac{8k_BT}{\pi\mu_{RC}}}exp\left(-\frac{E_a}{RT}\right) \tag{4.14}$$

4.4 Predicting Half-lives and the Maximum Turnover Number of Catalysts

In general, the half-life of the catalyst is inversely proportional to the reactant concentration.[6] The expression of the half-life, $t_{\frac{1}{2}}$ [Eq. (4.15)], of the catalyst is given by[50]

$$t_{\frac{1}{2}} = \frac{2ln\ 2 + K^{\neq}[C]_0}{2k_1[R]_0} \tag{4.15}$$

In Eq. (4.15), $K^{\neq}=\frac{k_1}{k_{-1}}$, the equilibrium constant of the reaction with forward rate constants and backward rate constants, k_1 and k_{-1}, respectively. $[C]_0$ and $[R]_0$ are the initial concentrations of the catalyst and reactant, respectively. Further, depending on the value of $K^{\neq}[C]_0$, $t_{\frac{1}{2}}$ varies.

Case-I: When the value of $K^{\neq}[C]_0 >> 2ln\ 2$, then the numerator of Eq. (4.15)

reduces to $2ln\,2 + K^{\neq}[C]_0 = K^{\neq}[C]_0$. Therefore, Eq. (4.15) can be written as

$$t_{\frac{1}{2}} = \frac{K^{\neq}[C]_0}{2k_1[R]_0}$$

Since, $K^{\neq} = \frac{k_1}{k_{-1}}$, therefore,

$$t_{\frac{1}{2}} = \frac{[C]_0}{2k_{-1}[R]_0} \tag{4.16}$$

Case-II: When the value of $K^{\neq}[C]_0 << 2ln\,2$, then the numerator of Eq. (4.15) reduces to $2ln\,2 + K^{\neq}[C]_0 = 2ln\,2$. The Eq. (4.15) changes to

$$t_{\frac{1}{2}} = \frac{ln2}{k_1[R]_0} \tag{4.17}$$

In both cases, the half-life of the catalyst is inversely related to the rate constants [Eq. (4.16) and Eq. (4.17)]. In addition, the rate constant, k_1 will vary depending on the reaction conditions. Therefore, $t_{\frac{1}{2}}$ is a condition-dependent kinetic parameter.

Further, when $[C]_0$ is very high, the second term of the numerator of the Eq. (4.15), *i.e.*, $K^{\neq}[C]_0$ cannot be ignored. Hence, $t_{\frac{1}{2}}$ will depend on the catalyst loading. Thus, a higher concentration of the catalyst will result in a greater half-life.

If the maximum TOF is represented by $\Gamma^0_{max\ TOF}$, then, by definition, the catalyst will have $\Gamma^0_{max\ TOF}$ turns in unit time. Therefore, in $t_{\frac{1}{2}}$ time, the catalyst will have $(\mathbf{t}_{\frac{1}{2}} \times \Gamma^0_{max\ TOF})$ turns. This suggests that $(\mathbf{t}_{\frac{1}{2}} \times \Gamma^0_{max\ TOF})$ is the maximum number

of turns a catalyst can take during its half-life period. Mathematically,

$$\tau^0_{max\ TON} = (\mathbf{t}_{\frac{1}{2}} \times \Gamma^0_{max\ TOF}) \quad turns \tag{4.18}$$

$$\tau^0_{max\ TON} = \sigma^2_{RC}\sqrt{\frac{8k_BT}{\pi\mu_{RC}}}exp\left(-\frac{E_a}{RT}\right) \times \left(\frac{2ln2 + K^{\neq}[C]_0}{2k_1[R]_0}\right)\ turns \tag{4.19}$$

Therefore, by determining the value of the half-life and the maximum turnover frequency ($\Gamma^0_{max\ TOF}$) of the catalyst, the maximum turnover number ($\tau^0_{max\ TON}$) of a catalyst can be computed.

4.5 Comparison of *MaxKinEff* with the Existing Models for Predicting Efficiency of Catalysts

To predict catalytic efficiency, different models have been developed based on unique approaches. Existing models such as the energetic span model,[18] the degree of rate control,[23,24] molecular volcano plot,[26] microkinetic modeling,[28] qualitatively assess catalyst efficiency, while *MaxKinEff* quantifies turnover frequencies and turnover numbers, which are validated with experimental results. Each model is based on different assumptions to predict turnover numbers and turnover frequencies. However, a detailed comparison is necessary to understand the similarities and differences between *MaxKinEff* and the existing models.

The energetic span model[18] is one of the widely used theoretical frameworks to

describe efficiency. Under steady-state conditions, the model predicts TOF using Eyring's transition state theory (TST). The energetic span (δE) between the TOF-determining transition states (TDTS) and TOF-determining intermediates (TDI), along with the reaction's driving force, facilitates TOF prediction through Arrhenius-Eyring kinetics.[18] To identify the critical states of the reaction, the model uses the degree of TOF control, X_{TOF}. The model proposed that catalytic efficiency is determined by rate-limiting states rather than rate-determining steps.[18] On the other hand, the *MaxKinEff* explores the overall mechanism of the reaction rather than rate-limiting states. Additionally, the *MaxKinEff* assumes the collisions within a cubic box to uniformly account for collisions over larger distances thereby calculating the maximum turnover frequency in terms of rate constants.

The molecular volcano plot[26] is another important model based on Sabatier's principle.[34,35] The volcano plot employs a descriptor variable to estimate the energies of transition states an intermediate involved in the catalytic cycle through linear free energy scaling relationships (LFSR). The approach produces a volcano curve that indicates the performance of each catalyst. In the volcano curve, the most effective catalyst is situated near the plateau.[26] In contrast, the *MaxKinEff* is a purely kinetic approach. It considers the collision diameter and activation barrier of the reaction and thus help to predict efficiency without relying on the thermodynamics of catalysts.

As far as microkinetic modeling[28] is concerned, it starts with assigning reaction

rates to all elementary reaction steps. The reaction rate of each elementary step is described by a differential equation, which can be numerically solved using initial concentration conditions.[28] The microkinetic modelling establishes a connection between the rate constant and the concentration of the species and helps in predicting the turnover frequency (TOF) of catalysts.[28] On the other hand, rather than focusing on individual elementary steps, the *MaxKinEff* model considers the overall catalytic mechanism for predicting the overall reaction rate under steady-state conditions. By applying collision theory, it predicts the maximum turnover frequency based on rate constants, providing a different approach to understand catalytic efficiency.

The degree of rate control (DRC)[23,24] is an important analytical tool used in catalysis to study multistep reaction mechanisms. DRC identifies the transition states and intermediates that control the reaction rate. By modifying the catalyst, solvent, or reactant structure, the energies of the rate-controlling transition states and intermediates can be adjusted and help to improve the performance of the catalyst.[23] Similarly, the *MaxKinEff* also addresses multi-step reaction mechanisms in which it considers the inevitable catalytic degradation or side reaction occurring in the mechanism and thus provides an actual illustration of the reaction.

4.6 Effect of Changing Conditions on the "Turning Over" of Catalysts

In our *MaxKinEff* model, the equations derived for $\Gamma^0_{max\ TOF}$ [Eq. (4.14)] and $\tau^0_{max\ TON}$ [Eq. (4.19)] are under standard conditions of temperature (298.15 K), pressure (1 atm), and concentration (1 M). However, variations in temperature and concentration are the main parameters that vary the values of $\Gamma^0_{max\ TOF}$ and $\tau^0_{max\ TON}$.

4.6.1 Effect of Temperature

The temperature is the primary parameter that affects $\Gamma^0_{max\ TOF}$ and $\tau^0_{max\ TON}$ of the catalyst. On increasing the temperature, the reactants, $\boldsymbol{R}$, and catalysts, $\boldsymbol{C}$, will achieve more kinetic energy and move in a faster random motion. This will eventually lead to an increase in collisions. In other words, an increase in collisions suggests an increase in the $\Gamma^0_{max\ TOF}$ of catalyst.

As far as the $\tau^0_{max\ TON}$ is concerned, depending on whether the reaction is exothermic or endothermic, the value of $K^{\neq}$ can vary. However, at a constant T, the magnitude of $K^{\neq}$ remains constant.

On increasing the temperature from T K to (T + C) K, where C is the change in

temperature, the ratio of $\Gamma^0_{max\ TOF}$ at these two temperatures will be,

$$\frac{\Gamma^0_{max\ TOF,\ TK}}{\Gamma^0_{max\ TOF,\ (T+C)K}} = \frac{\sigma\sqrt{\left(\frac{8kT}{\pi\mu}\right)}\ exp\left(-\frac{E_{a,T}}{RT}\right)}{\sigma\sqrt{\left(\frac{8k(T+C)}{\pi\mu}\right)}\ exp\left(-\frac{E_a}{R(T+C)}\right)} \tag{4.20}$$

$$\implies \frac{\Gamma^0_{max\ TOF,\ TK}}{\Gamma^0_{max\ TOF,\ (T+C)K}} = \frac{\sqrt{T}\ exp\left(-\frac{E_{a,T}}{T}\right)}{\sqrt{(T+C)}\ exp\left(-\frac{E_{a,(T+C)}}{(T+C)}\right)} \tag{4.21}$$

$$\implies \frac{\Gamma^0_{max\ TOF,\ TK}}{\Gamma^0_{max\ TOF,\ (T+C)K}} = \sqrt{\frac{T}{(T+C)}}\left[exp\left(-\frac{E_{a,T}}{T}\right) \times exp\left(\frac{E_{a,(T+C)}}{(T+C)}\right)\right] \tag{4.22}$$

$$\implies \frac{\Gamma^0_{max\ TOF,\ TK}}{\Gamma^0_{max\ TOF,\ (T+C)K}} = \left(\sqrt{\frac{(T+C)}{T}}\right)^{-1} exp\left[\frac{E_{a,(T+C)}}{(T+C)} - \frac{E_{a,T}}{T}\right] \tag{4.23}$$

$$\implies \frac{\Gamma^0_{max\ TOF,\ TK}}{\Gamma^0_{max\ TOF,\ (T+C)K}} = \left(\sqrt{1+\frac{C}{T}}\right)^{-1} exp\left[\frac{E_{a,(T+C)}}{(T+C)} - \frac{E_{a,T}}{T}\right] \tag{4.24}$$

Further, on increasing temperature, catalyst deactivation also becomes more pronounced, as it is a temperature-dependent phenomenon. To explain the temperature dependence, van Putten *et al.*[48] have shown the catalytic transfer hydrogenation (TH) of acetophenone using the Mn-NHC complexes. For the Mn-NHC catalyst, they have reported that with the same catalyst loading (50 ppm), the rate of deactivation enhanced at 70 ^{0}C compared to 60 ^{0}C. Thus, the reaction at lower temperature becomes more efficient, leading to higher catalytic turnovers.

4.6.2 Effect of Concentration

In catalysis, concentration plays a significant role. The computed maximum turnover frequency, $\Gamma^0_{max\ TOF}$, depends on the catalyst concentration in the catalytic reaction. During catalysis, at each step, the active species, $\boldsymbol{C}_1$, $\boldsymbol{C}_2$, $\boldsymbol{C}_3$, ... $\boldsymbol{C}_{N-1}$, and $\boldsymbol{C}_N$ get consumed and undergo deactivation (Figure 4.2). After the first step, the remaining amount of unconsumed catalyst, $\boldsymbol{C}_2$, will move the reaction forward. However, as the concentration of $\boldsymbol{C}_3$, ... $\boldsymbol{C}_{N-1}$, and $\boldsymbol{C}_N$ decreases, to sustain the reaction, it is necessary to increase the catalyst concentration. On increasing the catalyst concentration (or high catalyst loading), the activity of the catalyst will increase.

Further, when the catalyst concentration is very high, the catalytic cycle will continue forming the product. In the case of the Mn-catalyzed ester reduction process, Liu *et. al*[165] and van Putten *et. al*[40] have reported that increasing the concentration of the [KO^{t}Bu] base promoter for different benzoate substrate increases the yield. They reported that methyl and ethyl benzoates are more susceptible to the base concentration compared to the tert-butyl and benzyl benzoates. This is because the small alcohols formed from the methyl and ethyl benzoates inhibit the catalyst more, resulting in the stable manganese alkoxides formation.

4.7 Concluding Remarks

To assess the activity of the catalyst, turnover frequency is an important parameter. In the current chapter, the *MaxKinEff* model reported by us is purely kinetic, based on the collision theory to predict the maximum turnover frequency, $\Gamma^0_{max\ TOF}$ of catalysts. To compute the $\Gamma^0_{max\ TOF}$, *MaxKinEff* relies on two parameters: activation barrier (E_a) and collision diameter (σ_{RC}) of the reactant-catalyst ($\boldsymbol{RC}$) complex. The *MaxKinEff* model is designed to describe reactions under steady-state conditions. Therefore, it focuses on the behavior of the reaction when the concentrations of intermediates remain constant over time, reflecting a dynamic equilibrium of reactants and products. Unlike many other efficiency prediction models, the *MaxKinEff* model estimates the overall reaction kinetics, considering the reactants' and catalysts' reaction rates. According to the *MaxKinEff* model, the catalytic reaction follows first-order kinetics to both the reactant and the catalyst individually, resulting in an overall second-order reaction rate. The model assumes a cubic box to account for collisions occurring at a larger distance during the reaction process and, therefore, helps in understanding the efficiency of catalysts. In addition, the model provides an expression, typically represented by Eq. (4.14), to calculate the maximum turnover frequency under experimental conditions of temperature, pressure, and pH. With the computed half-lives ($t_{\frac{1}{2}}$) and maximum turnover frequency ($\Gamma^0_{max\ TOF}$), the *MaxKin-*

Eff model allows for straightforward computation of the maximum turnover number, $\tau^0_{max\ TON}$. On analyzing the effect of temperature and concentration, we found that the $\Gamma^0_{max\ TOF}$ increases with increasing these parameters. Further, as far as deactivation is concerned, the catalytic cycle will continue forming the product at high concentrations. Thus, catalyst deactivation relies on catalyst loading.

The computational approach for the *MaxKinEff* is expected to be a useful tool in the field of catalysis. The *MaxKinEff* model will be implemented in other organic and inorganic reactions to obtain the maximum TOF and TON. The discussions in this context are extended to the molecular water-oxidation reaction in the next chapter.

5

Application of the *MaxKinEff* Model to Water-Oxidation Catalysts: A Perspective to Efficiency

5.1 Introduction

In a catalytic cycle, the individual reaction steps undergo catalytic conversion at a particular rate. For a reaction following the first-order kinetics, the rate may be defined as turnover frequency (TOF) under the steady-state regime. Mathematically, the TOF of the catalyst is defined as[18]

$$TOF = \frac{N}{[C] \times t} \tag{5.1}$$

where N is the number of cycles, [C] is the catalyst concentration and t is the time.

TOF is a kinetic property that indicates the efficiency of catalysts. Therefore, it is important to understand the applicability of the formulated model for predicting TOF. In this chapter, we will employ the developed *MaxKinEff* model to determine the maximum turnover frequency ($\Gamma^0_{max\ TOF}$) and maximum turnover number ($\tau^0_{max\ TON}$) of catalysts. Our focus will remain on the water-oxidation reaction, a widely studied area in catalysis. We will apply the strategy to the transition metal-catalyzed molecular water-oxidation catalysts.

Artificial water splitting presents an energetically demanding process (ΔG = 4.92 eV)[166], facilitating the loss of $4H^+$ and $4e^-$ with concomitant formation of an O-O bond.[63] In nature, the remarkable efficiency of water-oxidation occurs at the oxygen-evolving center (OEC), where the tetra-manganese cluster (Mn_4CaO_5) within photosystem II (PSII) serves as the catalytic entity.[88] Concurrently, in pursuit of mimicking the natural photosynthetic process, researchers have undertaken the *in vitro* fabrication of durable catalysts exhibiting high turnover numbers (TONs) and reduced overpotentials. Significant attention has been paid to ruthenium (Ru) active centers[83–87] due to their evident structural characteristics and diagonal relationship to the manganese (Mn) center.[60,88] Ruthenium (Ru) and iridium (Ir) elements from the second (4d) and third-row (5d) transition series are recognised for their high activity and resilience in water-oxidation.[7,61,139] Despite the cost-effective and abundantly avail-

able nature of first-row (3d) transition elements, they can facilitate water-oxidation under mild conditions. Extensive research on catalysts involving active centers from manganese (Mn) to copper (Cu)[72,73,114,122] reveals that these catalysts often require a high formal oxidation state. Consequently, the first-row of transition elements appears to be a more suitable catalytic system than Ru-based catalysts.

Molecular water-oxidation follows two mechanisms: (a) water nucleophilic attack (WNA)[100] and (b) interaction between two radicals (I2M).[167] In the WNA pathway, the second water molecule reacts with the oxygen atom of the metal-oxo ($[M^{V}=O]$) complex with a high oxidation state. In contrast, the I2M mechanism involves two $[M^{V}=O]$ unit with high electron density exhibiting radical character. These radical M=O species pair up to form an O-O bond via an M-O-O-M intermediate.[167] Since the chosen transition-metal-based MWOCs follow the WNA pathway,[7,80,114,129] this study focuses only on the water nucleophilic attack (WNA) mechanism for methodological consistency.

Figure 5.1 shows (a) thirteen ruthenium catalysts - (i) MWOC-1: $[Ru(pda)(py)_2]$; (ii) MWOC-2: $[Ru(pda)(pic)_2]$; (iii) MWOC-3: $[Ru(pda)(Br\text{-}py)_2]$; (iv) Derivatives of $[Ru(bpy)(tpy)Cl]^{+}$ with MWOC-4: R= -H ; MWOC-5: R = Methyl (-Me) ; MWOC-6: R= Methoxy (-OMe) ; MWOC-7: R= Nitro ($-NO_2$) ; and MWOC-8: R= Ethoxycarbonyl (-COOEt) ; (v) MWOC-9: $[Ru(tpy)(bpy)(pic)]^{2+}$; (vi) MWOC-10: $[Ru(bpy)_3]^{2+}$; (vii) MWOC-11: $[Ru(tpy)(pic)_3]^{2+}$; (viii) MWOC-12: $[Ru(tpy)_2]^{2+}$

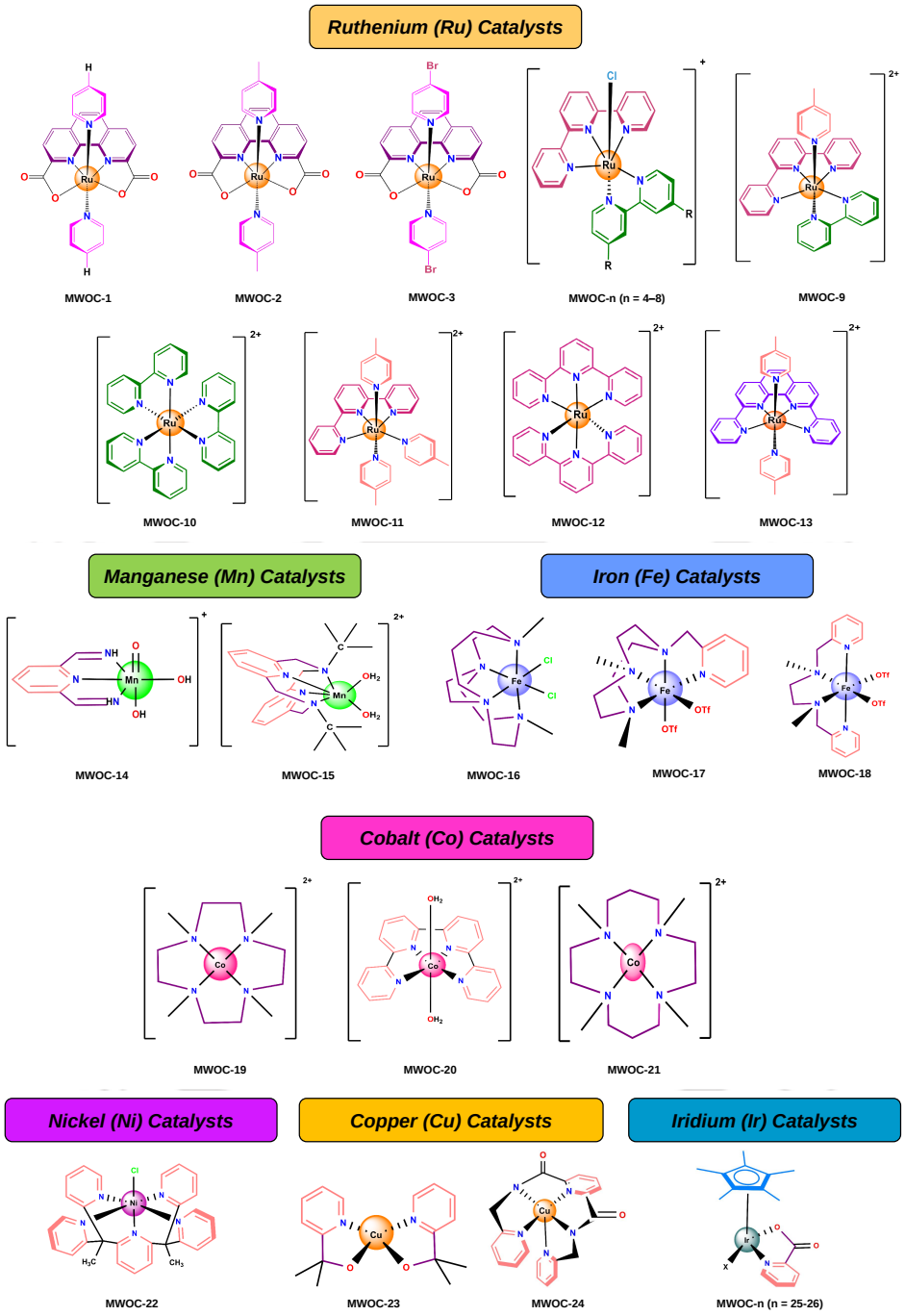

Figure 5.1: Structures of (a) Ruthenium (Ru) catalysts ; (b) Manganese (Mn) catalysts ; (c) Iron (Fe) catalysts; (d) Cobalt (Co) catalysts; (e) Nickel (Ni) catalysts; (f) Copper (Cu) catalysts; and (g) Iridium (Ir) catalysts.

; (ix) MWOC-13: $[Ru(dpp)(pic)_2]^{2+}$; (b) two Manganese catalysts - MWOC-14: $[Mn(Py)(O)(OH)_2]^{+}$; (ii) MWOC-15: $[Mn(Py)_2N^tBu_2(H_2O)_2]^{2+}$; (c) Three iron catalysts - (i) MWOC-16: cis-$[Fe(cbc)Cl_2]^{+}$; (ii) MWOC-17: $[Fe(OTf)_2(Me_2Pytacn)]$; (iii) MWOC-18: $[Fe(OTf)_2(mep)]$; (d) Three cobalt catalysts - (i) MWOC-19: [Co(12-TMC)]$^{2+}$; (ii) MWOC-20: trans-$[Co(qpy)_2(OH_2)_2]^{2+}$; (iii) MWOC-21: [Co(13-TMC)]$^{2+}$; (e) one Nickel catalyst - (i) MWOC-22: Ni-PY5 ; (f) two copper catalysts- (i) MWOC-23: $[Cu(pyalk)_2]$; (ii) (u) MWOC-24: $[Cu(Py_3P)]$; and (g) two iridium catalysts - $[Cp^*Ir(\kappa^2\text{-N,O})X]$ with MWOC-25: X = Cl; and MWOC-26: X = NO_3.

5.2 Implementation of *MaxKinEff* for Probing TOFs and TONs

During the water-oxidation reaction, the catalyst ($\boldsymbol{C}$) and the reactant water ($\boldsymbol{R}$) react together to form the catalyst-water ($\boldsymbol{RC}$) complex. Since the mass of the catalyst (m_C) is much higher than the mass of the reactant water (m_R), i.e., $m_C >> m_R$. Therefore, the reduced mass of the $\boldsymbol{RC}$-complex, μ_{RC}, becomes approximately equal to the mass of the water, m_R. Thus from Eq. (4.10)

$$\mu_{RC} \cong \frac{m_R \times m_C}{m_C} = m_R \tag{5.2}$$

Thus, Eq. (4.14) changes to the

$$\Gamma^{0}_{max\ TOF} = \sigma^{2}_{RC}\sqrt{\frac{8k_BT}{\pi m_R}}exp\left(-\frac{E_a}{RT}\right) \tag{5.3}$$

In Eq. (5.3), to evaluate the $\Gamma^{0}_{max\ TOF}$, the collision diameter (σ_{RC}) between the reactant water molecule ($\boldsymbol{R}$) and catalyst ($\boldsymbol{C}$) and the activation energy (E_a) of the reaction are the two required parameters. These two parameters, σ_{RC} and E_a, are computed and shown in Figures 5.2(a) and (b), respectively.

5.3 Methodology

Figure 5.1 shows the geometry of twenty-six catalysts chosen under investigation. The optimization of the complexes, $[M^{II}]^{n+}$, $[M^{V}{=}O]^{(n+1)}$, $[M^{IV}\text{-}OO]^{n+}$ (where M represents Mn, Fe, Co, Ni, Cu, Ru, or Ir, and n equals 0, 1, or 2), and the corresponding WNA transition-states (TSs) was performed at the M06-L[140] and MN15-L[141] level of theories with LANL2DZ (Los Alamos National Laboratory 2 double ζ) effective core potential (ECP) for all the metal (M) atoms and Br atom and 6-31G(d) basis set for remaining elements [142–144] using Gaussian 16 package.[145] The zero-point corrected Gibbs free energy and the electronic energies of the optimized MWOCs were determined using the same computational accuracy and were reported in Tables 8.6 - 8.8. To determine the energy of the optimized states, we applied the Yamaguchi broken spin-symmetry (BS) approach[153] to compute the energy of spin-purified low-spin

complexes. The solvation model density (SMD)[146] was utilized to compute solvent-phase properties, considering water as solvent under the experimental conditions of temperature, pressure, and pH.

5.4 Results and Discussion

5.4.1 Calculation of the Activation Energy, E_a

According to *MaxKinEff* [Eq. (5.3)], elevated activation energy results in sluggish reaction kinetics due to reduced collisions between catalysts and water molecules. Analysis of the data reveals that among the catalysts, MWOC-3 exhibits the lowest energy barrier of 71.37 kcal mol^{-1}, as illustrated in Figure 5.2 (a). For the catalysts with similar carboxylate morphology, MWOC-2 demonstrates the highest energy barrier of 233.64 kcal mol^{-1}, while MWOC-1 reports an approximate value of 200 kcal mol^{-1}. Thus, *MaxKinEff*, suggests that an increase in the activation energy leads to a decrease in the term $\exp(\frac{-E_a}{RT})$ which subsequently decreases $\Gamma^0_{max\ TOF}$ [Eq. (5.3)]. The findings also indicate that MWOC-3 shows greater reaction turnovers per unit of time, whereas MWOC-2 exhibits fewer turnovers. However, we have rationalized the computed barriers with known TOFs and adopted the Arrhenius equation. The results suggest that the computed activation energy of catalysts differs by $\sim$ 1 kcal mol^{-1} to that of the experimental activation energy. Similarly, *MaxKinEff* highlights that among the chosen catalysts, MWOC-11 has the highest activation energy, re-

sulting in a decreased $\exp(\frac{-E_a}{RT})$ term and subsequently reduced turnover frequencies for the catalyst.

Moreover, the iron catalysts synthesized by Fillol *et al.*[115] demonstrate comparable activation energies, E_a. For instance, MWOC-18 exhibits an energy barrier of 8.28 kcal mol^{-1} higher than MWOC-17, while MWOC-16 shows an activation energy of 116.87 kcal mol^{-1}. Thus, substituting the electron-withdrawing tosylate groups with chloride groups could enhance the TOFs of the catalysts. Additionally, catalysts featuring copper active centers, such as MWOC-23 and MWOC-24, display a notable energy difference (58.30 kcal mol^{-1}). From our study, it is anticipated that the higher rigidity of MWOC-24 leads to a lower energy barrier.

5.4.2 Measuring the Collision Diameter, σ_{RC}

As the collided molecules are assumed to be hard spheres, the corresponding collision diameter of the catalyst-water complex (***RC***-complex), σ_{RC}, was calculated mathematically as the distance between the centers of the water molecule, r_R, and the catalyst, r_C. The r_R is constant for different ***RC***-complexes, so σ_{RC} varies solely with r_C. Thus, the bulkiness of the catalyst is characterized by the covalent radius of the catalyst (r_C), impacting the collision diameter, σ_{RC}. With the variety of functional groups, Thummel and coworkers developed several ruthenium-centered catalysts (MWOC-4 to MWOC-8).[129] The results reveal that MWOC-8, featuring

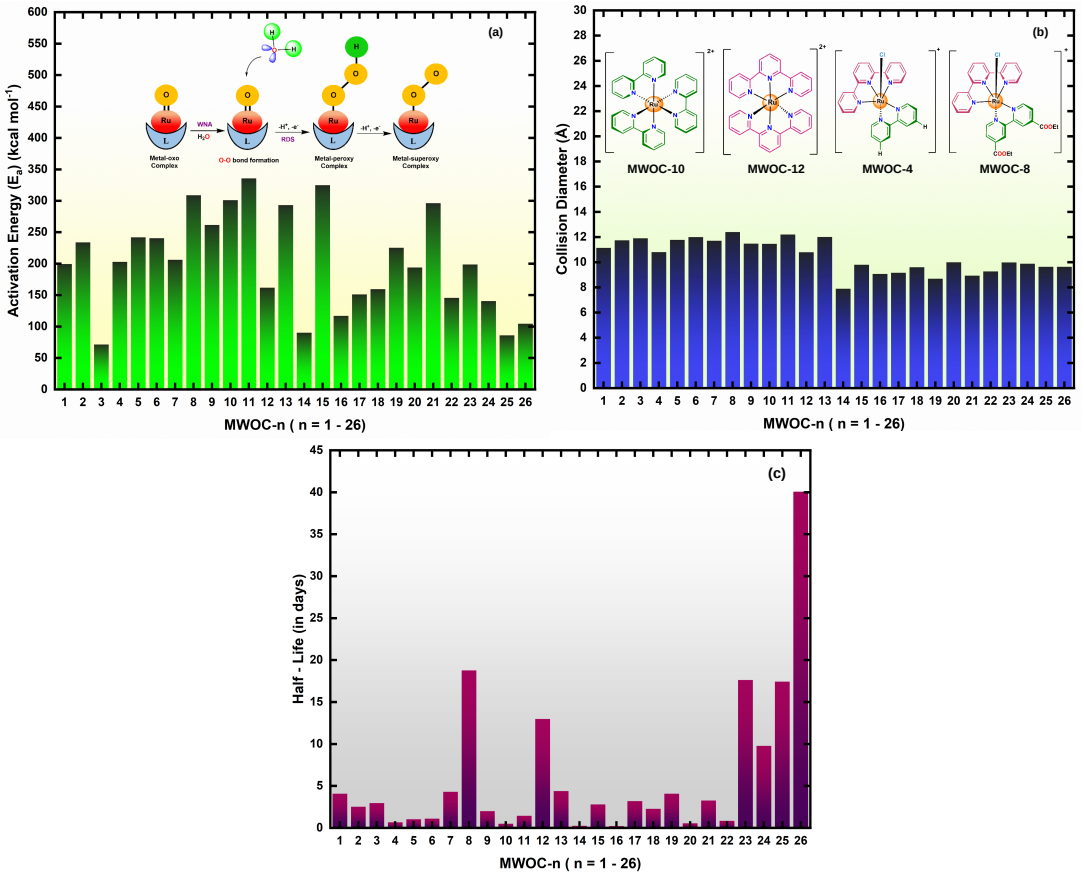

Figure 5.2: The computed (a) activation energy barrier; (b) collision diameter; and (c)Half-life of twenty-six catalysts. In (a), the picture at the top schematically illustrates the WNA mechanism. All parameters of the twenty-six catalysts computed at the M06-L level of theory employed with LANL2DZ effective core potential (ECP) for all the metal (M) atoms (M = Mn, Fe, Co, Ni, Cu, Ru, and Ir) and Br atom, and 6-31G (d) basis set for all other elements.

the -COOEt group, exhibits greater bulkiness and a larger σ_{RC}. Conversely, substituting the -COOEt group with -H in MWOC-4 reduces the bulkiness of the catalyst (r_C) and hence decreases the σ_{RC} as seen in Figure 5.2 (b).

Although there is a structural similarity between MWOC-10 and MWOC-12, both

catalysts differ mainly in ligand denticity. Notably, the σ_{RC} of MWOC-12 is significantly smaller than MWOC-10, indicating greater molecular compression by tridentate ligands than bidentate ligands. The smaller size of catalyst MWOC-14 results in a reduced σ_{RC} and contributes less to the $\Gamma^{0}_{max\ TOF}$. The average collision diameter of the 4d-ruthenium catalysts was observed to be higher than that of the remaining water-oxidation catalysts chosen for investigation.

5.4.3 Lifetime of Catalyst, $t_{\frac{1}{2}}$

Understanding how robust a catalyst remains throughout the catalytic cycle is crucial. Therefore, the half-life of catalysts serves as a suitable alternative for comprehending their standard lifetime and thus acts as a measure of the robustness of the catalyst. A robust catalyst completes more cycles in a given time, enhancing its efficiency. The results of the half-life calculations reveal that the iridium (Ir) catalysts have a very high lifespan of approximately 40.06 days (MWOC-26) and 17.42 days (MWOC-25), respectively, as depicted in Figure 5.2 (c). This highlights the importance of functional groups in predicting the half-lives of catalysts. However, in the case of iron (Fe) active centres, MWOC-16, proposed by Tan *et al.*, demonstrates a very short lifetime of 0.20 days ($\sim$ 5 hours). For instance, all the iron catalysts unexpectedly demonstrate a short lifetime. In addition, out of the different chosen cobalt catalysts, MWOC-19 and MWOC-20 exhibit lifespans of 4.07 days and 0.20 days ($\sim$ 5 hours), respectively. On

the other hand, MWOC-21 delineates a half-life of 3.26 days. These results indicate that MWOC-20 has a higher tendency towards degradation throughout the catalytic cycle. Moreover, catalysts featuring copper (Cu) as active centres do not demonstrate prolonged lifetimes. In particular, MWOC-23 and MWOC-24 were found to have a very moderate half-life of 17.61 days and 9.76 days, respectively. Thus, our results indicate that catalysts with these active centres, in conjunction with different ligand environments, exhibit variations in catalytic activity over time in promoting chemical reactions.

5.5 Assessing *MaxKinEff* with the Experiment

By considering activation energy (E_a), collision diameter (σ_{RC}), and catalyst half-life ($t_{\frac{1}{2}}$), *MaxKinEff* estimates the turnover frequencies (TOFs) and turnover numbers (TONs) of catalysts under experimental conditions of temperature, pressure, and pH [Table 3.3, *vide supra*]. The obtained TONs were normalized by calculating the ratio of the highest value of experimental TON, $\tau^0_{experimental\ TON}$ to the highest value of maximum computed TON, $\tau^0_{max\ TON}$, among the twenty-six catalysts. For instance, the computed and experimental results showed that the iridium (Ir) catalyst, MWOC-26, exhibited the highest $\tau^0_{experimental\ TON}$ and the highest $\tau^0_{max\ TON}$ among the chosen catalysts.[139] Thus, for MWOC-26, the computed normalization factor is, $NF = \frac{\tau^0_{experimental\ TON}}{\tau^0_{max\ TON}} = \frac{2000}{24499} = 0.0816$. Accordingly, the TONs for all catalysts

were multiplied by the normalization factor (NF) to obtain the normalized $\tau^0_{max\ TON}$ reported in Table 5.1.

In exploring ruthenium-based carboxylate catalysts, Sun and coworkers conducted experiments revealing intriguing insights.[7] They found that altering the axial position from pyridine (MWOC-1) to picoline (MWOC-2) led to increase in the $\Gamma^0_{experimental\ TOF}$ from 0.092 s^{-1} to 0.102 s^{-1}.[7] The trend in the experimental $\Gamma^0_{max\ TOF}$ values were further reproduced by computational analysis, yielding predicted $\Gamma^0_{max\ TOF}$ values of 739.95 $\times$ 10^{-5} s^{-1} (MWOC-1) and 753.45 $\times$ 10^{-5} s^{-1} (MWOC-2), at pH = 1.0 and T = 298.15 K. In a similar way, the $\Gamma^0_{max\ TOF}$ of the reaction increases to 1176.87 $\times$ 10^{-5} s^{-1}, indicating its prolonged endurance in the catalytic cycle. Additionally, under the strong acidic conditions (pH =1.0), MWOC-1 exhibited a $\tau^0_{max\ TON}$ of 212 ($\tau^0_{experimental\ TON}$ = 336), while MWOC-2 and MWOC-3 showed $\tau^0_{max\ TON}$ of 133 ($\tau^0_{experimental\ TON}$ = 310) and 244 ($\tau^0_{experimental\ TON}$ = 190), respectively.[7] These results collectively highlight the accuracy of the modelled method, providing robust validation for the experimental outcomes.[7] However, for MWOC-4 to MWOC-8,

Table 5.1: Computed maximum TOFs, $\Gamma^0_{max\ TOF}$ (in s^{-1}) and normalized maximum TONs, $\tau^0_{max\ TON}$ from the *MaxKinEff* in conjunction with M06-L level of theory.

MWOC	$\Gamma^0_{max\ TOF} \times 10^5$ (s^{-1})
MWOC-3	1176.87
MWOC-13	920.04
MWOC-7	803.26
MWOC-6	772.16
MWOC-12	766.01
MWOC-2	753.45
MWOC-25	742.47
MWOC-5	741.29
MWOC-1	739.95
MWOC- 26	707.75
MWOC-4	691.47
MWOC-8	690.96
MWOC-24	678.25
MWOC-9	669.83
MWOC-11	624.48
MWOC-18	610.74
MWOC-16	607.07
MWOC-20	604.99
MWOC-10	603.16
MWOC-23	595.23
MWOC-22	589.03
MWOC-17	568.06
MWOC-14	492.92
MWOC-19	421.68
MWOC-15	414.24
MWOC-21	371.09

Computed TOFs

_[c] Experimental result not reported

MWOC	$\tau^0_{max\ TON}$	$\tau^0_{experimental\ TON}$
MWOC-26	2000	2000
MWOC-8	914	570
MWOC-25	913	1200
MWOC-23	739	30
MWOC-12	701	–[c]
MWOC-24	467	19
MWOC-3	244	190
MWOC-13	243	416
MWOC-7	243	260
MWOC-1	212	336
MWOC- 2	133	310
MWOC-9	131	135
MWOC-17	128	82
MWOC-19	121	16
MWOC-18	97	145
MWOC-21	85	41
MWOC-15	81	16
MWOC-11	63	95
MWOC-6	59	110
MWOC-5	53	190
MWOC-22	34	19
MWOC-4	32	390
MWOC-20	22	160
MWOC-10	20	–[c]
MWOC-14	8	–[c]
MWOC-16	9	1020

Computed TONs

on evaluating the $\tau^0_{max\ TON}$, we found an excellent agreement with the experimental TONs, $\tau^0_{max\ TON}$. For instance, at an experimental pH of 1.0 and temperature of 298.15 K, the $\tau^0_{max\ TON}$ ranges from 59 ($\tau^0_{experimental\ TON} = 110$) for MWOC-6 to 914

($\tau^0_{experimental\ TON}$ = 570) for MWOC-8.[129]

Fillol and coworkers synthesized several exceptionally potent iron (Fe)-based neutral tetradentate catalysts, [Fe(OTf)$_2$(Me$_2$Pytacn)] (MWOC-17) and [Fe(OTf)$_2$(mep)] (MWOC-18) [where, OTf = $CF_3SO_3^-$ and Me$_2$Pytacn = 1-(2´-pyridylmethyl)-4,7-dimethyl-1,4,7-triazacyclononane; and mep = N, N´-dimethyl- N, N´-bis-(2-pyridylmethyl)-ethane-1,2-diamine].[115] At pH 8.0, these two catalysts showed outstanding TOFs of 436 h^{-1} and 503 h^{-1}, respectively.[115] The analysis of the results suggests that MWOC-17 has higher half-life suggesting it as an efficient catalyst for water-oxidation. Following the strategy, the $\tau^0_{max\ TON}$ values predict that MWOC-17 has higher TON ($\tau^0_{max\ TON}$ = 128) than MWOC-18 ($\tau^0_{max\ TON}$ = 97), aligning the results with the experiment.[115]

Meyer and coworkers synthesized a single-site copper (II) center catalyst in the water-oxidation reaction.[136] At pH = 8.0, the catalyst [Cu(Py$_3$P)] (MWOC-24), where, Py$_3$P = N,N -bis(2-(2-pyridyl)ethyl)pyridine-2,6-dicarboxamidate, showed $\tau^0_{experimental\ TON}$ of 19.[136] With the same metal as an active center, Batista, Crabtree, and Brudvig and their groups have designed [Cu(pyalk)$_2$] (MWOC-23, pyalk = 2-pyridyl-2-propanoate) which shows the turnover frequency of 0.7 s^{-1} at pH = 12.5 and $\sim$ 30 turnovers.[122] On exploring the catalyst computationally, MWOC-23 exhibit a catalytic turnover of 739, whereas, MWOC-24 completes 467 turns under experimental pH, suggesting [Cu(pyalk)$_2$] to be a less efficient catalyst than [Cu(Py$_3$P)].

Further, among the cobalt (Co) catalysts, *MaxKinEff* suggests that MWOC-19 shows a lower catalytic activity, $\Gamma^0_{max\ TOF} = 421.68 \times 10^{-5}$ s^{-1}. On the other hand, MWOC-21 reported $\Gamma^0_{max\ TOF} = 371.09 \times 10^{-5}$ s^{-1}. Although MWOC-21 and MWOC-19 show comparable σ_{RC}s, the former has an energy barrier ∼71 kcal mol^{-1} higher than the latter. Combining these factors results in a sluggish reaction with reduced collision probability with the reactant molecule, consequently diminishing the $\Gamma^0_{max\ TOF}$ value of the catalyst.

In the quest for efficient water-oxidation, Macchioni and group[139] synthesized a diverse array of iridium (Ir)-based catalysts, altering functional groups to develop catalysts with improved effectiveness. Their strategy involved designing [$Cp^*Ir(\kappa^2$-N,O)X] compounds, where κ^2-N,O represents 2-pyridinecarboxylate, and X denotes -Cl (MWOC-25) or -NO_3 (MWOC-26), both known for their ability to catalyze water-oxidation.[139] Among non-ruthenium MWOCs, the iridium-based MWOC-25, have the lowest activation energy of ∼85 kcal mol^{-1}. For MWOC-26, computationally, we expect that the electron-withdrawing capacity of the -NO_3 raises the energy barrier resulting in a sluggish rate of the reaction. In addition, *MaxKinEff*, further confirms the outstanding performance of MWOC-25 ($\tau^0_{max\ TON} = 913$; $\tau^0_{experimental\ TON} = 1200$) and MWOC-26 ($\tau^0_{max\ TON} = 2000$; $\tau^0_{experimental\ TON} = 2000$), respectively.[139] Thus, although the catalysts have lower turns per second, their longer half-life over the catalytic cycle makes them an efficient catalyst with a higher turnover number. The

agreement between experimental and computational findings validates the approach and emphasises the potential of *MaxKinEff* for computing the turnover number and turnover frequency.

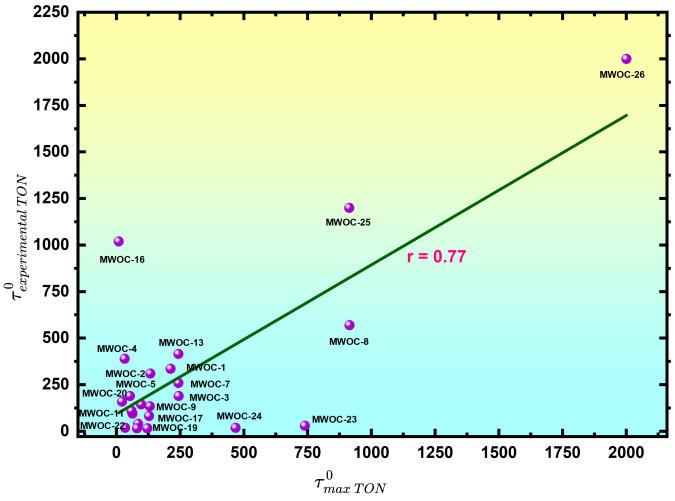

Figure 5.3: Pearson's correlation coefficient analysis between maximum computed TONs, $\tau^0_{max\ TON}$ and experimental TONs, $\tau^0_{experimental\ TON}$ with the correlation coefficient $r = 0.77$.

To observe the correlation between the computed and experimental TONs, the Pearson correlation coefficient analysis[164] was adopted with $r = 0.77$, as shown in Figure 5.3. These suggest a robust correlation between $\tau^0_{experimental\ TON}$ and $\tau^0_{max\ TON}$ values.

5.6 Concluding Remarks

In the current chapter, *MaxKinEff* calculates the maximum turnovers, $\Gamma^0_{max\ TON}$ and $\tau^0_{max\ TON}$ of twenty-six molecular water-oxidation catalysts. The application of *MaxKinEff* to MWOCs suggests that MWOC-3 has the highest turnover frequency, $\Gamma^0_{max\ TON} = 1176.87 \times 10^{-5}\ s^{-1}$, due to its bulky nature, *i.e.* larger collision diameter (σ_{RC}) and lower activation energy (E_a). In case MWOC-8, due to the presence of bulky -COOEt functional group, the catalyst has a larger collision diameter (σ_{RC}) and thereby an increased efficiency. The computed normalized $\tau^0_{max\ TON}$ values suggest that Iridium (Ir)-centered MWOC-25 has a $\tau^0_{max\ TON}$ of 913, while its $\tau^0_{experimental\ TON}$ is 1200. Similarly, for MWOC-26, the computed $\tau^0_{max\ TON}$ is 2000, which corroborates $\tau^0_{experimental\ TON}$ (2000). The iridium complexes exhibit high $\tau^0_{max\ TON}$ values due to the high lifetime in the catalytic cycle. For the water-oxidation reaction, the calculated Pearson's correlation coefficient of 0.77, for $\tau^0_{max\ TON}$ *vs.* $\tau^0_{experimental\ TON}$ values, delineates a strong correlation between the variables. Thus, the computational approach within *MaxKinEff* offers a clear mathematical framework for understanding the lifetime of catalysts, turnover frequencies (TOFs), and turnover numbers (TONs). At the current stage, *MaxKinEff* has been adopted with the experimental conditions of temperature, pressure and pH. The versatility of the method may be further examined by adopting different reactions and conditions.

6

A Comparative Analysis of Developed Models: Efficiency Conceptualization Model *vs.* *MaxKinEff* Model

6.1 Introduction

Catalysis plays a crucial role in chemical technology. Predicting the efficiencies of different catalysts used for various industrial processes is also an important facet of catalysis. Multiple models have been developed to determine the efficiencies of such catalysts, usually in terms of turnover number (TON) and turnover frequency (TOF). Although the overall complexity of the catalysis is a challenge in evaluating

the efficiencies, in the current thesis, two catalytic models were formulated *viz.* efficiency conceptualization model (ECM) and maximum kinetic efficiency (*MaxKinEff*) model. The two formulated strategies have been modelled on different foundations and were evaluated in the context of molecular water-oxidation reaction with twenty-six catalysts having different active centres. To gather more information regarding the accuracy of the models, both have been validated for the water-oxidation reaction. In the following section, we have added a comparative discussion between the models to understand their similarities and differences.

6.2 A Comparative Discussion between ECM and *MaxKinEff*

Kinetics and thermodynamics are two important factors for every chemical reaction. ECM considers that kinetics and thermodynamics play a crucial role in predicting turnover frequency (TOF) of catalysts. In dealing with kinetic factors, we have calculated the rate constants involved in the RDS. To exemplify, we consider the water-oxidation reaction catalyzed by twenty-six different catalysts and calculated the rate constants using the transition state theory (TST).[51] The obtained rate constants were further corrected by utilizing Eckart[52–53] and Wigner tunnelling methods.[54] However, the Wigner tunnelling method is not suitable for predicting TOFs and TONs as it does not take care of the barrier height of the RDS. In addition, to take

care of the thermodynamic effects, we have considered the feasibility of the reaction, $\Delta G_{r,RDS}$ and the stability (α) of the associated adduct measured in terms of formation energy (E_f) of catalysts. According to the Bell–Evans–Polanyi (BEP) principle, the activation energy varies linearly with changes in enthalpy of the elementary reaction.[58] An exothermic reaction indicates the increased stability of the associated adduct. Therefore, when the energy of the associated adduct decreases, according to the BEP principle, the activation energy also decreases. As a result, over the same time, the catalyst with lower activation energy will complete more turns and thereby will exhibit higher TOF. Thus, the increased stability of the associated adduct increases the TOF of the catalyst. However, according to ECM, increasing the TOF of the catalyst requires decreasing the value of efficiency conceptualized energy (E_{ECE}). Therefore, when a more stable associated adduct is formed, the value of E_{ECE} decreases. Thus, E_{ECE} varies linearly to $\frac{1}{\alpha}$ [Eq. (2.21)]. Further, when the Gibbs free energy of the reaction ($\Delta G_{r,RDS}$) is more negative, the feasibility of the reaction increases. Hence, over the same time, on decreasing the $\Delta G_{r,RDS}$ of the reaction, the TOF of the catalyst increases.

On the other hand, in *MaxKinEff*, we have focused only on the kinetic parameters. *MaxKinEff* considered the collision between the reactant and substrate with sufficient threshold energy and proper orientation. To determine the efficiency of catalysts, the model employs a cubic box of unit dimensions to consider the total collisions at larger

distances occurring in the three-dimensional space. Since the rate constant, k has the dimension of $[L^3\ T^{-1}]$, the total number of favourable collisions within a cubic box per unit volume will have a dimension equal to $[L^3\ T^{-1}] \times [L^3] = [T^{-1}]$. Thus, the dimension of k within the cubic box becomes $[T^{-1}]$, highlighting the number of collisions occurring per unit time as defined by Boudart.[12]

The catalyst deactivation is an important factor that is to be taken care of. While the kinetic perspective of ECM primarily focuses on the performance of the catalyst, *MaxKinEff* considers the side reaction or inevitable catalyst degradation for the catalytic cycle.

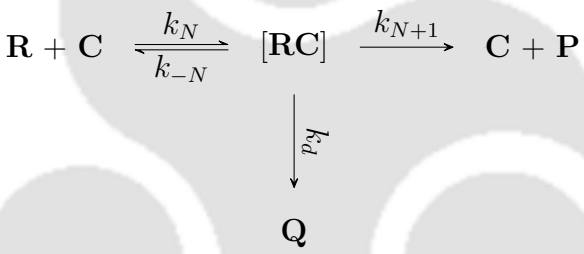

In the reaction, k_N, and k_{-N} are the rate constants for the forward reaction and backward reaction for the reaction between reactant ($\boldsymbol{R}$) and catalyst ($\boldsymbol{C}$) to form reactant-catalyst complex ($\boldsymbol{RC}$), respectively. Meanwhile, k_{N+1}, and k_d represent the rate constants for product formation and catalyst deactivation, respectively. Considering the deactivation, the rate of the reaction is

$$Rate = \frac{k_{N+1}k_N[R][C]}{(k_{-N} + k_{N+1} + k_d)} \tag{6.1}$$

In *MaxKinEff*, during catalysis, the active species are consumed and thereby decrease its efficiency. However, there may be the possibility of multiple pathways for the deactivation of catalysts. Hence, it is very difficult to portray the deactivation pathways.[14] In *MaxKinEff*, the amount of catalyst that remains active, $\boldsymbol{C}_1$ will carry forward the reaction as $\boldsymbol{C}_2$, $\boldsymbol{C}_3$, ... $\boldsymbol{C}_{N-1}$, and $\boldsymbol{C}_N$, until it gets consumed. Following the reaction, the catalysts eliminate the product, $\boldsymbol{P}$, and subsequently regenerate $\boldsymbol{C}$ [Figure 4.2, *vide supra*]. Therefore, as the reaction progresses, the catalyst concentration decreases. Thus, an increase in catalyst loading proves beneficial in countering the effect. The catalytic cycle will continue to form the product when the catalyst concentration is very high. However, if the rate of deactivation is high, then complete conversion is not attainable. Therefore, if the deactivation of the catalyst becomes dominant, *i.e.*, $k_d >> k_{-N}$, and $k_d >> k_{N+1}$, then, $k_{-N} + k_{N+1} + k_d \cong k_d$. Thus, the Eq. (6.1) changes to

$$Rate = \frac{k_{N+1}k_N[R][C]}{k_d} \tag{6.2}$$

Hence, the rate of the reaction is first order to reactant, $\boldsymbol{R}$ and first order to the catalyst, $\boldsymbol{C}$. On the other hand, if the deactivation barrier is very high and catalysis is dominant, then k_d is very small. In that case, $k_d << k_{N+1}$, and $k_{N+1} >> k_{-N}$, which implies that $k_{-N} + k_{N+1} + k_d \cong k_{N+1}$. Therefore, in such cases, deactivation

may be ignored and is more apparent at low concentrations. The Eq. (6.1) becomes

$$Rate = \frac{k_{N+1}k_N[R][C]}{k_{N+1}} = k_N[R][C] \tag{6.3}$$

Thus, the rate of the reaction is first order to reactant, $\boldsymbol{R}$ and first order to the catalyst, $\boldsymbol{C}$.

In contrast, the ECM considers only the rate-determining step (RDS) of the catalytic cycle. The model assumes the improvement in the kinetic behavior that signifies the catalyst performance. In ECM, the TOF is directly proportional to the tunnelling corrected rate constants, $k_{overall}(T)$. Nevertheless, the detailed consideration of catalyst deactivation will be amended in the ECM strategy in the future.

Further, the computed turnover frequency, $\Gamma^0_{computed\ TOF}$ is obtained through the ECM strategy, a concentration-dependent model. The dependence in concentration may be observed from both kinetic and thermodynamic perspectives. From a kinetic perspective, the higher the concentration of species involved, the higher the probability of transmission. This will eventually increase the $\Gamma^0_{computed\ TOF}$. In addition, ECM states that among the available $\boldsymbol{N_0}$ catalyst molecules, all molecules may not lead to product formation. ECM approximates that the probability of the effective number of product molecules ($\boldsymbol{N}$) formed per catalyst molecule per unit time, *i.e.* $\frac{N}{N_0}$ must possess the minimum thermodynamic energy, E_{ECE}, to drive the catalytic

reaction successfully.

As stated, both models compute the efficiencies in terms of TOFs and TONs. During a catalytic cycle, a catalyst remains alive in the catalytic cycle until it is exhausted. Under the half-life regime, *MaxKinEff* evaluates the maximum number of turns that a catalyst may cover per active site per unit time, defined as $\Gamma^0_{max\ TOF}$ when the reactant molecules react in the proper orientation and activation energy, E_a. The model also depicts the maximum number of turns that the catalyst can make before it gets deactivated, denoted as $\tau^0_{max\ TON}$. On the other hand, ECM computes only the turnovers of the catalyst without considering its maximum value.

The collision theory is the bedrock of the *MaxKinEff* model, in which it was assumed that the reactants and catalysts are hard spheres and collide with all the molecules coming within the collision diameter. Alternatively, in the case of the ECM model, the assumptions of such collisions were not taken and were established based on the chosen kinetic and thermodynamic parameters. For instance, we have defined the efficiency conceptualized energy, E_{ECE}, necessary for the reaction to occur, which may be considered parallel to the activation energy, E_a. However, the difference is that the E_{ECE} is the thermodynamic threshold energy that drives catalytic reactions successfully, whereas activation energy, E_a, is the kinetic threshold energy.

Further, ECM and *MaxKinEff* use different parameters for predicting the efficiency of catalysts. The ECM uses the kinetic parameter, TST rate constants cor-

rected with the transmission coefficient (κ),[56] and the thermodynamic parameters, the $\Delta G_{r,RDS}$, and the α measured in terms of the E_f of the catalysts. On the other hand, *MaxKinEff* utilizes the activation energy, E_a, of the reaction step in which the rate of the reaction depends and the corresponding collision diameter, σ_{RC}, of the reactant-substrate complex.

Another important point where both models contrast, is in the approach for the computation of the $\tau^0_{max\ TON}$ in *MaxKinEff* and $\tau^0_{computed\ TON}$ in ECM. In ECM, we consider the relation proposed by Kozuch *et al.* given by[11]

$$\tau^0_{computed\ TON} = \frac{\Gamma^0_{computed\ TOF} \times t_{\frac{1}{2}}}{ln\ 2} \tag{6.4}$$

In the case of *MaxKinEff*, in $t_{\frac{1}{2}}$ time, the $\tau^0_{max\ TON} = (\Gamma^0_{max\ TOF} \times \mathbf{t}_{\frac{1}{2}})$

where

$$t_{\frac{1}{2}} = \frac{2ln\ 2 + K^{\neq}[C]_0}{2k_1[R]_0} \tag{6.5}$$

In Eq. (6.5) k_1 is the TST rate constant, $[R]_0$ and $[C]_0$ are the initial concentrations of the reactant and catalyst, respectively, and $K^{\neq}$ is the equilibrium constant of the reaction.

Since both models have different assumptions and considerations with different perspectives, there exists a variation in the results in predicting the TOFs of catalysts. Further, it has to be kept in mind that the models were constructed not to mimic

the experimental result but rather to observe a trend in the turnover numbers and frequencies.

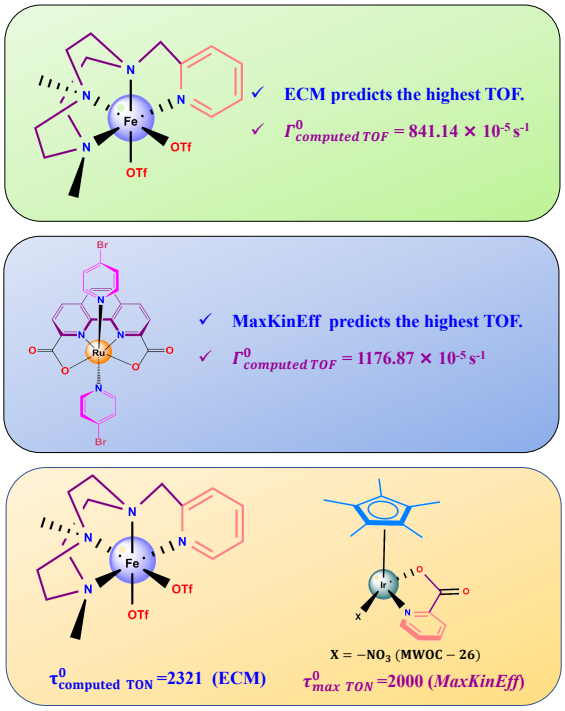

Figure 6.1: Illustration of results from efficiency conceptualization model (ECM) and maximum kinetic efficiency (*MaxKinEff*).

To understand the model, after the formulation, it is always essential to validate the results with experimental values. The validation becomes more meaningful when we apply both models to identical reactions under the same reaction conditions. This is because applying the model to identical reactions with the same set of catalysts will provide us with information on similarities, differences, and, most importantly, the accuracy of the models. In our case, for computing TONs, we have considered the experimentally defined conditions of temperature, pressure (1 atm),

and pH for validating the results from both models. However, the results showed that with ECM, [Fe(OTf)$_2$(Me$_2$Pytacn)], the iron-based catalyst reports the highest $\Gamma^0_{computed\ TOF}$ of 841.14 $\times$ 10^{-5} s^{-1}, indicating it is the most efficient catalyst for the water-oxidation reaction. On the other hand, with the *MaxKinEff*, the ruthenium pda catalyst [Ru(pda)(Br-py)$_2$] shows the highest $\Gamma^0_{max\ TOF}$ of 1176.87 $\times$ 10^{-5} s^{-1}. ECM predicts that [Fe(OTf)$_2$(Me$_2$Pytacn)] shows highest value of $\tau^0_{computed\ TON}$= 2321, while *MaxKinEff* indicates that the catalyst [Cp*Ir(κ^2-N,O)NO$_3$] exhibits the highest value, $\tau^0_{max\ TON}$= 2000; $\tau^0_{experimental\ TON}$ = 2000.[139] Exploring the observation, we found that in *MaxKinEff*, although the catalyst [Cp*Ir(κ^2-N,O)NO$_3$] possesses a lower number of turns, a longer half-life makes it more efficient in terms of the TON. Figure 6.1 summarizes the results observed from both catalytic models.

6.3 Concluding Remarks

From the above discussion, we conclude that the developed models provide important information regarding catalysis. Therefore, it is essential to acknowledge that the distinct assumptions of each model may be used to forecast the efficiency of catalysts depending on the requirements. At the current stage, the models have been developed under experimental conditions of temperature, pressure and pH. However, the factors that limit the efficiency of catalysts will be addressed, and subsequent amendments will be made in the future.

7

Summary and Conclusions

In catalysis, turnover number (TON) and turnover frequency (TOF) are two critical parameters. The TON indicates the number of turns completed per unit time by a catalyst during the conversion of the reactant to the product before its deactivation. Numerous research endeavours have aimed to unravel the catalytic efficiency. Owing to the catalyst deactivation, reaction conditions, catalyst structure, and the nature of the reactants involved, attaining high TONs remains challenging. Thus, there is a high need for the formulation of catalytic tools. The thesis discusses the formulation of two theoretical catalytic models and their applications in the context of the water-oxidation reaction and summarizes the work as follows.

Chapter 1 introduces the thesis that provides the basic understanding of catalysis along with the two basic efficiency parameters, turnover number (TON) and turnover

frequency (TOF). The chapter also discusses the existing catalytic models used to predict efficiency and recent advances in theoretical tools for catalysis. Finally, the chapter concludes by discussing the goals of the thesis.

Chapter 2 discusses the formulation of the efficiency conceptualization model (ECM). ECM depends on the kinetic and thermodynamic parameters of the rate-determining step (RDS). From the kinetic perspective, it calculates rate constants and is further corrected by the Eckart and the Wigner tunnelling methods. From the thermodynamic perspective, the model calculates the feasibility of reactions and the stability parameter of catalysts. The chosen kinetic and thermodynamic parameters are integrated to derive the turnover frequency, $\Gamma^0_{computed\ TOF}$ of the catalyst. The $\Gamma^0_{computed\ TOF}$ is further extended to compute the turnover number, $\tau^0_{computed\ TON}$, thereby offering a comprehensive understanding of the efficiency metrics.

Chapter 3 investigates the molecular water-oxidation reaction using twenty-six transition metal catalysts. Under the chosen experimental environments, the efficiency of the catalyst was predicted in terms of the TONs and TOFs. Among the twenty-six catalysts, the majority of the complexes contain ruthenium as an active centre. However, it also consists of catalysts with first and third-row transition metals in the active centre. Our results suggest that the iron based catalyst, $[Fe(OTf)_2(Me_2Pytacn)]$ has the highest TOF of 841.14×10^{-5} s^{-1}, demonstrating high activity and robustness within the catalytic cycle. In addition, the same cata-

lyst showed impressive efficiency in producing O_2 with the highest computed turnover numbers, $\tau^0_{computed\ TON}$ of 2321. The computed TONs have a strong correlation with the experimental TONs with Pearson's correlational analysis value, $r = 0.92$. The Pearson's r value suggests a strong correlation between the computed TONs and experimental TONs for the chosen catalysts.

In Chapter 4, mathematically we formulate the *MaxKinEff* model for prediction of the maximum turnover frequency, $\Gamma^0_{max\ TOF}$, of a catalyst. The *MaxKinEff* considers the catalyst deactivation process of the catalytic cycle and calculates the rate of the reaction. With the collision theory as the basis, the strategy predicts the activation energy (E_a) and collision diameter (σ_{RC}) and computes the maximum turnover frequency, $\Gamma^0_{max\ TOF}$, considering the favourable orientations of the catalyst and reactant.

Chapter 5 explores the application of water oxidation reaction to predict both the maximum turnover frequency, $\Gamma^0_{max\ TOF}$, and the maximum turnover number, $\tau^0_{max\ TON}$, of catalysts. Using the same set of twenty-six catalysts as in the previous chapter, the *MaxKinEff* model identifies the carboxylate-based Ru-pda catalyst, [Ru(pda)(Br-py)$_2$] with an axial Bromopyridine (Br-py) ligand as the most efficient. The computed normalized $\tau^0_{max\ TON}$ values reveal that the Iridium (Ir)-centred catalyst, [Cp*Ir(κ^2-N,O)Cl] achieves a $\tau^0_{max\ TON}$ of 913, resembling with its experimental value of 1200. In addition, [Cp*Ir(κ^2-N,O)NO_3] is reported to possess a normalized

computed $\tau^0_{max\ TON}$ of 2000, which is in good agreement with the experimental TON of 2000. The validity of the model was checked using Pearson's correlational analysis that shows $r = 0.77$. The Pearson's r value suggests a strong correlation between the computed TONs and experimental TONs for the chosen catalysts.

After establishing the two models, in Chapter 6, we provide a comparative overview of two established models. While much of the effort has been dedicated to formulate the ECM and *MaxKinEff* models, we hope that these models will help other researchers to apply them in different catalytic reactions. In future, the formulated models may be integrated with machine learning to enhance the accuracy of the models.

8

Appendix

In the Appendix, we have added

1. The transition state theory (TST), Eckart and Wigner Tunnelling rate constants (both are in s^{-1}) in MN15-L level of theory.

2. Feasibility and stability of catalysts in MN15-L level of theory.

3. The experimental TONs and conditions ($\tau^0_{experimental\ TON}$) of all chosen catalysts.

4. All geometries of the transition state (TS) along with the imaginary frequencies.

5. The highest occupied molecular orbitals (HOMO) and Lowest unoccupied molecular orbitals (LUMO) with their energies. All the energies were reported in

Hartree.

6. The experimental conditions of temperature, pH, and the experimental TON ($\tau^{0}_{experimental\ TON}$) of all chosen catalysts.

7. $< S^2 >$ expectation values for the representative $[M^{V}{=}O]^{(n+1)+}$ complexes with the (M = metal atom and n = 0, 1, 2) complexes calculated with MN15-L and M06-L functional employed with LANL2DZ ECP for all the metal (M) atoms (M = Mn, Fe, Co, Ni, Cu, Ru, and Ir) and Br atom and 6-31G(d) basis set for remaining elements in the solvent phase.

8. Zero-point corrected electronic energies of the complexes in solvent phase with MN15-L and M06-L functionals employed with LANL2DZ ECP for all the metal (M) atoms (M = Mn, Fe, Co, Ni, Cu, Ru, and Ir) and Br atom and 6-31G(d) basis set for remaining elements. All the energies were reported in Hartree.

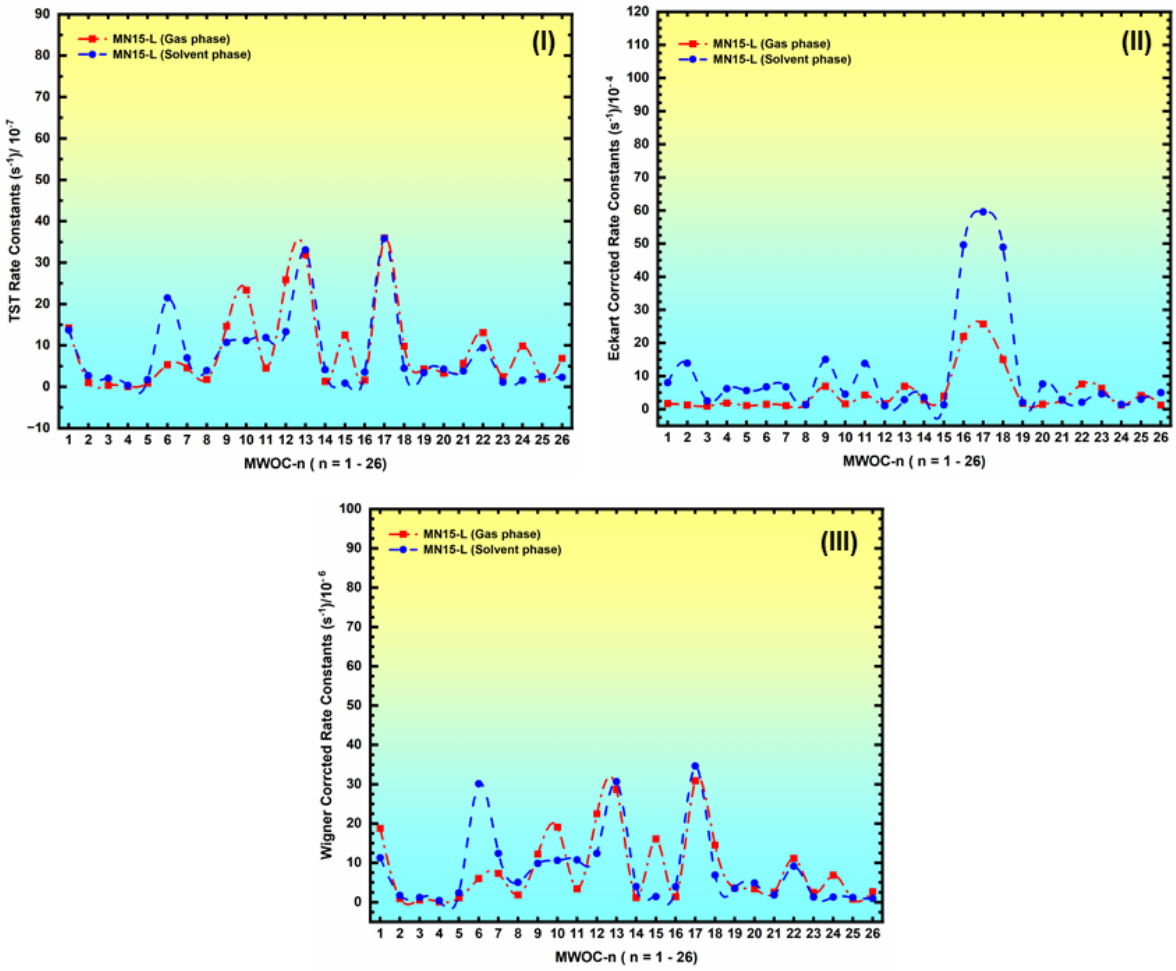

Figure 8.1: (I) Transition State Theory (TST) rate constants (s^{-1}), (II) Eckart tunnelling corrected rate constants (s^{-1}), and (III) Wigner tunnelling corrected rate constants (s^{-1}) for twenty-six catalysts in gas phase and solvent phase using the solvation model density (SMD). MN15-L level of theory was implemented with LANL2DZ ECP for all the metal (M) atoms (M = Mn, Fe, Co, Ni, Cu, Ru, and Ir) and Br atom, and 6-31G(d) basis set for remaining elements.

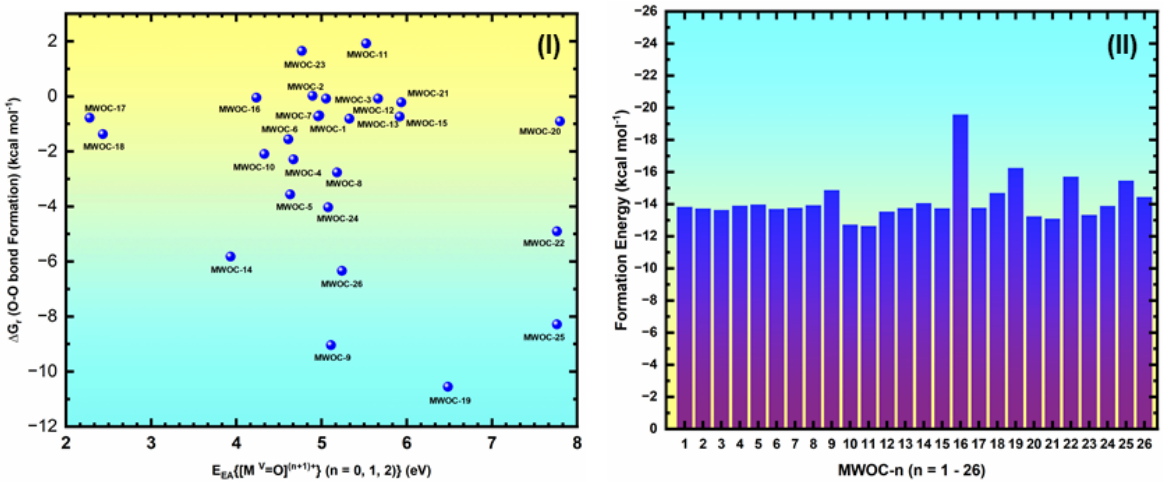

Figure 8.2: Variations in the (I) feasibility of the reaction, ΔG_r (O-O bond formation) in solvent phase (in kcal mol^{-1}); (II) Formation energies (in kcal mol^{-1}) involved in the rate-limiting O-O bond formation step of representative twenty-six catalysts in the MN15-L level of theory using the solvation model density (SMD). MN15-L level of theory was implemented with LANL2DZ ECP for all the metal (M) atoms (M = Mn, Fe, Co, Ni, Cu, Ru, and Ir) and Br atom, and 6-31G(d) basis set for remaining elements.

Table 8.1: The transition state (TS) structures of the O-O bond formation process with the corresponding imaginary frequencies (in cm^{-1}).

MWOC	TS Structure for the O-O bond formation process	Imaginary Frequency	
		MN15-L	M06-L
MWOC -1	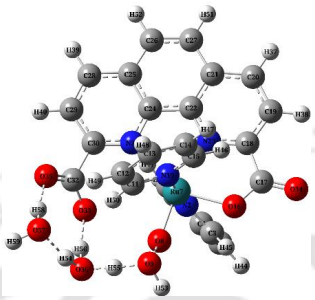	-557.94	-676.43
MWOC -2	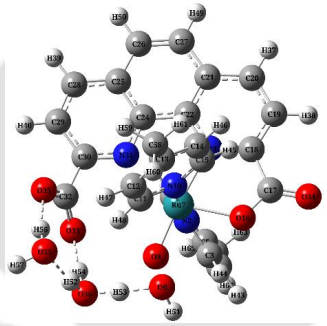	-456.36	-596.35
MWOC -3	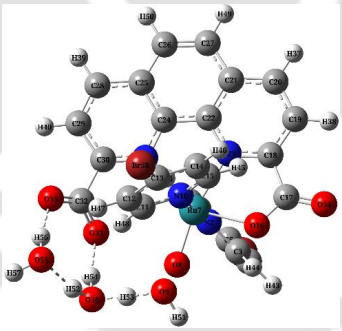	-641.32	-657.36
MWOC -4	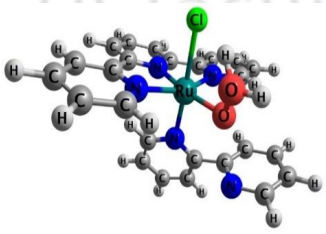	-522.77	-543.23

MWOC -5	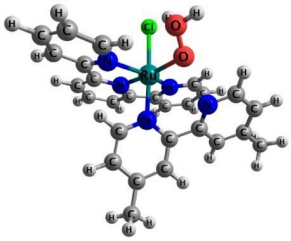	**-573.66**	**-575.13**
MWOC -6	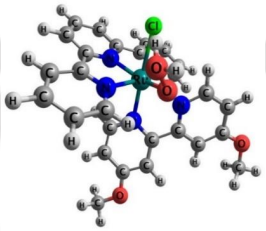	**-576.43**	**-597.96**
MWOC -7	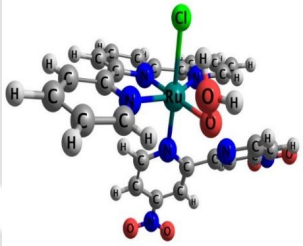	**-653.95**	**-667.03**
MWOC -8	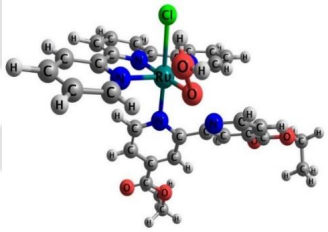	**-553.07**	**-574.13**
MWOC -9	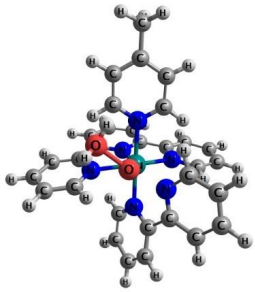	**-457.32**	**-496.47**

MWOC -10	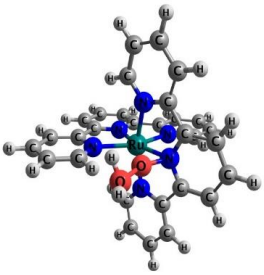	**-466.08**	**-465.40**
MWOC -11	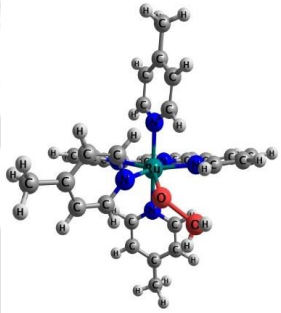	**-451.98**	**-441.02**
MWOC -12	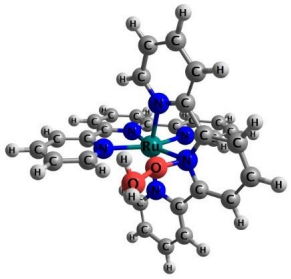	**-461.40**	**-480.63**
MWOC -13	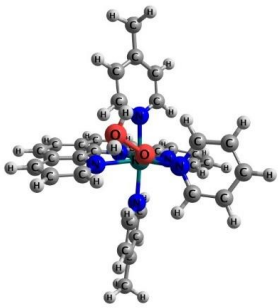	**-459.11**	**-488.29**
MWOC -14	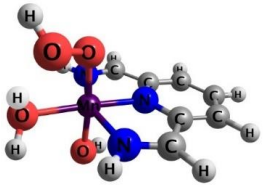	**-467.11**	**-446.45**

MWOC -15	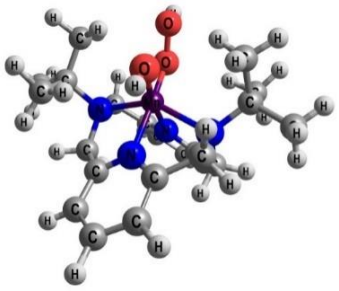	**-619.59**	**-631.98**
MWOC -16	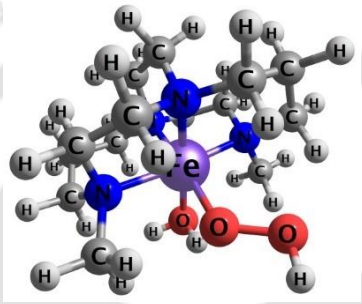	**-507.13**	**-521.27**
MWOC -17	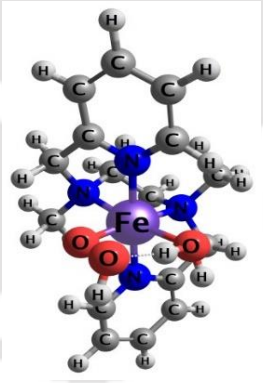	**-469.97**	**-499.37**
MWOC -18	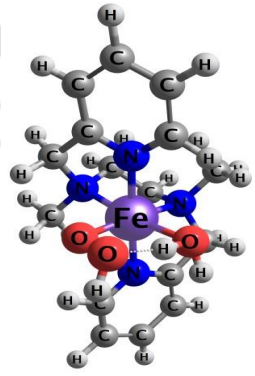	**-606.31**	**-608.44**

MWOC -19	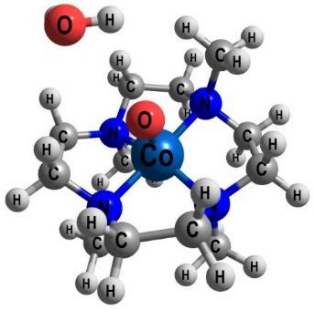	**-486.95**	**-466.69**
MWOC -20	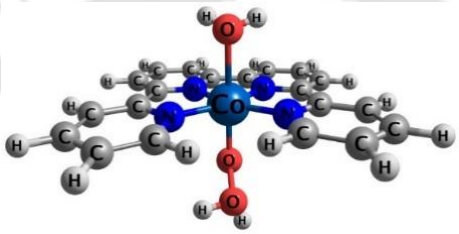	**-514.50**	**-514.79**
MWOC -21	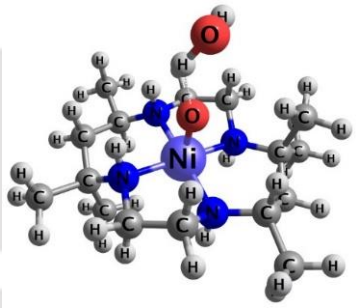	**-307.48**	**-323.63**
MWOC -22	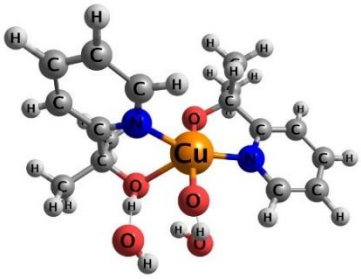	**-471.07**	**-490.49**

MWOC -23	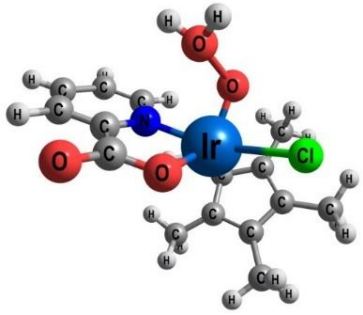	**-526.26**	**-526.79**
MWOC -24	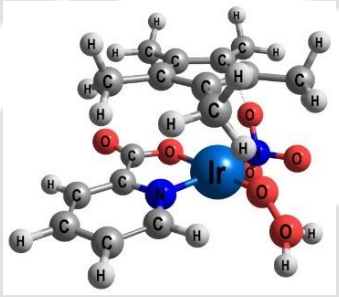	**-438.25**	**-457.02**
MWOC -25	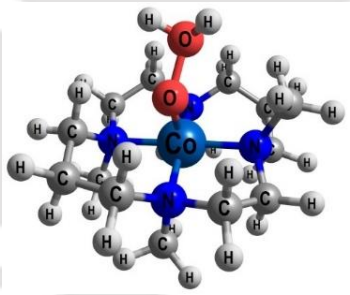	**-304.97**	**-316.07**
MWOC -26	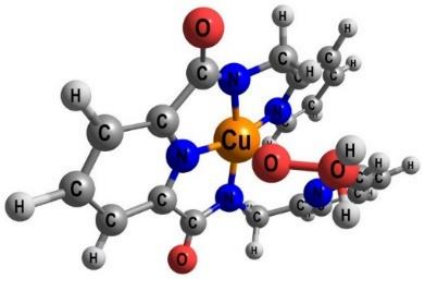	**-284.54**	**-295.23**

Table 8.2: The HOMOs and LUMOs for the representative $[M^{V}{=}O]^{(n+1)+}$ (n = 0, 1, 2) at the MN15-L functional employed with LANL2DZ ECP for all the metal (M) atoms (M = Mn, Fe, Co, Ni, Cu, Ru, and Ir) and Br atom and 6-31G(d) basis set for remaining elements. The values in the brackets represent the orbital energy in Hartree.

MWOC	HOMO	LUMO
MWOC-1	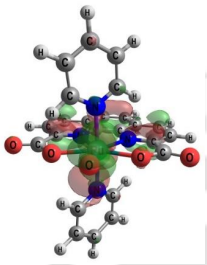 E = -0.23283 Hartree	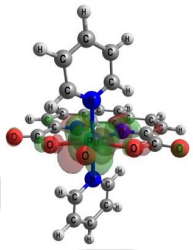 E = -0.18284 Hartree
MWOC-2	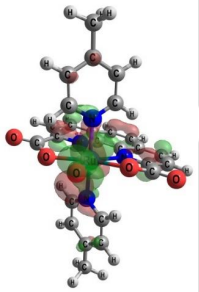 E = -0.22925 Hartree	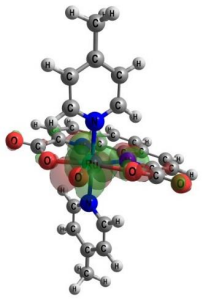 E = -0.17993 Hartree
MWOC-3	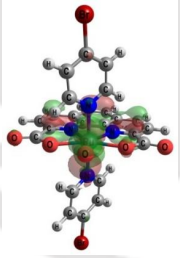 E = -0.23557 Hartree	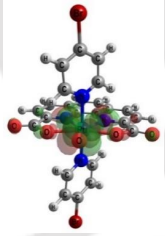 E = -0.18577 Hartree
MWOC-4	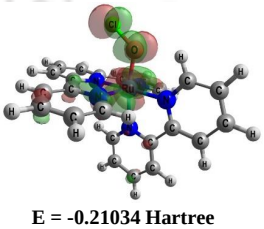 E = -0.21034 Hartree	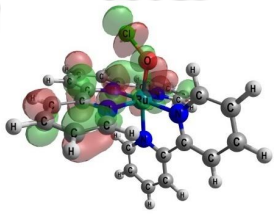 E = -0.17171 Hartree

MWOC-5	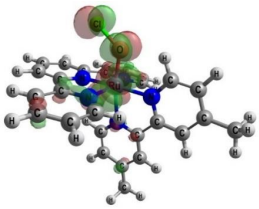 **E = -0.20890 Hartree**	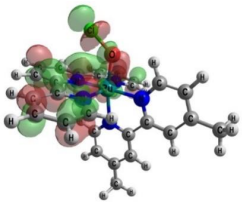 **E = -0.17028 Hartree**
MWOC-6	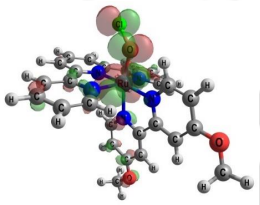 **E = -0.20765 Hartree**	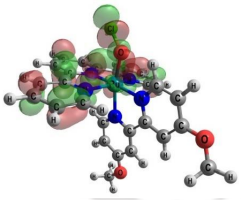 **E = -0.16954 Hartree**
MWOC-7	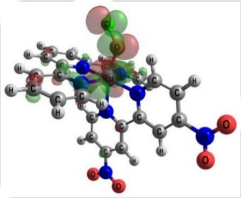 **E = -0.21912 Hartree**	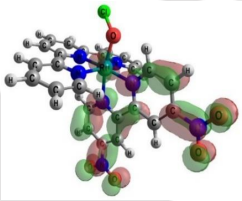 **E = -0.18238 Hartree**
MWOC-8	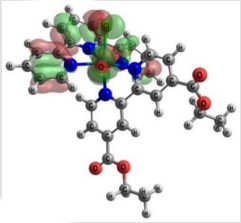 **E = -0.24100 Hartree**	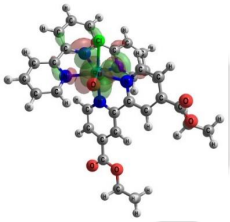 **E = -0.19049 Hartree**
MWOC-9	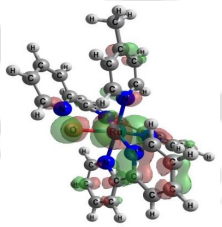 **E = -0.23797 Hartree**	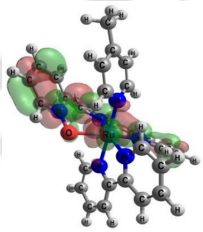 **E = -0.18792 Hartree**

MWOC-10	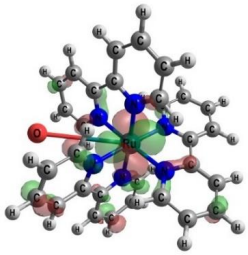 **E = -0.23604 Hartree**	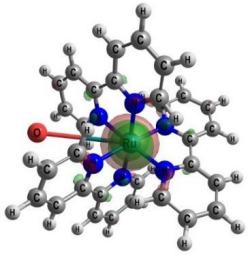 **E = -0.15910 Hartree**
MWOC-11	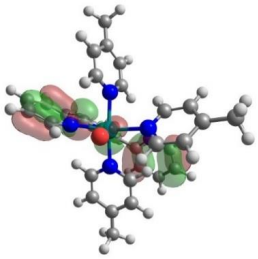 **E = -0.23958 Hartree**	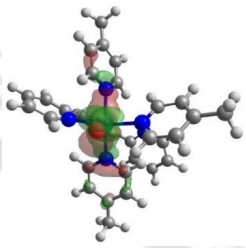 **E = -0.20304 Hartree**
MWOC-12	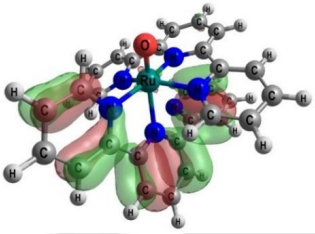 **E = -0.24403 Hartree**	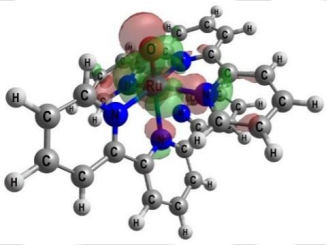 **E = -0.20823 Hartree**
MWOC-13	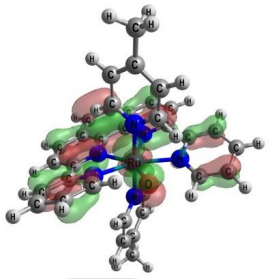 **E = -0.23537 Hartree**	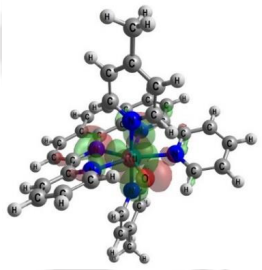 **E = -0.19579 Hartree**
MWOC-14	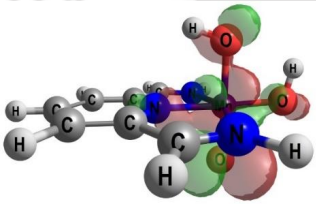 **E = -0.23803 Hartree**	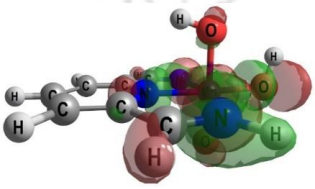 **E = -0.14455 Hartree**

MWOC-15	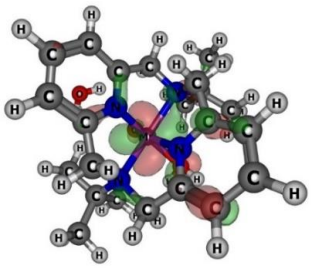 **E = -0.25666 Hartree**	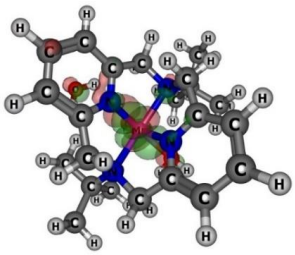 **E = -0.21755 Hartree**
MWOC-16	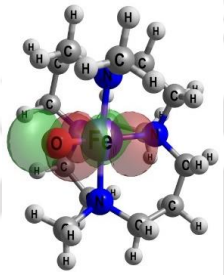 **E = -0.22912 Hartree**	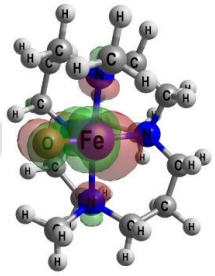 **E = -0.15576 Hartree**
MWOC-17	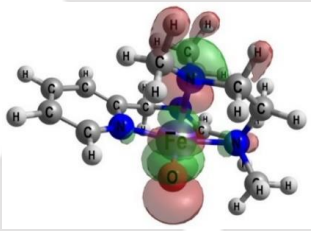 **E = -0.25920 Hartree**	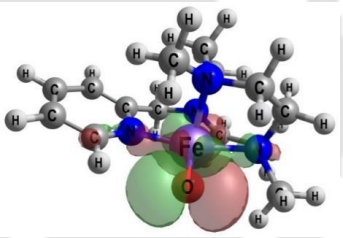 **E = -0.18927 Hartree**
MWOC-18	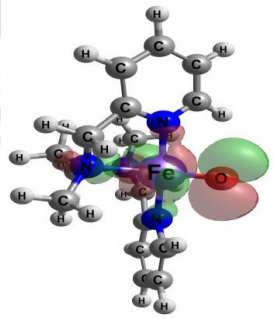 **E = -0.25602 Hartree**	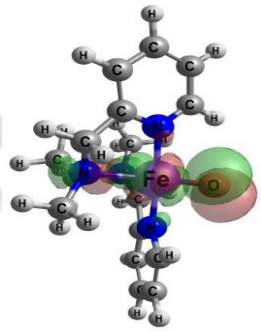 **E = -0.19547 Hartree**

MWOC-19	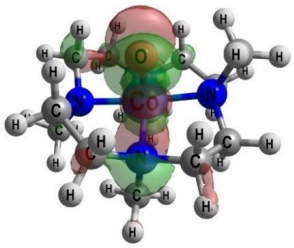 **E = -0.25014 Hartree**	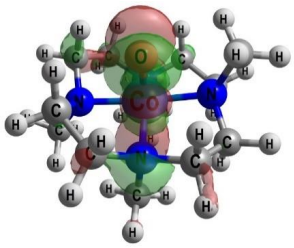 **E = -0.23836 Hartree**
MWOC-20	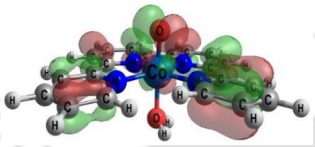 **E = -0.25584 Hartree**	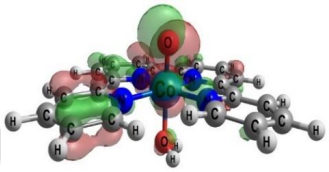 **E = -0.28666 Hartree**
MWOC-21	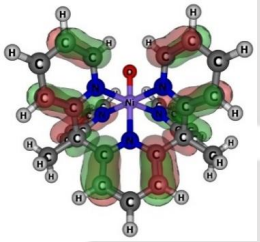 **E = -0.29086 Hartree**	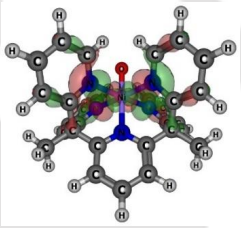 **E = -0.23573 Hartree**
MWOC-22	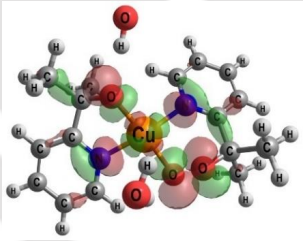 **E = -0.16452 Hartree**	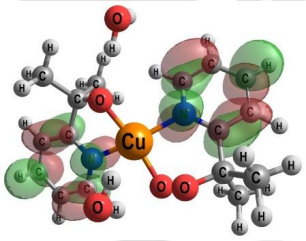 **E = -0.12173 Hartree**
MWOC-23	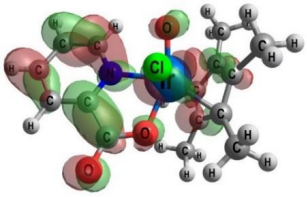 **E = -0.23938 Hartree**	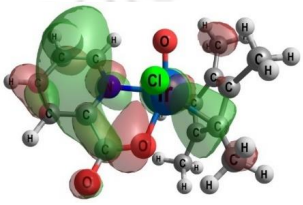 **E = -0.17528 Hartree**

MWOC-24	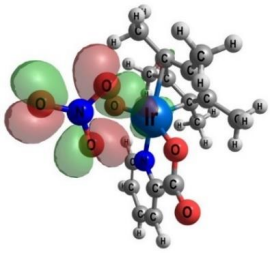 **E = -0.21633 Hartree**	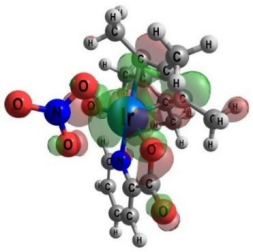 **E = -0.18670 Hartree**
MWOC-25	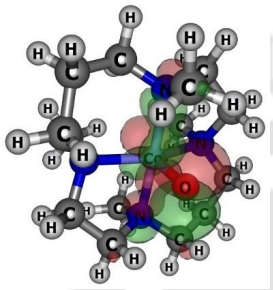 **E = -0.24911 Hartree**	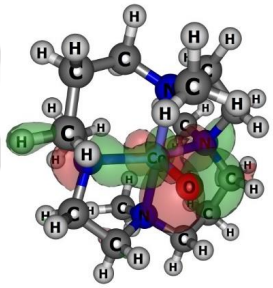 **E=0.28543 Hartree**
MWOC-26	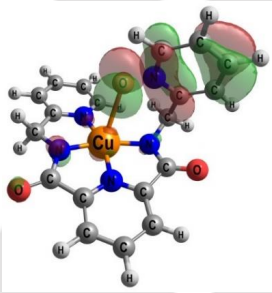 **E = -0.21408 Hartree**	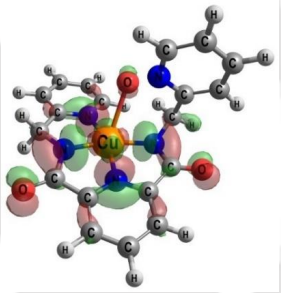 **E = -0.19265 Hartree**

Table 8.3: The HOMOs and LUMOs for the representative $[M]^{n+}$ (n = 0, 1, 2) at the MN15-L functional employed with LANL2DZ ECP for all the metal (M) atoms (M = Mn, Fe, Co, Ni, Cu, Ru, and Ir) and Br atom and 6-31G(d) basis set for remaining elements. The values in the brackets represent the orbital energy in Hartree.

MWOC	HOMO	LUMO
MWOC-1	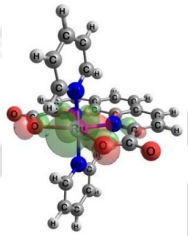 **E = -0.15826 Hartree**	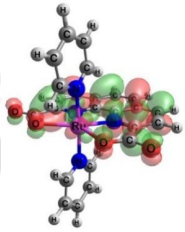 **E = -0.09813 Hartree**
MWOC-2	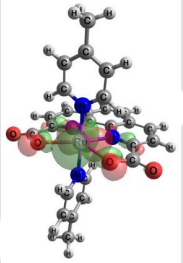 **E = -0.15868 Hartree**	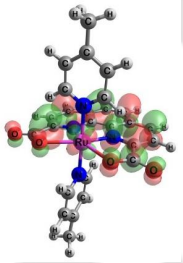 **E = -0.17993 Hartree**
MWOC-3	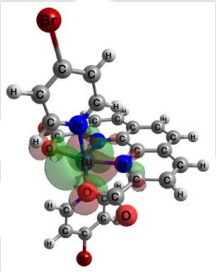 **E = -0.16080 Hartree**	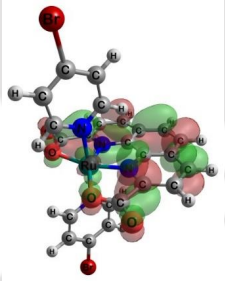 **E = -0.09949 Hartree**
MWOC-4	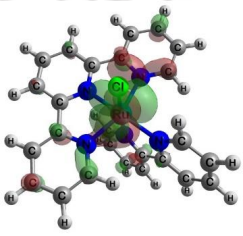 **E = -0.17103 Hartree**	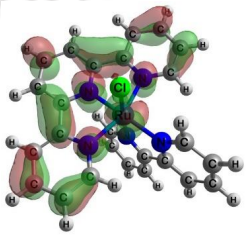 **E = -0.09561 Hartree**

MWOC-5	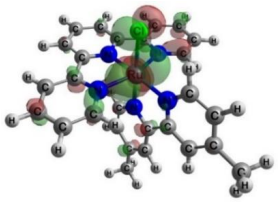 **E = -0.16917 Hartree**	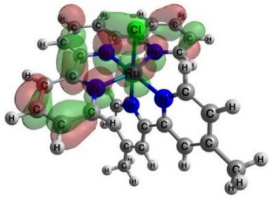 **E = -0.09491 Hartree**
MWOC-6	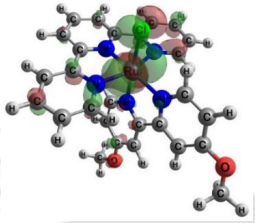 **E = -0.16678 Hartree**	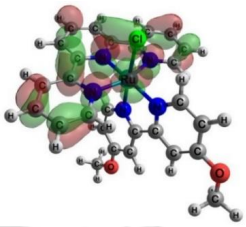 **E = -0.09416 Hartree**
MWOC-7	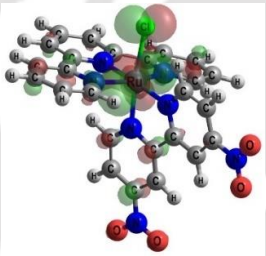 **E = -0.06886 Hartree**	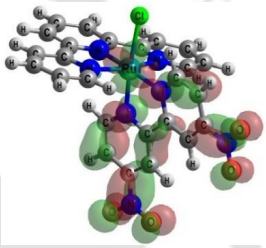 **E = -0.05378 Hartree**
MWOC-8	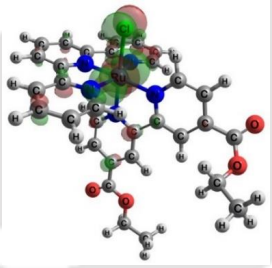 **E = -0.17821 Hartree**	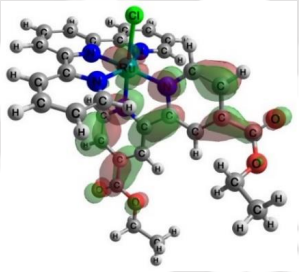 **E = -0.10981 Hartree**
MWOC-9	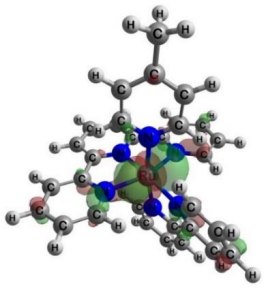 **E = -0.18296 Hartree**	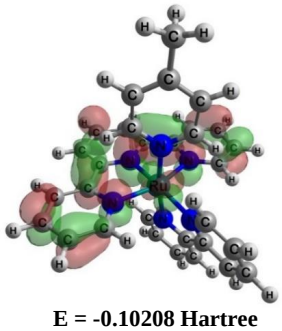 **E = -0.10208 Hartree**

MWOC-10	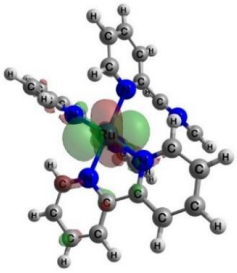 **E = -0.17960 Hartree**	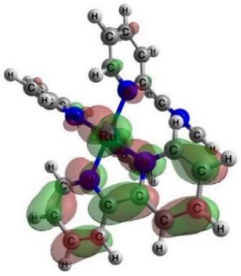 **E = -0.10000 Hartree**
MWOC-11	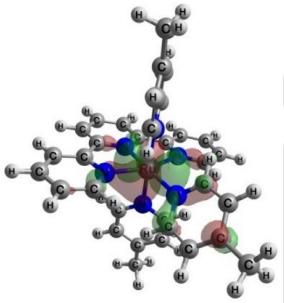 **E = -0.18167 Hartree**	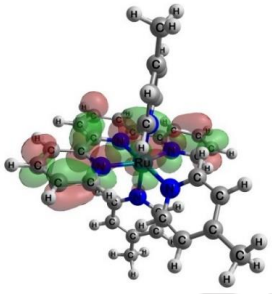 **E = -0.10200 Hartree**
MWOC-12	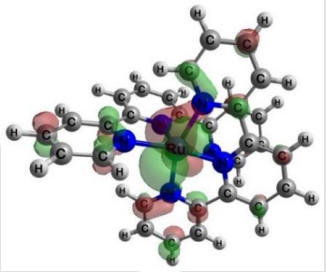 **E = -0.18175 Hartree**	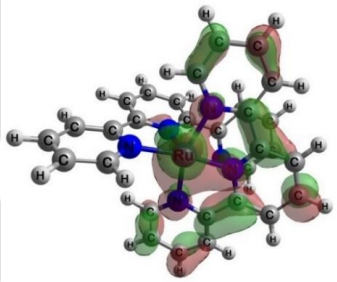 **E = -0.11140 Hartree**
MWOC-13	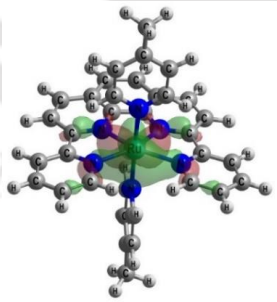 **E = -0.17692 Hartree**	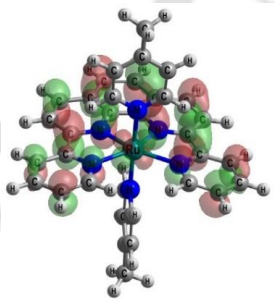 **E = -0.10922 Hartree**

MWOC-14	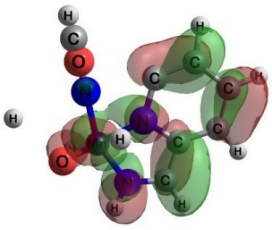 **E = -0.23803 Hartree**	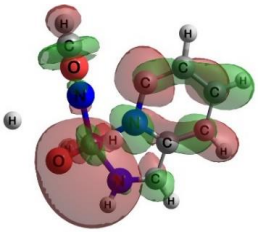 **E = -0.14455 Hartree**
MWOC-15	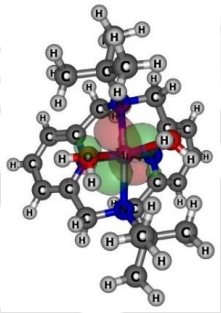 **E = -0.16335 Hartree**	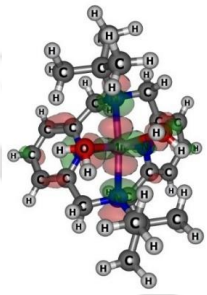 **E = -0.08172 Hartree**
MWOC-16	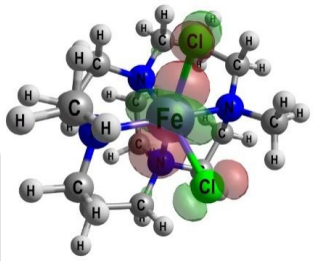 **E = -0.16734 Hartree**	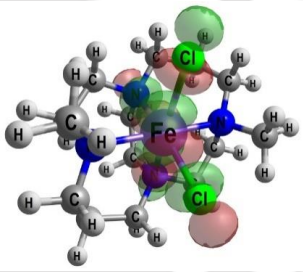 **E = -0.11851 Hartree**
MWOC-17	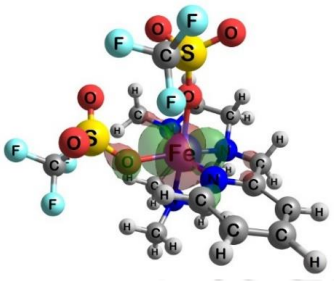 **E = -0.14174 Hartree**	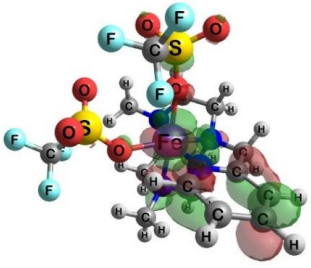 **E = -0.06061 Hartree**

MWOC-18	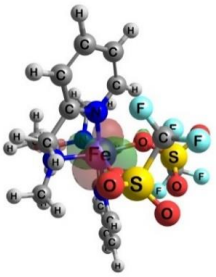 **E = -0.15061 Hartree**	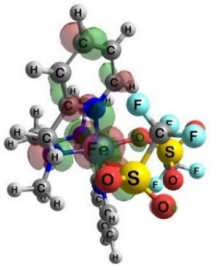 **E = -0.06510 Hartree**
MWOC-19	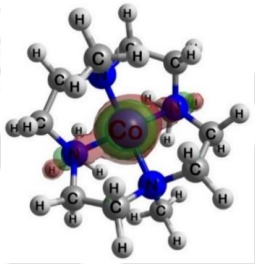 **E = -0.19136 Hartree**	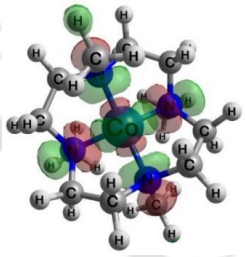 **E = -0.10232 Hartree**
MWOC-20	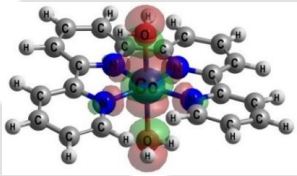 **E = -0.19953 Hartree**	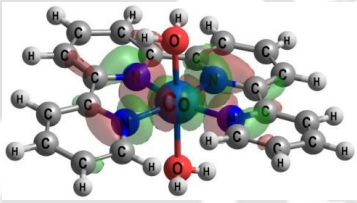 **E = -0.11849 Hartree**
MWOC-21	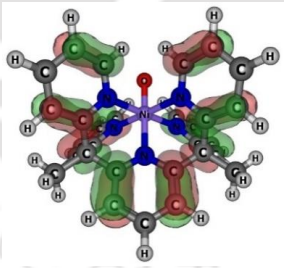 **E = -0.18247 Hartree**	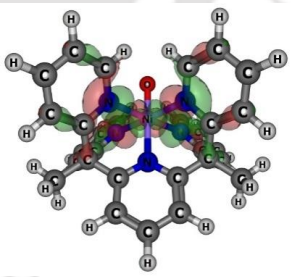 **E = -0.10760 Hartree**

MWOC-22	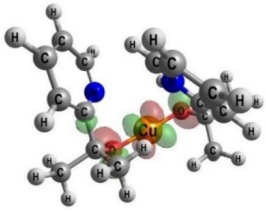 **E = -0.13016 Hartree**	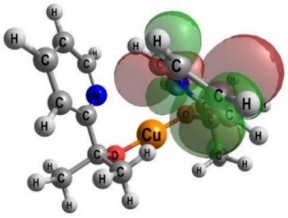 **E = -0.07982 Hartree**
MWOC-23	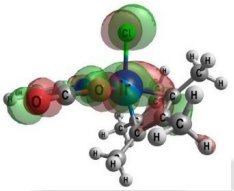 **E = -0.22716 Hartree**	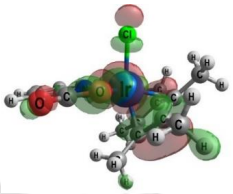 **E = -0.18914 Hartree**
MWOC-24	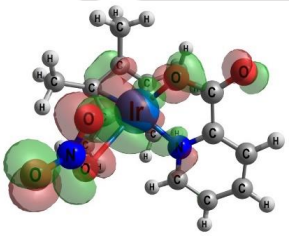 **E = -0.21363 Hartree**	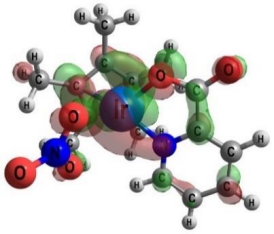 **E = -0.17704 Hartree**
MWOC-25	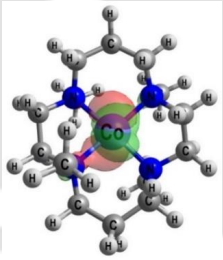 **E = -0.18421 Hartree**	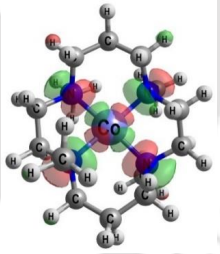 **E = -0.17704 Hartree**
MWOC-26	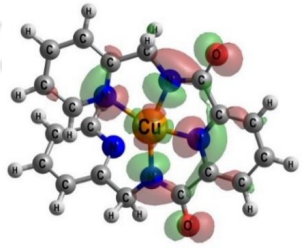 **E = -0.18300 Hartree**	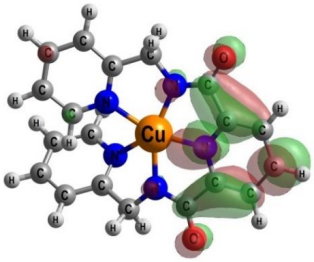 **E = -0.14173 Hartree**

Table 8.4: $< S^2 >$ expectation values for the representative $[M^V{=}O]^{(n+1)+}$ complexes with the (M = metal atom and n = 0, 1, 2) complexes calculated with MN15-L and M06-L functional employed with LANL2DZ ECP for all the metal (M) atoms (M = Mn, Fe, Co, Ni, Cu, Ru, and Ir) and Br atom and 6-31G(d) basis set for remaining elements in the solvent phase.

MWOC	**Solvent phase**		
	MN15-L	**M06-L**	$< \widehat{S^2} > = S(S+1)\hbar^2$
MWOC -1	0.7503	0.7502	0.7500
MWOC -2	0.7503	0.7502	0.7500
MWOC -3	0.7503	0.7502	0.7500
MWOC -4	0.7501	0.7502	0.7500
MWOC -5	0.7501	0.7502	0.7500
MWOC -6	0.7501	0.7502	0.7500
MWOC -7	0.7501	0.7501	0.7500
MWOC -8	0.7504	0.7502	0.7500
MWOC -9	0.7501	0.7501	0.7500
MWOC -10	0.8148	0.8099	0.7500
MWOC -11	0.7502	0.7501	0.7500
MWOC -12	0.7503	0.7501	0.7500
MWOC -13	0.7502	0.7501	0.7500
MWOC -14	2.2392	2.0186	2.0000
MWOC -15	_[c]	_[c]	_[c]
MWOC -16	_[c]	_[c]	_[c]
MWOC -17	_[c]	_[c]	_[c]
MWOC -18	0.0387	0.0243	3.7500
MWOC -19	_[c]	_[c]	_[c]
MWOC -20	_[c]	_[c]	_[c]
MWOC -21	0.7503	0.7502	0.7500
MWOC -22	0.7500	0.7500	0.7500
MWOC -23	0.7504	0.7507	0.7500
MWOC -24	0.7505	0.7503	0.7500
MWOC -25	_[c]	_[c]	_[c]
MWOC -26	_[c]	_[c]	_[c]

_[c] Spin contamination value not reported in the output file (closed-shell system).

Table 8.5: Zero-point corrected optimized energies (absolute and relative energies) of the representative $[\mathbf{M}^{\mathrm{II}}]^{n+}$ complexes in the solvent phase. All the energies were reported in Hartree.

MWOC	**Solvent Phase**			
	Absolute Energy (MN15-L)	**Relative Energy (MN15-L)**	**Absolute Energy (M06-L)**	**Relative Energy (M06-L)**
MWOC -1	-1536.2215	1350.1273	-1537.6816	1349.2308
MWOC -2	-1614.7192	1271.5556	-1616.2533	1270.7331
MWOC -3	-1561.2715	1325.0001	-1562.8088	1324.1808
MWOC -4	-1790.1145	1096.3396	-1791.4693	1095.3378
MWOC -5	-1868.6095	1017.7693	-1870.0396	1016.8428
MWOC -6	-2019.3380	717.1683	-2170.6406	866.1143
MWOC -7	-2198.7551	687.5568	-2200.2521	686.6972
MWOC -8	-2323.8560	562.1578	-2325.6511	561.5963
MWOC -9	-1617.0560	1269.2300	-1618.5789	1268.3963
MWOC -10	-1577.7777	1308.5475	-1579.2614	1307.6746
MWOC -11	-1696.7022	1189.4996	-1698.3093	1188.7501
MWOC -12	-1576.6216	1309.7161	-1578.0928	1308.8307
MWOC -13	-1732.4501	1153.7529	-1734.0560	1153.0022
MWOC -14	-764.5399	2122.1222	-765.6867	2120.9124
MWOC -15	-1330.8944	1555.2751	-1332.5338	1554.5579
MWOC -16	-1812.4408	1075.3681	-1812.4408	1073.0115
MWOC -17	-2809.2614	76.2348	-2811.5741	76.1909
MWOC -18	-2885.4523	**0.0000**	-2887.8089	**0.0000**
MWOC -19	-836.0339	2050.3202	-837.4887	2049.4184
MWOC -20	-1285.2128	1600.8854	-1286.9235	1600.2395
MWOC -21	-2020.7744	865.0206	-2022.7883	864.6779
MWOC -22	-1076.3503	1809.7434	-1078.0655	1809.1020
MWOC -23	-1389.6786	1497.0240	-1390.7849	1495.7737
MWOC -24	-1209.5791	1676.9411	-1210.8678	1675.8732
MWOC -25	-914.5548	1971.7386	-916.0703	1970.8975
MWOC -26	-1351.2265	1534.6926	-1353.1163	1534.2258

Table 8.6: Zero-point corrected optimized energies (absolute and relative energies) of the representative $[\mathbf{M}^{V}\mathbf{=O}]^{(n+1)+}$ complexes in the solvent phase. All the energies were reported in Hartree.

MWOC	Solvent Phase			
	Absolute Energy (MN15-L)	Relative Energy (MN15-L)	Absolute Energy (M06-L)	Relative Energy (M06-L)
MWOC -1	-1611.1360	787.5755	-1612.6780	787.9064
MWOC -2	-1689.6365	709.0750	-1691.2504	709.3340
MWOC -3	-1636.1829	762.5286	-1637.8021	762.7823
MWOC -4	-1864.9998	533.7117	-1866.4239	534.1605
MWOC -5	-1943.4962	455.2153	-1944.9960	455.5884
MWOC -6	-2093.7664	304.9451	-2095.3881	305.1963
MWOC -7	-2273.6295	125.0820	-2275.3862	125.1982
MWOC -8	-2398.7115	**0.0000**	-2400.5844	**0.0000**
MWOC -9	-1691.9558	706.7557	-1693.5480	707.0364
MWOC -10	-1652.6246	746.0869	-1654.1796	746.4048
MWOC -11	-1771.5474	627.1641	-1773.2322	627.3522
MWOC -12	-1651.5111	747.2004	-1653.0542	747.5302
MWOC -13	-1807.3443	591.3672	-1809.0322	591.5522
MWOC -14	-764.5399	1634.1720	-765.6866	1634.8978
MWOC -15	-1481.8173	916.8942	-1482.8583	917.7261
MWOC -16	-967.1052	1431.6060	-968.5665	1432.0179
MWOC -17	-963.6013	1435.1100	-965.0297	1435.5547
MWOC -18	-1038.6128	1360.0990	-1040.0788	1360.5056
MWOC -19	-910.8722	1487.8390	-912.3713	1488.2131
MWOC -20	-1283.6881	1115.0234	-1285.7091	1114.8753
MWOC -21	-1635.2798	763.4317	-1637.3259	763.2585
MWOC -22	-1303.3252	1095.3860	-1303.2606	1097.3238
MWOC -23	-1464.7556	933.9559	-1465.9225	934.6619
MWOC -24	-1284.6492	1114.0620	-1285.9958	1114.5886
MWOC -25	-989.3854	1409.3260	-990.9810	1409.6034
MWOC -26	-1436.1351	962.5764	-1428.0918	972.4926

Table 8.7: Zero-point corrected optimized energies (absolute and relative energies) of the representative $[\mathbf{M}^{V}\mathbf{=O:\ H_2O}]^{(n+1)+}$ complexes in the solvent phase. All the energies were reported in Hartree.

MWOC	**Solvent Phase**			
	Absolute Energy (MN15-L)	**Relative Energy (MN15-L)**	**Absolute Energy (M06-L)**	**Relative Energy (M06-L)**
MWOC -1	-1840.0800	634.9125	-1841.8760	635.0495
MWOC -2	-1918.5805	556.4120	-1920.4516	556.4739
MWOC -3	-1865.1337	609.8588	-1866.9725	609.9530
MWOC -4	-1941.2527	533.7398	-1942.7465	534.1790
MWOC -5	-2019.7496	455.2429	-2021.3188	455.6067
MWOC -6	-2170.0200	304.9725	-2171.7111	305.2144
MWOC -7	-2349.8877	125.1048	-2351.7188	125.2067
MWOC -8	-2474.9925	**0.0000**	-2476.9255	**0.0000**
MWOC -9	-1768.2762	706.7163	-1769.9408	706.9847
MWOC -10	-1728.9936	745.9989	-1730.6336	746.2919
MWOC -11	-1847.8812	627.1113	-1849.6351	627.2904
MWOC -12	-1727.8342	747.1583	-1729.4497	747.4758
MWOC -13	-1883.6531	591.3394	-1885.4043	591.5212
MWOC -14	-840.8625	1634.1300	-842.0835	1634.8420
MWOC -15	-1482.0629	992.9296	-1483.8409	993.0846
MWOC -16	-1119.1013	1355.8912	-1120.7100	1356.2155
MWOC -17	-1115.6190	1359.3735	-1117.1922	1359.7333
MWOC -18	-1190.2741	1284.7184	-1192.2741	1284.6514
MWOC -19	-987.1958	1487.7967	-988.7672	1488.1583
MWOC -20	-1360.0510	1114.9415	-1361.8275	1115.0980
MWOC -21	-1711.6008	763.3917	-1713.7190	763.2065
MWOC -22	-1379.6289	1095.3636	-1381.6352	1095.2903
MWOC -23	-1541.0782	933.9143	-1542.3255	934.6000
MWOC -24	-1360.9598	1114.0327	-1362.4206	1114.5049
MWOC -25	-1065.7097	1409.2828	-1067.3629	1409.5626
MWOC -26	-1502.4188	972.5737	-1504.3941	972.5314

Table 8.8: Zero-point corrected optimized energies (absolute and relative energies) of the representative $[\mathbf{M^{IV}\text{-}OO}]^{n+}$ complexes in the solvent phase. All the energies were reported in Hartree.

MWOC	Solvent Phase			
	Absolute Energy (MN15-L)	**Relative Energy (MN15-L)**	**Absolute Energy (M06-L)**	**Relative Energy (M06-L)**
MWOC -1	-1686.3966	787.5872	-1687.9933	787.9423
MWOC -2	-1764.8947	709.0891	-1766.5712	709.3644
MWOC -3	-1711.4450	762.5388	-1713.1254	762.8102
MWOC -4	-1940.2439	533.7399	-1941.7290	534.2066
MWOC -5	-2018.7393	455.2445	-2020.2525	455.6831
MWOC -6	-2169.0073	304.9765	-2170.6406	305.2950
MWOC -7	-2348.8817	125.1021	-2350.6711	125.2645
MWOC -8	-2473.9838	**0.0000**	-2475.9356	**0.0000**
MWOC -9	-1768.8646	705.1192	-1768.8645	707.0711
MWOC -10	-1727.9481	746.0357	-1729.5906	746.3450
MWOC -11	-1846.8512	627.1326	-1848.5913	627.3443
MWOC -12	-1726.8064	747.1774	-1728.4104	747.5252
MWOC -13	-1882.6144	591.3694	-1884.3554	591.5802
MWOC -14	-839.8436	1634.1402	-841.0953	1634.8403
MWOC -15	-1481.0908	992.8930	-1482.8583	993.0773
MWOC -16	-1962.6326	511.3512	-1043.8016	1432.1340
MWOC -17	-1038.8186	1435.1652	-1040.3069	1435.6287
MWOC -18	-1113.7889	1360.1949	-1115.3612	1360.5744
MWOC -19	-986.2117	1487.7722	-987.7764	1488.1592
MWOC -20	-1359.0648	1114.9190	-1360.8370	1115.0986
MWOC -21	-1710.5943	763.3895	-1712.7036	763.2320
MWOC -22	-1378.5799	1095.4039	-1380.5910	1095.3446
MWOC -23	-1540.0105	933.9733	-1541.2430	934.6926
MWOC -24	-1359.8870	1114.0968	-1361.2942	1114.6414
MWOC -25	-1064.7363	1409.2475	-1066.3810	1409.5546
MWOC -26	-1501.4032	972.5806	-1504.0139	971.9217

Table 8.9: Copyright permission for Figure 1.3.

JOHN WILEY AND SONS LICENSE
TERMS AND CONDITIONS

Apr 01, 2025

This Agreement between Himangshu Pratim Bhattacharyya ("You") and John Wiley and Sons ("John Wiley and Sons") consists of your license details and the terms and conditions provided by John Wiley and Sons and Copyright Clearance Center.

License Number	6000100054741
License date	Apr 01, 2025
Licensed Content Publisher	John Wiley and Sons
Licensed Content Publication	Angewandte Chemie International Edition
Licensed Content Title	Structural Modifications of Mononuclear Ruthenium Complexes: A Combined Experimental and Theoretical Study on the Kinetics of Ruthenium-Catalyzed Water Oxidation
Licensed Content Author	Licheng Sun , Timofei Privalov, Yunhua Xu, et al
Licensed Content Date	Dec 9, 2010
Licensed Content Volume	50
Licensed Content Issue	2
Licensed Content Pages	5
Type of use	Dissertation/Thesis
Requestor type	University/Academic
Format	Print and electronic
Portion	Figure/table
Number of figures/tables	1
Will you be translating?	No
Title of new work	Theoretical Models for Predicting Catalytic Efficiencies
Institution name	Indian Institute of Technology Guwahati
Expected presentation date	Oct 2025
Portions	Scheme 1
The Requesting Person / Organization to Appear on the License	Himangshu Pratim Bhattacharyya

Table 8.10: Copyright permission for Figures (a) 1.4, (b) 1.5, (c) 1.6.

(a)

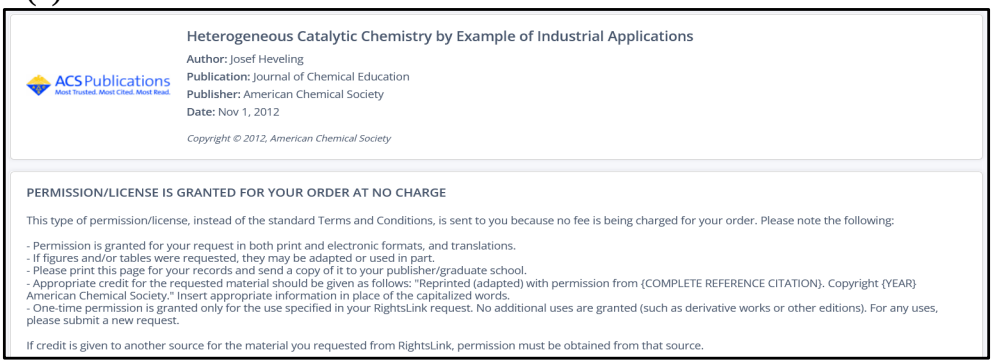

ACS Publications
Most Trusted. Most Cited. Most Read.

Heterogeneous Catalytic Chemistry by Example of Industrial Applications

Author: Josef Heveling
Publication: Journal of Chemical Education
Publisher: American Chemical Society
Date: Nov 1, 2012

Copyright © 2012, American Chemical Society

PERMISSION/LICENSE IS GRANTED FOR YOUR ORDER AT NO CHARGE

This type of permission/license, instead of the standard Terms and Conditions, is sent to you because no fee is being charged for your order. Please note the following:

- Permission is granted for your request in both print and electronic formats, and translations.
- If figures and/or tables were requested, they may be adapted or used in part.
- Please print this page for your records and send a copy of it to your publisher/graduate school.
- Appropriate credit for the requested material should be given as follows: "Reprinted (adapted) with permission from {COMPLETE REFERENCE CITATION}. Copyright {YEAR} American Chemical Society." Insert appropriate information in place of the capitalized words.
- One-time permission is granted only for the use specified in your RightsLink request. No additional uses are granted (such as derivative works or other editions). For any uses, please submit a new request.

If credit is given to another source for the material you requested from RightsLink, permission must be obtained from that source.

(b)

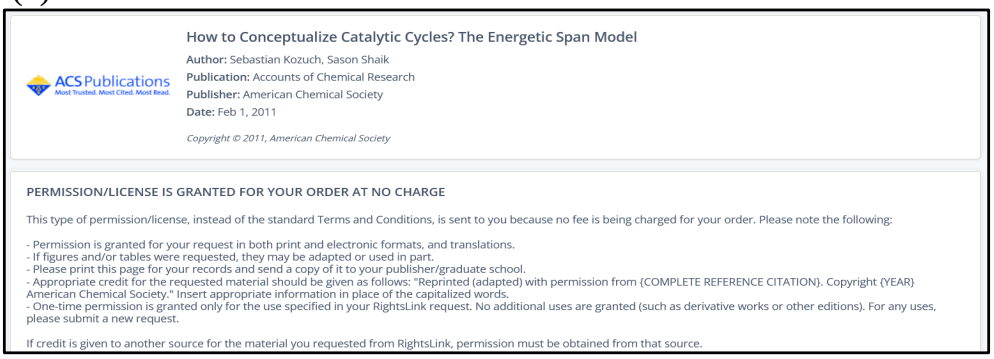

ACS Publications
Most Trusted. Most Cited. Most Read.

How to Conceptualize Catalytic Cycles? The Energetic Span Model

Author: Sebastian Kozuch, Sason Shaik
Publication: Accounts of Chemical Research
Publisher: American Chemical Society
Date: Feb 1, 2011

Copyright © 2011, American Chemical Society

PERMISSION/LICENSE IS GRANTED FOR YOUR ORDER AT NO CHARGE

This type of permission/license, instead of the standard Terms and Conditions, is sent to you because no fee is being charged for your order. Please note the following:

- Permission is granted for your request in both print and electronic formats, and translations.
- If figures and/or tables were requested, they may be adapted or used in part.
- Please print this page for your records and send a copy of it to your publisher/graduate school.
- Appropriate credit for the requested material should be given as follows: "Reprinted (adapted) with permission from {COMPLETE REFERENCE CITATION}. Copyright {YEAR} American Chemical Society." Insert appropriate information in place of the capitalized words.
- One-time permission is granted only for the use specified in your RightsLink request. No additional uses are granted (such as derivative works or other editions). For any uses, please submit a new request.

If credit is given to another source for the material you requested from RightsLink, permission must be obtained from that source.

(c)

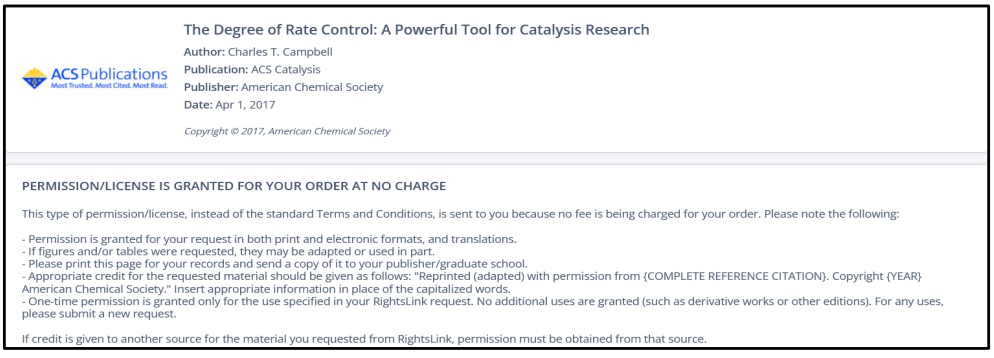

ACS Publications
Most Trusted. Most Cited. Most Read.

The Degree of Rate Control: A Powerful Tool for Catalysis Research

Author: Charles T. Campbell
Publication: ACS Catalysis
Publisher: American Chemical Society
Date: Apr 1, 2017

Copyright © 2017, American Chemical Society

PERMISSION/LICENSE IS GRANTED FOR YOUR ORDER AT NO CHARGE

This type of permission/license, instead of the standard Terms and Conditions, is sent to you because no fee is being charged for your order. Please note the following:

- Permission is granted for your request in both print and electronic formats, and translations.
- If figures and/or tables were requested, they may be adapted or used in part.
- Please print this page for your records and send a copy of it to your publisher/graduate school.
- Appropriate credit for the requested material should be given as follows: "Reprinted (adapted) with permission from {COMPLETE REFERENCE CITATION}. Copyright {YEAR} American Chemical Society." Insert appropriate information in place of the capitalized words.
- One-time permission is granted only for the use specified in your RightsLink request. No additional uses are granted (such as derivative works or other editions). For any uses, please submit a new request.

If credit is given to another source for the material you requested from RightsLink, permission must be obtained from that source.

Table 8.11: Copyright permission for Figure 1.7.

JOHN WILEY AND SONS LICENSE
TERMS AND CONDITIONS

Apr 01, 2025

This Agreement between Himangshu Pratim Bhattacharyya ("You") and John Wiley and Sons ("John Wiley and Sons") consists of your license details and the terms and conditions provided by John Wiley and Sons and Copyright Clearance Center.

License Number	6000100574308
License date	Apr 01, 2025
Licensed Content Publisher	John Wiley and Sons
Licensed Content Publication	WIRES Computational Molecular Science
Licensed Content Title	Microkinetic modeling in homogeneous catalysis
Licensed Content Author	Feliu Maseras, Maria Besora
Licensed Content Date	Jun 1, 2018
Licensed Content Volume	8
Licensed Content Issue	6
Licensed Content Pages	13
Type of use	Dissertation/Thesis
Requestor type	University/Academic
Format	Print and electronic
Portion	Figure/table
Number of figures/tables	1
Will you be translating?	No
Title of new work	Theoretical Models for Predicting Catalytic Efficiencies
Institution name	Indian Institute of Technology Guwahati
Expected presentation date	Oct 2025
Portions	Figure 1
The Requesting Person / Organization to Appear on the License	Himangshu Pratim Bhattacharyya

9

References

1. Berzelius, J. J. *Årsberättelse Om Framstegen i Fysik och Kemi: 1835* ; P. A. Norstedt and Söner, **1835**.

2. Kutney, G. *Sulfur: History, Technology, Applications and Industry*; Elsevier, **2023**.

3. van Santen, R. A.; van Leeuwen, P. W. N. M.; Moulijn, J. A.; Averill, B. A. *Catalysis: An Integrated Approach*; Elsevier, **2000**.

4. Ostwald, W.; Bredig, G. *Über Katalyse*; Leipzig: Akademische verlagsgesellschaft m. b. h., **1923**.

5. Chorkendorff, I.; Niemantsverdriet, J. W. *Concepts of Modern Catalysis and Kinetics*; John Wiley & Sons, **2017**.

6. Laidler, K. J. *Chemical Kinetics*; Pearson Education Inc., **1987**.

7. Tong, L.; Duan, L.; Xu, Y.; Privalov, T.; Sun, L. Structural modifications of mononuclear ruthenium complexes: A combined experimental and theoretical study on the kinetics of ruthenium-catalyzed water oxidation. *Angew. Chem. Int. Ed.* **2011**, *50*, 445–449.

8. Heveling, J. Heterogeneous catalytic chemistry by example of industrial applications. *J. Chem. Educ.* **2012**, *89*, 1530–1536.

9. Kakimoto, P. A.; Tamaki, F. K.; Cardoso, A. R.; Marana, S. R.; Kowaltowski, A. J. H_2O_2 release from the very long chain acyl-CoA dehydrogenase. *Redox Biology* **2015**, *4*, 375–380.

10. Alfonso-Prieto, M.; Biarnés, X.; Vidossich, P.; Rovira, C. The molecular mechanism of the catalase reaction. *J. Am. Chem. Soc.* **2009**, *131*, 11751–11761.

11. Kozuch, S.; Martin, J. M. "Turning over" definitions in catalytic cycles. *ACS Catal.* **2012**, *12*, 2787–2794.

12. Boudart, M.; Aldag, A.; Benson, J.; Dougharty, N.; Harkins, C. G. On the specific activity of platinum catalysts. *J. Catal.* **1966**, *6*, 92–99.

13. Turnover Frequency. IUPAC Compendium of Chemical Terminology, IUPAC Compendium of Chemical Terminology, *5th ed.* International Union of Pure

and Applied Chemistry; **2025**.

14. Yang, W.; Filonenko, G. A.; Pidko, E. A. Performance of homogeneous catalysts viewed in dynamics. *Chem. Commun.* **2023**, *59*, 1757–1768.

15. Behr, A.; Neubert, P. *Applied Homogeneous Catalysis*; John Wiley & Sons, **2012**.

16. van Eldik, R.; Hubbard, C. D. *Water Oxidation Catalysts*; Academic Press, **2019**.

17. Kozuch, S.; Shaik, S. How to conceptualize catalytic cycles? The energetic span model. *Acc. Chem. Res.* **2011**, *44*, 101–110.

18. Kozuch, S.; Martin, J. M. What makes for a bad catalytic cycle? A theoretical study on the Suzuki- Miyaura reaction within the energetic span model. *ACS Catal.* **2011**, *1*, 246–253.

19. Kozuch, S.; Shaik, S. A combined kinetic-quantum mechanical model for assessment of catalytic cycles: Application to cross-coupling and Heck reactions. *J. Am. Chem. Soc.* **2006**, *128*, 3355–3365.

20. Kozuch, S.; Shaik, S. Kinetic-quantum chemical model for catalytic cycles: The Haber- Bosch process and the effect of reagent concentration. *J. Phys. Chem. A* **2008**, *112*, 6032–6041.

21. Kozuch, S.; Lee, S. E.; Shaik, S. Theoretical analysis of the catalytic cycle of a nickel cross-coupling process: Application of the energetic span model. *Organometallics* **2009**, *28*, 1303–1308.

22. Kozuch, S. A refinement of everyday thinking: The energetic span model for kinetic assessment of catalytic cycles. *Wiley Interdiscip. Rev. Comput. Mol. Sci.* **2012**, *2*, 795–815.

23. Stegelmann, C.; Andreasen, A.; Campbell, C. T. Degree of rate control: How much the energies of intermediates and transition states control rates. *J. Am. Chem. Soc.* **2009**, *131*, 8077–8082.

24. Mao, Z.; Campbell, C. T. Kinetic isotope effects interpretation and prediction using degrees of rate control. *ACS Catal.* **2020**, *10*, 4181–4192.

25. Wodrich, M. D.; Sawatlon, B.; Busch, M.; Corminboeuf, C. The genesis of molecular volcano plots. *Acc. Chem. Res.* **2021**, *54*, 1107–1117.

26. Busch, M.; Wodrich, M. D.; Corminboeuf, C. Linear scaling relationships and volcano plots in homogeneous catalysis–revisiting the Suzuki reaction. *Chem. Sci.* **2015**, *6*, 6754–6761.

27. Wodrich, M. D.; Busch, M.; Corminboeuf, C. Accessing and predicting the kinetic profiles of homogeneous catalysts from volcano plots. *Chem. Sci.* **2016**,

7, 5723–5735.

28. Besora, M.; Maseras, F. Microkinetic modeling in homogeneous catalysis. *Wiley Interdiscip. Rev. Comput. Mol. Sci.* **2018**, *8*, e1372.

29. Christiansen, J. A. The elucidation of reaction mechanisms by the method of intermediates in quasi-stationary concentrations. *Adv. Catal.* **1953**, *5*, 311-353.

30. Campbell, C. T. Future directions and industrial perspectives micro-and macro-kinetics: Their relationship in heterogeneous catalysis. *Top. Catal.* **1994**, *1*, 353–366.

31. Campbell, C. T. Finding the rate-determining step in a mechanism: Comparing DeDonder relations with the "Degree of Rate Control". *J Catal.* **2001**, *204*, 525-529.

32. Campbell, C. T. The degree of rate control: A powerful tool for catalysis research. *ACS Catal.* **2017**, *7*, 2770-2779.

33. Eyring, H. The activated complex in chemical reactions. *J. Chem. Phys.* **1935**, *3*, 107–115.

34. Sabatier, P. *La catalyse en chimie organique; Librarie Polytechnique*, Paris, **1913**.

35. Sabatier, P. Hydrogénations et déshydrogénations par catalyse. *Ber. Dtsch. Chem. Ges.* **1911**, *44*, 1984–2001.

36. Gerischer, H. Mechanismus der elektrolytischen Wasserstoffabscheidung und Adsorptionsenergie von atomarem Wasserstoff. *Bull. Soc. Chim. Belg.* **1958**, *67*, 506–527.

37. Parsons, R. The rate of electrolytic hydrogen evolution and the heat of adsorption of hydrogen. *Trans. Faraday Soc.* **1958**, *54*, 1053–1063.

38. Kalikadien, A. V.; Pidko, E. A.; Sinha, V. ChemSpaX: exploration of chemical space by automated functionalization of molecular scaffold. *Digital Discovery* **2022**, *1*, 8–25.

39. Hashemi, A.; Bougueroua, S.; Gaigeot, M.-P.; Pidko, E. A. ReNeGate: A reaction network graph-theoretical tool for automated mechanistic studies in computational homogeneous catalysis. *J. Chem. Theor. Comput.* **2022**, *18*, 7470–7482.

40. van Putten, R.; Uslamin, E. A.; Garbe, M.; Liu, C.; Gonzalez-de Castro, A.; Lutz, M.; Junge, K.; Hensen, E. J.; Beller, M.; Lefort, L. et al. Non-pincer-type manganese complexes as efficient catalysts for the hydrogenation of esters. *Angew. Chem. Int. Ed.* **2017**, *56*, 7531–7534.

41. Filonenko, G. A.; van Putten, R.; Hensen, E. J.; Pidko, E. A. Catalytic (de) hydrogenation promoted by non-precious metals–Co, Fe and Mn: recent advances in an emerging field. *Chem. Soc. Rev.* **2018**, *47*, 1459–1483.

42. González, T.; García, J. J. Catalytic CO_2 hydrosilylation with $[Mn(CO)_5Br]$ under mild reaction conditions. *Polyhedron* **2021**, *203*, 115242 (1-8).

43. van Putten, R.; Filonenko, G. A.; Gonzalez de Castro, A.; Liu, C.; Weber, M.; Müller, C.; Lefort, L.; Pidko, E. Mechanistic complexity of asymmetric transfer hydrogenation with simple Mn–diamine catalysts. *Organometallics* **2019**, *38*, 3187–3196.

44. Krieger, A. M.; Pidko, E. A. The impact of computational uncertainties on the enantioselectivity predictions: A microkinetic modeling of ketone transfer hydrogenation with a Noyori-type Mn-diamine catalyst. *ChemCatChem* **2021**, *13*, 3517–3524.

45. Hashemi, A.; Bougueroua, S.; Gaigeot, M.-P.; Pidko, E. A. HiREX: High throughput reactivity exploration for extended databases of transition-metal catalysts. *J. Chem. Inf. Model.* **2023**, *63*, 6081–6094.

46. Krieger, A. M.; Sinha, V.; Kalikadien, A. V.; Pidko, E. A. Metal-ligand cooperative activation of HX (X= H, Br, OR) bond on Mn based pincer complexes. *Z. Anorg. Allg. Chem* **2021**, *647*, 1486–1494.

47. Pidko, E. A. Death and life of catalysts: a theory-guided unified approach for non-critical metal catalyst development. *https://cordis.europa.eu/project/id/725686*, DOI: 10.3030 /725686, **2017**.

48. van Putten, R.; Benschop, J.; de Munck, V. J.; Weber, M.; Müller, C.; Filonenko, G. A.; Pidko, E. A. Efficient and practical transfer hydrogenation of ketones catalyzed by a simple bidentate Mn- NHC complex. *ChemCatChem* **2019**, *11*, 5232–5235.

49. Yang, W.; Chernyshov, I. Y.; van Schendel, R. K.; Weber, M.; Müller, C.; Filonenko, G. A.; Pidko, E. A. Robust and efficient hydrogenation of carbonyl compounds catalysed by mixed donor Mn (I) pincer complexes. *Nat. Commun.* **2021**, *12*, 1-8.

50. Bhattacharyya, H. P.; Sarma, M. Efficiency conceptualization model: A theoretical method for predicting the turnover of catalysts. *ChemPhysChem* **2024**, *25*, e202400004 (1-12).

51. McQuarrie, D. A.; Simon, J. D. *Physical Chemistry: A Molecular Approach*; University Science Books Sausalito, CA, **1997**.

52. Eckart, C. The penetration of a potential barrier by electrons. *Phys. Rev.* **1930**, *35*, 1303–1309.

53. Johnston, H. S.; Heicklen, J. Tunnelling corrections for unsymmetrical Eckart potential energy barriers. *J. Phys. Chem.* **1962**, *66*, 532–533.

54. Wigner, E. P. *Part I: Physical Chemistry.*; Springer, **1997**.

55. Bhattacharyya, H. P.; Sarma, M. *MaxKinEff*: A collision theory-based approach for analyzing turnover frequency and turnover number in catalytic processes. *Chem. Asian J.* **2024**, *19*, e202400674 (1-11).

56. Sherer, E. C.; Cramer, C. J. Quantum chemical characterization of methane metathesis in L_2MCH_3 (L= H, Cl, Cp, Cp*; M= Sc, Y, Lu). *Organometallics* **2003**, *22*, 1682–1689.

57. Bao, J. L.; Truhlar, D. G. Variational transition state theory: Theoretical framework and recent developments. *Chem. Soc. Rev.* **2017**, *46*, 7548–7596.

58. Bell–Evans–Polanyi principle, IUPAC Compendium of Chemical Terminology, *5th ed.* International Union of Pure and Applied Chemistry; **2025**.

59. Anantharaj, S.; Karthik, P. E.; Noda, S. The significance of properly re- porting turnover frequency in electrocatalysis research. *Angew. Chem. Int. Ed.* **2021**, *60*, 23051–23067.

60. Hetterscheid, D. G.; Reek, J. N. Mononuclear water oxidation catalysts. *Angew. Chem. Int. Ed.* **2012**, *51*, 9740–9747.

61. Meyer, T. J. Chemical approaches to artifcial photosynthesis. *Acc. Chem. Res.* **1989**, *22*, 163–170.

62. Berto, T. F.; Sanwald, K. E.; Byers, J. P.; Browning, N. D.; Gutiérrez, O. Y.; Lercher, J. A. Enabling overall water splitting on photocatalysts by CO-covered noble metal co-catalysts. *J. Phys. Chem. Lett.* **2016**, *7*, 4358–4362.

63. Neudeck, S.; Maji, S.; López, I.; Meyer, S.; Meyer, F.; Llobet, A. New powerful and oxidatively rugged dinuclear Ru water oxidation catalyst: Control of mechanistic pathways by tailored ligand design. *J. Am. Chem. Soc.* **2014**, *136*, 24–27.

64. Shao, Y.; de Groot, H. J.; Buda, F. Proton acceptor near the active site lowers dramatically the O–O bond formation energy barrier in photocatalytic water splitting. *J. Phys. Chem. Lett.* **2019**, *10*, 7690–7697.

65. Krewald, V.; Retegan, M.; Neese, F.; Lubitz, W.; Pantazis, D. A.; Cox, N. Spin state as a marker for the structural evolution of nature's water-splitting catalyst. *Inorg. Chem.* **2016**, *55*, 488–501.

66. Pérez-Navarro, M.; Neese, F.; Lubitz, W.; Pantazis, D. A.; Cox, N. Recent developments in biological water oxidation. *Curr. Opin. Chem. Bio.* **2016**, *31*, 113–119.

67. Fan, T.; Duan, L.; Huang, P.; Chen, H.; Daniel, Q.; Ahlquist, M. S.; Sun, L. The Ru-tpc water oxidation catalyst and beyond: Water nucleophilic attack pathway versus radical coupling pathway. *ACS Catal.* **2017**, *7*, 2956–2966.

68. Hoque, M. A.; Chowdhury, A. D.; Maji, S.; Benet-Buchholz, J.; Ertem, M. Z.; Gimbert-Suriñach, C.; Lahiri, G. K.; Llobet, A. Synthesis, characterization, and water oxidation activity of isomeric Ru complexes. *Inorg. Chem.* **2021**, *60*, 5791–5803.

69. Schilling, M.; Cunha, R. A.; Luber, S. Enhanced ab initio molecular dynamics exploration unveils the complex role of different intramolecular bases on the water nucleophilic attack mechanism. *ACS Catal.* **2020**, *10*, 7657–7667.

70. Gil-Sepulcre, M.; Böhler, M.; Schilling, M.; Bozoglian, F.; Bachmann, C.; Scherer, D.; Fox, T.; Spingler, B.; Gimbert-Suriñach, C.; Alberto, R. et al. Ruthenium water oxidation catalysts based on pentapyridyl ligands. *ChemSusChem* **2017**, *10*, 4517–4525.

71. Busch, M.; Fabrizio, A.; Luber, S.; Hutter, J.; Corminboeuf, C. Exploring the limitation of molecular water oxidation catalysts. *J. Phys. Chem. C* **2018**, *122*, 12404–12412.

72. Lee, W.-T.; Muñoz III, S. B.; Dickie, D. A.; Smith, J. M. Ligand modifcation transforms a catalase mimic into a water oxidation catalyst. *Angew. Chem.*

Int. Ed. **2014**, *53*, 9856–9859.

73. Crandell, D. W.; Xu, S.; Smith, J. M.; Baik, M.-H. Intramolecular oxyl radical coupling promotes O–O bond formation in a homogeneous mononuclear Mn-based water oxidation catalyst: A computational mechanistic investigation. *Inorg. Chem.* **2017**, *56*, 4435–4445.

74. Naruta, Y.; Sasayama, M.; Sasaki, T. Oxygen evolution by oxidation of water with manganese porphyrin dimers. *Angew. Chem. Int. Ed.* **1994**, *33*, 1839–1841.

75. Okamura, M.; Kondo, M.; Kuga, R.; Kurashige, Y.; Yanai, T.; Hayami, S.; Praneeth, V. K.; Yoshida, M.; Yoneda, K.; Kawata, S. et al. A pentanuclear iron catalyst designed for water oxidation. *Nature* **2016**, *530*, 465–468.

76. Kleingardner, J. G.; Kandemir, B.; Bren, K. L. Hydrogen evolution from neutral water under aerobic conditions catalyzed by cobalt microperoxidase-11. *J. Am. Chem. Soc.* **2014**, *136*, 4–7.

77. Kandemir, B.; Kubie, L.; Guo, Y.; Sheldon, B.; Bren, K. L. Hydrogen evolution from water under aerobic conditions catalyzed by a cobalt ATCUN metallopeptide. *Inorg. Chem.* **2016**, *55*, 1355–1357.

78. Lai, W.; Cao, R.; Dong, G.; Shaik, S.; Yao, J.; Chen, H. Why is cobalt the best

transition metal in transition-metal hangman corroles for O–O bond formation during water oxidation? *J. Phys. Chem. Lett.* **2012**, *3*, 2315–2319.

79. Wang, L.-P.; Van Voorhis, T. Direct-coupling O_2 bond forming a pathway in cobalt oxide water oxidation catalysts. *J. Phys. Chem. Lett.* **2011**, *2*, 2200–2204.

80. Zhang, M.-T.; Chen, Z.; Kang, P.; Meyer, T. J. Electrocatalytic water oxidation with a copper (II) polypeptide complex. *J. Am. Chem. Soc.* **2013**, *135*, 2048–2051.

81. Wang, D.; Ghirlanda, G.; Allen, J. P. Water oxidation by a nickel-glycine catalyst. *J. Am. Chem. Soc.* **2014**, *136*, 10198–10201.

82. Li, M.; Takada, K.; Goldsmith, J. I.; Bernhard, S. Iridium (III) bis-pyridine-2-sulfonamide complexes as efficient and durable catalysts for homogeneous water oxidation. *Inorg. Chem.* **2016**, *55*, 518–526.

83. Richmond, C. J.; Escayola, S.; Poater, A. Axial ligand effects of Ru-BDA complexes in the O–O bond formation via the I2M bimolecular mechanism in water oxidation catalysis. *Eur. J. Inorg. Chem.* **2019**, *2019*, 2101–2108.

84. Wang, L.; Duan, L.; Wang, Y.; Ahlquist, M. S.; Sun, L. Highly efficient and robust molecular water oxidation catalysts based on ruthenium complexes. *Chem.*

Commun. **2014**, *50*, 12947–12950.

85. Duan, L.; Wang, L.; Li, F.; Li, F.; Sun, L. Highly efficient bioinspired molecular Ru water oxidation catalysts with negatively charged backbone ligands. *Acc. Chem. Res.* **2015**, *48*, 2084–2096.

86. Liu, Y.; Su, X.; Guan, W.; Yan, L. Ruthenium-based catalysts for water oxidation: The key role of carboxyl groups as proton acceptors. *Phys. Chem. Chem. Phys.* **2020**, *22*, 5249–5254.

87. Luque-Urrutia, J. A.; Kamdar, J. M.; Grotjahn, D. B.; Solà, M.; Poater, A. Understanding the performance of a bisphosphonate Ru water oxidation catalyst. *Dalton Trans.* **2020**, *49*, 14052–14060.

88. Blakemore, J. D.; Crabtree, R. H.; Brudvig, G. W. Molecular catalysts for water oxidation. *Chem. Rev.* **2015**, *115*, 12974–13005.

89. Gersten, S. W.; Samuels, G. J.; Meyer, T. J. Catalytic oxidation of water by an oxo-bridged ruthenium dimer. *J. Am. Chem. Soc.* **1982**, *104*, 4029-4030.

90. Gilbert, J. A.; Eggleston, D. S.; Murphy Jr., W. R.; Geselowitz, D. A.; Gersten, S. W.; Hodgson, D. J.; Meyer, T. J. Structure and redox properties of the water-oxidation catalyst $[(bpy)_2(OH_2)RuORu(OH_2)(bpy)_2]^{4+}$. *J. Am. Chem. Soc.* **1985**, *107*, 3855–3864.

91. Chronister, C. W.; Binstead, R. A.; Ni, J.; Meyer, T. J. Mechanism of water oxidation catalyzed by the μ-oxo dimer $[(bpy)_2(OH_2)RuORu(OH_2)(bpy)_2]^{4+}$. *Inorg. Chem.* **1997**, *36*, 3814–3815.

92. Sens, C.; Romero, I.; Rodríguez, M.; Llobet, A.; Parella, T.; BenetBuchholz, J. A new Ru complex capable of catalytically oxidizing water to molecular dioxygen. *J. Am. Chem. Soc.* **2004**, *126*, 7798–7799.

93. Deng, Z.; Tseng, H.-W.; Zong, R.; Wang, D.; Thummel, R. Preparation and study of a family of dinuclear Ru (II) complexes that catalyze the decomposition of water. *Inorg. Chem.* **2008**, *47*, 1835–1848.

94. Zong, R.; Thummel, R. P. A new family of Ru complexes for water oxidation. *J. Am. Chem. Soc.* **2005**, *127*, 12802–12803.

95. Polyansky, D. E.; Muckerman, J. T.; Rochford, J.; Zong, R.; Thummel, R. P.; Fujita, E. Water oxidation by a mononuclear ruthenium catalyst: Characterization of the intermediates. *J. Am. Chem. Soc.* **2011**, *133*, 14649–14665.

96. Concepcion, J. J.; Jurss, J. W.; Templeton, J. L.; Meyer, T. J. One site is enough. Catalytic water oxidation by $[Ru(tpy)(bpm)(OH_2)]^{2+}$ and $[Ru(tpy)(bpz)(OH_2)]^{2+}$. *J. Am. Chem. Soc.* **2008**, *130*, 16462–16463.

97. Wasylenko, D. J.; Palmer, R. D.; Berlinguette, C. P. Homogeneous water ox-

idation catalysts containing a single metal site. *Chem. Commun.* **2013**, *49*, 218–227.

98. Tong, L.; Thummel, R. P. Mononuclear ruthenium polypyridine complexes that catalyze water oxidation. *Chem. Sci.* **2016**, *7*, 6591–6603.

99. Duan, L.; Xu, Y.; Zhang, P.; Wang, M.; Sun, L. Visible light-driven water oxidation by a molecular ruthenium catalyst in homogeneous system. *Inorg. Chem.* **2010**, *49*, 209–215.

100. Zhang, B.; Sun, L. Ru-bda: Unique molecular water-oxidation catalysts with distortion induced open site and negatively charged ligands. *J. Am. Chem. Soc.* **2019**, *141*, 5565–5580.

101. Sala, X.; Maji, S.; Bofill, R.; García-Antón, J.; Escriche, L.; Llobet, A. Molecular water oxidation mechanisms followed by transition metals: State of the art. *Acc. Chem. Res.* **2014**, *47*, 504–516.

102. Shaffer, D. W.; Xie, Y.; Concepcion, J. J. O-O bond formation in ruthenium-catalyzed water oxidation: Single-site nucleophilic attack vs. O–O radical coupling. *Chem. Soc. Rev.* **2017**, *46*, 6170–6193.

103. Yang, J.; Wang, L.; Zhan, S.; Zou, H.; Chen, H.; Ahlquist, M. S.; Duan, L.; Sun, L. From Ru-bda to Ru-bds: A step forward to highly efficient molecular water

oxidation electrocatalysts under acidic and neutral conditions. *Nat. Commun.* **2021**, *12*, 1–10.

104. Duan, L.; Araujo, C. M.; Ahlquist, M. S.; Sun, L. Highly efficient and robust molecular ruthenium catalysts for water oxidation. *Proc. Natl. Acad. Sci. USA* **2012**, *109*, 15584–15588.

105. Nyhlén, J.; Duan, L.; Åkermark, B.; Sun, L.; Privalov, T. Evolution of O_2 in a seven-coordinate Ru^{IV} dimer complex with a $[HOHOH]^-$ bridge: A computational study. *Angew. Chem. Int. Ed.* **2010**, *49*, 1773–1777.

106. Wang, L.; Duan, L.; Stewart, B.; Pu, M.; Liu, J.; Privalov, T.; Sun, L. Toward controlling water oxidation catalysis: Tunable activity of ruthenium complexes with axial imidazole/DMSO ligands. *J. Am. Chem. Soc.* **2012**, *134*, 18868–18880.

107. Fan, T.; Zhan, S.; Ahlquist, M. S. Why is there a barrier in the coupling of two radicals in the water oxidation reaction? *ACS Catal.* **2016**, *6*, 8308–8312.

108. Staehle, R.; Tong, L.; Wang, L.; Duan, L.; Fischer, A.; Ahlquist, M. S.; Sun, L.; Rau, S. Water oxidation catalyzed by mononuclear ruthenium complexes with a 2,2´-bipyridine-6,6´-dicarboxylate (bda) ligand: How ligand environment influences the catalytic behavior. *Inorg. Chem.* **2014**, *53*, 1307–1319.

109. Zhan, S.; Mårtensson, D.; Purg, M.; Kamerlin, S. C.; Ahlquist, M. S. Capturing the role of explicit solvent in the dimerization of Ru^{V}(bda) water oxidation catalysts. *Angew. Chem. Int. Ed.* **2017**, *56*, 6962–6965.

110. Zhang, B.; Zhan, S.; Liu, T.; Wang, L.; Inge, A. K.; Duan, L.; Timmer, B. J.; Kravchenko, O.; Li, F.; Ahlquist, M. S. et al. Switching O-O bond formation mechanism between WNA and I2M pathways by modifying the Ru-bda backbone ligands of water-oxidation catalysts. *J. Energy Chem.* **2021**, *54*, 815–821.

111. Huynh, M. H. V.; Meyer, T. J. Proton-coupled electron transfer. *Chem. Rev.* **2007**, *107*, 5004–5064.

112. Betley, T. A.; Wu, Q.; Van Voorhis, T.; Nocera, D. G. Electronic design criteria for O- O bond formation via metal- oxo complexes. *Inorg. Chem.* **2008**, *47*, 1849–1861.

113. Karkas, M. D.; Verho, O.; Johnston, E. V.; Åkermark, B. Artificial photosynthesis: Molecular systems for catalytic water oxidation. *Chem. Rev.* **2014**, *114*, 11863–12001.

114. Ashley, D. C.; Baik, M.-H. The electronic structure of [Mn (V)=O]: What is the connection between oxyl radical character, physical oxidation state, and reactivity? *ACS Catal.* **2016**, *6*, 7202–7216.

115. Fillol, J. L.; Codolà, Z.; Garcia-Bosch, I.; Gómez, L.; Pla, J. J.; Costas, M. Efficient water oxidation catalysts based on readily available iron coordination complexes. *Nat. Chem.* **2011**, *3*, 807–813.

116. Acuña-Parés, F.; Costas, M.; Luis, J. M.; Fillol, J. L. Theoretical study of the water oxidation mechanism with non-heme Fe(Pytacn) iron complexes. Evidence that the Fe^{IV}(O)(Pytacn) species cannot react with the water molecule to form the O–O bond. *Inorg. Chem.* **2014**, *53*, 5474–5485.

117. Liu, T.; Zhang, B.; Sun, L. Iron-based molecular water oxidation catalysts: Abundant, cheap, and promising. *Chem. Asian J.* **2019**, *14*, 31–43.

118. Ellis, W. C.; McDaniel, N. D.; Bernhard, S.; Collins, T. J. Fast water oxidation using iron. *J. Am. Chem. Soc.* **2010**, *132*, 10990–10991.

119. Leung, C.-F.; Ng, S.-M.; Ko, C.-C.; Man, W.-L.; Wu, J.; Chen, L.; Lau, T.- C. A cobalt (II) quaterpyridine complex as a visible light-driven catalyst for both water oxidation and reduction. *Energy Environ. Sci.* **2012**, *5*, 7903–7907.

120. Hong, D.; Jung, J.; Park, J.; Yamada, Y.; Suenobu, T.; Lee, Y.-M.; Nam, W.; Fukuzumi, S. Water-soluble mononuclear cobalt complexes with organic ligands acting as precatalysts for efficient photocatalytic water oxidation. *Energy Environ. Sci.* **2012**, *5*, 7606–7616.

121. Zhang, M.; Zhang, M.-T.; Hou, C.; Ke, Z.-F.; Lu, T.-B. Homogeneous electrocatalytic water oxidation at neutral pH by a robust macrocyclic nickel (II) complex. *Angew. Chem. Int. Ed.* **2014**, *126*, 13258–13264.

122. Rudshteyn, B.; Fisher, K. J.; Lant, H. M.; Yang, K. R.; Mercado, B. Q.; Brudvig, G. W.; Crabtree, R. H.; Batista, V. S. Water-nucleophilic attack mechanism for the Cu^{II} $(pyalk)_2$ water-oxidation catalyst. *ACS Catal.* **2018**, *8*, 7952–7960.

123. Young, K. J.; Takase, M. K.; Brudvig, G. W. An anionic N-donor ligand promotes manganese-catalyzed water oxidation. *Inorg. Chem.* **2013**, *52*, 7615–7622.

124. Barnett, S. M.; Goldberg, K. I.; Mayer, J. M. A soluble copper–bipyridine water-oxidation electrocatalyst. *Nat. Chem.* **2012**, *4*, 498–502.

125. Fisher, K. J.; Materna, K. L.; Mercado, B. Q.; Crabtree, R. H.; Brudvig, G. W. Electrocatalytic water oxidation by a copper (II) complex of an oxidation-resistant ligand. *ACS Catal.* **2017**, *7*, 3384–3387.

126. Stott, L. A.; Prosser, K. E.; Berdichevsky, E. K.; Walsby, C. J.; Warren, J. J. Lowering water oxidation overpotentials using the ionisable imidazole of copper (2-(2-pyridyl) imidazole). *Chem. Commun.* **2017**, *53*, 651–654.

127. Su, X.-J.; Gao, M.; Jiao, L.; Liao, R.-Z.; Siegbahn, P. E.; Cheng, J.-P.; Zhang,

M.-T. Electrocatalytic water oxidation by a dinuclear copper complex in a neutral aqueous solution. *Angew. Chem. Int. Ed.* **2015**, *54*, 4909–4914.

128. Duan, L.; Bozoglian, F.; Mandal, S.; Stewart, B.; Privalov, T.; Llobet, A.; Sun, L. A molecular ruthenium catalyst with water-oxidation activity comparable to that of photosystem II. *Nat. Chem.* **2012**, *4*, 418–423.

129. Tseng, H.-W.; Zong, R.; Muckerman, J. T.; Thummel, R. Mononuclear ruthenium (II) complexes that catalyze water oxidation. *Inorg. Chem.* **2008**, *47*, 11763–11773.

130. Signorella, S.; Hureau, C. Bioinspired functional mimics of the manganese catalases. *Coord. Chem. Rev.* **2012**, *256*, 1229–1245.

131. Li, Y.-Y.; Ye, K.; Siegbahn, P. E.; Liao, R.-Z. Mechanism of water oxidation catalyzed by a mononuclear manganese complex. *ChemSusChem* **2017**, *10*, 903–911.

132. Company, A.; Gómez, L.; Güell, M.; Ribas, X.; Luis, J. M.; Que, L.; Costas, M. Alkane hydroxylation by a nonheme iron catalyst that challenges the heme paradigm for oxygenase action. *J. Am. Chem. Soc.* **2007**, *129*, 15766–15767.

133. Yin, Q.; Tan, J. M.; Besson, C.; Geletii, Y. V.; Musaev, D. G.; Kuznetsov, A. E.; Luo, Z.; Hardcastle, K. I.; Hill, C. L. A fast soluble carbon-free molecular water

oxidation catalyst based on abundant metals. *Science* **2010**, *328*, 342–345.

134. Xiao, D.; Gregg, J.; Lakshmi, K.; Bonitatibus Jr, P. J. Bio-inspired molecular catalysts for water oxidation. *Catalysts* **2021**, *11*, 1068 (1-51).

135. Wang, L.; Duan, L.; Ambre, R. B.; Daniel, Q.; Chen, H.; Sun, J.; Das, B.; Thapper, A.; Uhlig, J.;Dinér, P. et al. A nickel (II) PY5 complex as an electrocatalyst for water oxidation. *J. Catal.* **2016**, *335*, 72–78.

136. Coggins, M. K.; Zhang, M.-T.; Chen, Z.; Song, N.; Meyer, T. J. Single-site copper (II) water oxidation electrocatalysis: Rate enhancements with HPO_4^{2-} as a proton acceptor at pH 8. *Angew. Chem. Int. Ed.* **2014**, *53*, 12226–12230.

137. McDaniel, N. D.; Coughlin, F. J.; Tinker, L. L.; Bernhard, S. Cyclometalated iridium (III) aquo complexes: Efficient and tunable catalysts for the homogeneous oxidation of water. *J. Am. Chem. Soc.* **2008**, *130*, 210–217.

138. Hull, J. F.; Balcells, D.; Blakemore, J. D.; Incarvito, C. D.; Eisenstein, O.; Brudvig, G. W.; Crabtree, R. H. Highly active and robust Cp^* iridium complexes for catalytic water oxidation. *J. Am. Chem. Soc.* **2009**, *131*, 8730–8731.

139. Bucci, A.; Savini, A.; Rocchigiani, L.; Zuccaccia, C.; Rizzato, S.; Albinati, A.; Llobet, A.; Macchioni, A. Organometallic iridium catalysts based on pyridinecarboxylate ligands for the oxidative splitting of water. *Organometallics* **2012**, *31*,

8071–8074.

140. Zhao, Y.; Truhlar, D. G. A new local density functional for main-group thermochemistry, transition metal bonding, thermochemical kinetics, and noncovalent interactions. *J. Chem. Phys.* **2006**, *125*, 194101 (1-18).

141. Yu, H. S.; He, X.; Truhlar, D. G. MN15-L: A new local exchange-correlation functional for Kohn–Sham density functional theory with broad accuracy for atoms, molecules, and solids. *J. Chem. Theor. Comput.* **2016**, *12*, 1280–1293.

142. Ditchfeld, R.; Hehre, W. J.; Pople, J. A. Self-consistent molecular-orbital methods. IX. An extended Gaussian-type basis for molecular-orbital studies of organic molecules. *J. Chem. Phys.* **1971**, *54*, 724–728.

143. Harper, D. R.; Kulik, H. J. Computational scaling relationships predict experimental activity and rate-limiting behavior in homogeneous water oxidation. *Inorg. Chem.* **2022**, *61*, 2186–2197.

144. Kumar, R.; Pandey, B.; Singh, A.; Rajaraman, G. Mechanistic insights into the oxygen atom transfer reactions by nonheme manganese complex: A computational case study on the comparative oxidative ability of manganese-hydroperoxo vs Mn^{IV}=O and Mn^{IV}–OH intermediates. *Inorg. Chem.* **2021**, *60*, 12085–12099.

145. Frisch, M. J.; Trucks, G. W.; Schlegel, H. B.; Scuseria, G. E.; Robb, M. A.;

Cheeseman, J. R.; Scalmani, G.; Barone, V.; Petersson, G. A.; Nakatsuji, H. et al. Gaussian16 Revision C.01. 2016; Gaussian Inc. Wallingford CT.

146. Marenich, A. V.; Cramer, C. J.; Truhlar, D. G. Universal solvation model based on solute electron density and on a continuum model of the solvent defined by the bulk dielectric constant and atomic surface tensions. *J. Phys. Chem. B* **2009**, *113*, 6378–6396.

147. Edler, E.; Stein, M. Spin-state-dependent properties of an iron (III) hydrogenase mimic. *Eur. J. Inorg. Chem.* **2014**, *2014*, 3587–3599.

148. Moltved, K. A.; Kepp, K. P. Performance of density functional theory for transition metal oxygen bonds. *ChemPhysChem.* **2019**, *20*, 3210–3220.

149. Hay, P. J.; Wadt, W. R. Ab initio effective core potentials for molecular calculations. Potentials for the transition metal atoms Sc to Hg. *J. Chem. Phys.* **1985**, *82*, 270–283.

150. Roy, L. E.; Hay, P. J.; Martin, R. L. Revised basis sets for the LANL effective core potentials. *J. Chem. Theor. Comput.* **2008**, *4*, 1029–1031.

151. Weigend, F.; Ahlrichs, R. Balanced basis sets of split valence, triple zeta valence and quadruple zeta valence quality for H to Rn: Design and assessment of accuracy. *Phys. Chem. Chem. Phys.* **2005**, *7*, 3297–3305.

152. Zhang, G.; Chen, K.; Chen, H.; Yao, J.; Shaik, S. What factors control O_2 binding and release thermodynamics in mononuclear ruthenium water oxidation catalysts? A theoretical exploration. *Inorg. Chem.* **2013**, *52*, 5088–5096.

153. Yamaguchi, K.; Jensen, F.; Dorigo, A.; Houk, K. A spin correction procedure for unrestricted Hartree-Fock and Møller-Plesset wavefunctions for singlet diradicals and polyradicals. *Chem. Phys. Lett.* **1988**, *149*, 537–542.

154. Privalov, T.; Åkermark, B.; Sun, L. The O−O bonding in water oxidation: The electronic structure portrayal of a concerted oxygen atom–proton transfer pathway. *Chem. Eur. J* **2011**, *17*, 8313–8317.

155. Pearson, R. G. Absolute electronegativity and hardness correlated with molecular orbital theory. *Proc. Natl. Acad. Sci. USA* **1986**, 83, 8440–8441.

156. Vallés-Pardo, J. L.; Guijt, M. C.; Iannuzzi, M.; Joya, K. S.; de Groot, H. J.; Buda, F. Ab initio molecular dynamics study of water oxidation reaction pathways in mono-Ru catalysts. *ChemPhysChem* **2012**, *13*, 140–146.

157. Hutter, J.; Iannuzzi, M.; Schiffmann, F.; VandeVondele, J. *Wiley Interdiscip. Rev. Comput. Mol. Sci.* **2014**, *4*, 15–25.

158. Kühne, T. D.; Iannuzzi, M.; Del Ben, M.; Rybkin, V. V.; Seewald, P.; Stein, F.; Laino, T.; Khaliullin, R. Z.; Schütt, O.; Schiffmann, F. et al. CP2K: An

electronic structure and molecular dynamics software package - Quickstep: Efficient and accurate electronic structure calculations. *J. Chem. Phys.* **2020**, *152*, 194103 (1-47).

159. Goedecker, S.; Teter, M.; Hutter, J. Separable dual-space Gaussian pseudopotentials. *Phys. Rev. B* **1996**, *54*, 1703-1710.

160. VandeVondele, J.; Hutter, J. Gaussian basis sets for accurate calculations on molecular systems in gas and condensed phases. *J. Chem. Phys.* **2007**, *127*, 114105 (1-9).

161. Grimme, S.; Antony, J.; Ehrlich, S.; Krieg, H. A consistent and accurate *ab initio* parametrization of density functional dispersion correction (DFT-D) for the 94 elements H-Pu. *J. Chem. Phys.* **2010**, *132*, 154104 (1-19).

162. Evans, D. J.; Holian, B. L. The Nose–Hoover thermostat. *J. Chem. Phys.* **1985**, *83*, 4069–4074.

163. Tan, P.; Kwong, H.-K.; Lau, T.-C. Catalytic oxidation of water and alcohols by a robust iron (III) complex bearing a cross-bridged cyclam ligand. *Chem. Commun.* **2015**, *51*, 12189–12192.

164. Schober, P.; Boer, C.; Schwarte, L. A. Correlation coefficients: Appropriate use and interpretation. *Anesth. Analg.* **2018**, *126*, 1763–1768.

165. Liu, C.; van Putten, R.; Kulyaev, P. O.; Filonenko, G. A.; Pidko, E. A. Computational insights into the catalytic role of the base promoters in ester hydrogenation with homogeneous non-pincer-based Mn-P, N catalyst. *J. Catal.* **2018**, *363*, 136–143.

166. Chu, S.; Coccia, E.; Barborini, M.; Guidoni, L. Role of electron correlation along the water splitting reaction. *J. Chem. Theor. Comput.* **2016**, *12*, 5803–5810.

167. Romain, S.; Vigara, L.; Llobet, A. Oxygen-oxygen bond formation pathways promoted by ruthenium complexes. *Acc. Chem. Res.* **2009**, *42*, 1944–1953.